



CONTROLLING CHAOS IN PLASMA-FILLED DIODES

Peter A. Lindsay

Xiaodong Chen

John Watkins

Jianxin Zhang

28 February 2000

Final Technical Report

1 December 1996 – 30 November 1999

Prepared for: US Airforce Office of Scientific Research
801 Randolph Street
Arlington, VA 22203, USA

European Office of Aerospace Research and Development
223/231 Old Marylebone Road
London, NW1 5TH, UK

Contact No. F46920-97-I-0035

Prepared by: Department of Electronic Engineering
King's College London
Strand
London, WC2R 2LS, UK

DTIC QUALITY INSPECTED 3

DISTRIBUTION STATEMENT A

Approved for Public Release
Distribution Unlimited

20000315 018

28 Feb 2000

Final: 1 Dec 96 – 30 Nov 99

F46920 – 97 – I - 0035

Controlling Chaos in Plasma-filled Diodes

P A Lindsay

X Chen

J Watkins

J Zhang

AFOSR

801 Randolph Street
Arlington VA 22203 USA

EOARD

223/231 Old Marylebone Road
London NW1 5TH UK

REPORT DOCUMENTATION PAGE

0063

The public reporting burden for this collection of information is estimated to average 1 hour per response, including the gathering and maintaining the data needed, and completing and reviewing the collection of information. Send comments regarding this burden estimate or any other aspect of this collection of information, including suggestions for reducing the burden, to Department of Defense, Washington Headquarters, (0704-0188), 1215 Jefferson Davis Highway, Suite 1204, Arlington, VA 22202-4302. Respondents should be aware that notwithstanding any other provision of law, no person shall be subject to any penalty for failing to comply with a collection of information if it does not display a currently valid OMB control number.

PLEASE DO NOT RETURN YOUR FORM TO THE ABOVE ADDRESS.

1. REPORT DATE (DD-MM-YYYY) 28-02-2000	2. REPORT TYPE Final Technical	3. DATES COVERED (From - To) Dec 1996 - Nov 1999		
4. TITLE AND SUBTITLE CONTROLLING CHAOS IN PLASMA-FILLED DIODES		5a. CONTRACT NUMBER --		
		5b. GRANT NUMBER F46920-97-1-0035		
		5c. PROGRAM ELEMENT NUMBER --		
		5d. PROJECT NUMBER --		
		5e. TASK NUMBER --		
		5f. WORK UNIT NUMBER --		
7. PERFORMING ORGANIZATION NAME(S) AND ADDRESS(ES) King's College London 222 Strand London WC2R 2LS UK		8. PERFORMING ORGANIZATION REPORT NUMBER --		
9. SPONSORING/MONITORING AGENCY NAME(S) AND ADDRESS(ES) US Air Force Office of Scientific Research 801 Randolph Street, Arlington VA 22203 USA. European Office of Aerospace Research and Development, 223/231 Old Marylebone Rd. London NW1 5TH UK		10. SPONSOR/MONITOR'S ACRONYM(S) AFOSR/BOARD		
		11. SPONSOR/MONITOR'S REPORT NUMBER(S) --		
12. DISTRIBUTION/AVAILABILITY STATEMENT Approved for public release; distribution unlimited.				
13. SUPPLEMENTARY NOTES --				
14. ABSTRACT This Final Report covers the results of investigations extending over a three-year period: 1 Dec 96 - 30 Nov 99. The Report starts with a brief historical introduction to current investigations and a description of possible physical embodiments of the system. This is followed by a detailed discussion of the mathematical model of the system, the methods used in solving the corresponding integro-differential equations and some analytical solutions in the two accessible cases of a steady state and harmonic oscillations. The main body of the report is concerned with detailed analysis of the				
15. SUBJECT TERMS dynamical behaviour of the system and various methods of controlling chaos by a suitable adjustment of the plasma-filled relevant parameters of the system.				
16. SECURITY CLASSIFICATION OF: a. REPORT U b. ABSTRACT U c. THIS PAGE U		17. LIMITATION OF ABSTRACT UU	18. NUMBER OF PAGES	19a. NAME OF RESPONSIBLE PERSON Prof. P.A.Lindsay
				19b. TELEPHONE NUMBER (Include area code) +44 20 7882 5424/8995 9703

Contents

Summary	
1. Introduction	3
2. Possible mathematical models of the diode	6
3. Mathematical derivation of the Godfrey model, including load	8
4. Steady state solutions	13
5. Oscillatory solutions	18
6. Method of presentation of computational results, using a short-circuit diode as an example	23
7. Physical interpretation of the results	29
8. Computational results – AC currents and a load	33
8.1 Resistive load	33
8.2 Capacitive load	34
8.3 Inductive load	36
8.4 Inductance, Resistance and capacitance in series	37
8.4.1 Variable \hat{R} and \hat{C}	38
8.4.2 Fixed \hat{R} , variable \hat{L} and \hat{C}	39
8.4.3 A purely reactive \hat{L} and \hat{C} load	40
9. Computational results – AC + DC currents and a load	41
9.1 Resistive load	41
9.2 Resistance and inductance in series	43
10. Conclusion and suggestions for future work	46
Conclusions	47
Future work	50
Appendix 1: Notation	52
Appendix 2: Numerical solutions of the integral equations	55
Appendix 3: General observations on the effect of positive ions	60
References	67
Figures	72

Summary

This is the Final Report covering the results of investigations extending over a three-year period, 1 Dec 96 – 30 Nov 99. Following a brief summary of early investigations of the dynamic behaviour of a plane, plasma-filled diode, a detailed description of physical realisations of the system is then presented. The main part of the Report deals with the generation of oscillations and control of chaos. This is achieved by first carefully analysing the dynamic behaviour of the system as a function of three parameters: the ratio of ion/electron charge density at the entrance electrode $\hat{\alpha}$, the spatial separation of the electrodes \hat{x}_L and the load \hat{Z}_t . It is then indicated how the oscillations and the chaotic behaviour of the system can be controlled by a suitable adjustment of the above parameters. The report ends with suggestions for future work based on the results of the above investigations.

It should be added that the above investigations generated two special issue papers and six contributions at various conferences.

1. Introduction

The problem of interaction between electron beams and positively charged ions acquired some significance in the late fifties of the last century when it was realised that the interaction process may lead to the generation and amplification of microwave radiation [1-6]), the results of these investigations being extensively summarised by R. J. Briggs [7]. Although the interaction process was very efficient (say $\sim 60\text{db/cm}$ TWT amplification), actual devices failed to materialise largely due to unacceptable noise levels and practical problems associated with input and output coupling. However interest in the dynamics of plasma by no means abated, largely due to the related work associated with the development of fusion devices. More recently the development of high power sources of microwave radiation such as the VIRCATOR, brought the problem of electron beam/plasma interaction again into focus [8-10].

Let us now consider in more detail the actual system we are going to investigate. In principle there are two different models that are referred to as a 'plasma-filled diode'. The first model, shown in Fig. 1, comprises three electrodes, the middle one being a permeable grid G which is common to both sections. The first section, Region I, acts as a space-charge-limited diode, its purpose being to generate a space-charge-limited current, the corresponding current density being given by the usual expression

$$-J_{\text{spl}} = \frac{4}{9} \epsilon_0 \sqrt{\frac{2e}{m_0}} \frac{\phi_0^{3/2}}{d_0^2} \quad (1.1)$$

The second section, the actual 'plasma-filled diode' to be investigated, Region II, uses the grid G as an entrance electrode, the electrons being collected by the third electrode

usually called the anode A. Since the grid G is kept at a constant potential ϕ_0 relative to the cathode C, the electron velocity at the entrance electrode is given by

$$v_0 = \sqrt{2e\phi_0 / m_0} \quad (1.2)$$

Frequently, for the sake of brevity, only the second half marked II is shown in the literature, the electron beam entering the diode from 'outside' through a permeable entrance electrode, but it is worth reminding ourselves that such representation is incomplete, the only physically realisable unit being that shown in Fig. 1.

The second model is shown in Fig. 2. Here we have four electrodes, a cathode C, two permeable grids G1 and G2 and an anode A. This arrangement makes it possible to separate the DC and AC components of the current, somewhat along the lines of similar arrangements in many microwave tubes. Here the C-G1 section, Region I, is again intended to act as a space-charge-limited diode, the grid G1 being kept at a constant potential ϕ_0 relative to the cathode so that the electrons again reach velocity v_0 at that point. The 'plasma-filled diode' under consideration is now contained between the two grids, G1 and G2, Region II, respectively acting as entrance and exit electrodes; both grids are assumed to be totally permeable to the electrons. The electron beam now passes Region III and is collected by the fourth electrode A. In this arrangement only the AC component of the total current can flow through the load Z_t , the DC component reaching the anode A which acts as a 'collector'; this electrode is directly connected to the battery, the connection by-passing the diode load Z_t . Here it is assumed that a complete separation of the AC and DC components of the total current can be achieved.

When a plasma-filled diode is short-circuited ($Z_t = 0$), there is little to choose between Fig. 1 and 2 [11-15]. However when the diode has a load connected across its

electrodes, the dynamic behaviour can be substantially different in the two cases. For example in the case of Fig. 1 the load Z_t must not contain a series capacitance, since that would amount to an open circuit for DC currents. There is no such restriction in the case of Fig. 2, since the DC path by-passes the load Z_t . In our investigations we have used both systems in order to be able to compare the results which can be obtained in the two cases [16-19, 24, 25, 48].

It is generally assumed that due to the difference in mass between ions and electrons, the ions remain immobile, at least for the first few nanoseconds of operation of the diode. We have accepted this assumption as being quite reasonable. Perhaps one ought to add that some authors prefer to assume that electrons and positive ions move together so that the DC component of the total current is fully neutralised, or alternatively that neutralisation is achieved by external current sources [20-22], but we have avoided making such assumptions since they appeared to us to be somewhat artificial, although mathematically convenient.

Finally one should mention that other authors choose to consider a closely related system shown in Fig. 3, which in effect is a Q-machine [17,23]. Here both power supplies and a load directly connect across a plasma-filled diode. This means that now most of the potential drop occurs across the two sheaths situated next to the electrodes. Although in some circumstances such a system can be used to model a Pierce diode, we have felt that those shown in Figs. 1 and 2 are simpler and therefore preferable for the purpose of our investigations.

2. Possible mathematical models of the diode

The Report is primarily limited to the investigation of a plasma-filled diode, Region II in Figs.1 and 2. In analysing the diode we can adopt in principle three different mathematical approaches. The oldest is that due to Birdsall et al. [26,27], where the electron stream is represented by a series of infinitely thin electron sheets. This approach has been discussed by us at some length and used in our earlier investigations of the dynamic behaviour of the diode [28]. Although the method is quite effective, it suffers from the usual problems associated with discretisation of a continuous flow; this becomes particularly awkward when the sheets begin to overtake each other, or change their direction of motion, although in some more recent versions of the method attempts have been made to overcome this problem [29,30]. The second approach to the problem is that initially developed by B. B. Godfrey [14] and then extended to systems lacking charge balance at the entrance electrode by others [16]. The method is based on the derivation of a pair of coupled integro-differential equations of the Volterra type, their solution providing the field at the entrance electrode \hat{E}_0 and the transit time $\hat{\tau}_L$ as functions of time. This information is adequate for the derivation of electric field \hat{E} as a function of the interelectrode distance \hat{x} , provided the fixed parameters of the system such as the electron/ion charge ratio $\hat{\alpha}$ at the entrance electrode and the electrode separation \hat{x}_L are known. Godfrey's approach has been considered by us to be preferable in our investigation of the dynamic behaviour of a plasma-filled diode. The third approach is based on a powerful code called MAGIC2D/3D which is a PIC Finite-Difference Time-Domain computer code of great versatility [31,32]. Further comments on possible

applications of the code to the analysis of the whole system, including all three regions of Figs 1 and 2 can be found in the last section of the Report where proposals for future work are being discussed.

3. Mathematical derivation of the Godfrey model, including load

In deriving the integral equations we start, following B.B. Godfrey [14], with the usual set of partial differential equations, all in 1-D:

$$\partial_{\hat{x}} \hat{E} = \partial_{\hat{x}\hat{x}}^2 \hat{\phi} = \hat{\rho}_e - \hat{\alpha} = \hat{\rho} \quad \text{Poisson's eq.} \quad (3.1)$$

$$d_{\hat{t}} \hat{x} = d_{\hat{t}} \hat{v} = \partial_{\hat{t}} \hat{v} + \hat{v} \partial_{\hat{x}} \hat{v} = \hat{E} \quad \text{Equation of motion} \quad (3.2)$$

$$\partial_{\hat{x}} \hat{J}_{\text{tot}} = \partial_{\hat{x}} (\hat{J}_c + \hat{J}_d) = \partial_{\hat{x}} (\hat{\rho}_e \hat{v} + \partial_{\hat{t}} \hat{E}) = 0 \quad \text{Continuity eq. for} \quad (3.3)$$

the *total* current density

The 'hat' variables used throughout the Report are defined in Appendix 1. Partial derivatives with respect to \hat{t} are deliberately included in order to allow for possible oscillatory and chaotic behaviour of the system. It is to be noted that since the positive ions are assumed to be immobile, they affect the Poisson equation (3.1) where $\hat{\rho} = \hat{\rho}_e + \hat{\rho}_i = \hat{\rho}_e - \hat{\alpha}$, but not the continuity equation (3.3) where $\hat{J}_c = \hat{\rho}_e \hat{v}$ and *not* $\hat{\rho} \hat{v}$. Consequently our model is valid for the first few nanoseconds, before the ions are able to move under the influence of the electric field set up between the electrodes. Substituting from (3.1) and remembering that in 1-D

$$d_{\hat{t}} \hat{E} = \partial_{\hat{t}} \hat{E} + \hat{v} \partial_{\hat{x}} \hat{E} \quad (3.4)$$

we obtain from (3.3):

$$\partial_{\hat{x}} \hat{J}_{\text{tot}} = \partial_{\hat{x}} (\hat{\rho}_e \hat{v} + \partial_{\hat{t}} \hat{E}) = \partial_{\hat{x}} \{(\partial_{\hat{x}} \hat{E} + \hat{\alpha}) \hat{v} + \partial_{\hat{t}} \hat{E}\} = \partial_{\hat{x}} \{d_{\hat{t}} \hat{E} + \hat{\alpha} d_{\hat{t}} \hat{x}\} = 0 \quad (3.5)$$

Integrating with respect to \hat{x} we now obtain:

$$\hat{J}_{\text{tot}} = d_{\hat{t}} (\hat{E} + \hat{\alpha} \hat{x}) = (\hat{J}_{\text{tot}})_{\hat{x}=0} = \hat{\rho}_{e0} \hat{v}_0 + (\partial_{\hat{t}} \hat{E})_{\hat{x}=0} = 1 + d_{\hat{t}} \hat{E}_0(\hat{t}) \quad (3.6)$$

since at the entrance electrode $\hat{\rho}_{e0} \hat{v} = 1$ and $(\partial_{\hat{t}} \hat{E}(\hat{x}, \hat{t}))_{\hat{x}=0} = d_{\hat{t}} \hat{E}(0, \hat{t}) = d_{\hat{t}} \hat{E}_0(\hat{t})$.

Integrating with respect to \hat{t} and substituting from (3.2) we finally obtain:

$$\hat{E} + \hat{\alpha} \hat{x} = d_{\hat{t}}^2 \hat{x} + \hat{\alpha} \hat{x} = \hat{E}_0(\hat{t}) + (\hat{t} - \hat{t}_1) \quad (3.7)$$

Here the boundary conditions have been suitably chosen, so that at $\hat{x} = 0, \hat{t} = \hat{t}_1$, i.e. at the entrance electrode, $(d_{\hat{t}}^2 \hat{x})_{\hat{x}=0} = \hat{E}_0(\hat{t}_1)$ where, as before, $\hat{E}_0(\hat{t}) = \hat{E}(0, \hat{t})$ is the time-dependent value of the electric field at the entrance electrode.

In principle (3.2) and (3.7) together with suitable boundary conditions should be adequate to define the dynamical properties of the system shown in Figs 1 and 2. However, attempts at numerical solutions of the above equations in their differential form were not very effective and therefore it proved better to convert the differential equations into a pair of coupled integral equations, as shown elsewhere for $\hat{\alpha} = 1$ [14]; this approach was then extended to $\hat{\alpha} \neq 1$ by others [16, 39].

In order to describe the system in terms of integral equations we note, first of all, that the homogeneous form of (3.7), i.e. when the driving term $\hat{E}_0(\hat{t}) + (\hat{t} - \hat{t}_1) = 0$, has a solution given by

$$\hat{x} = \sin\{\hat{\alpha}^{1/2}(\hat{t} - \hat{t}')\} \quad (3.8)$$

This suggests that $\sin\{\hat{\alpha}^{1/2}(\hat{t} - \hat{t}')\}$ could be used as a kernel in our integral equations. Thus multiplying the left hand side of (3.7) by $\sin\{\hat{\alpha}^{1/2}(\hat{t} - \hat{t}')\}$ and integrating from $\hat{t}' = \hat{t}_1$ to $\hat{t}' = \hat{t}$ we first obtain, using integration by parts,

$$\int_{\hat{t}_1}^{\hat{t}} \frac{d^2\hat{x}}{d\hat{t}'^2} \sin\{\hat{\alpha}^{1/2}(\hat{t} - \hat{t}')\} d\hat{t}' + \hat{\alpha} \int_{\hat{t}_1}^{\hat{t}} \hat{x} \sin\{\hat{\alpha}^{1/2}(\hat{t} - \hat{t}')\} d\hat{t}' = -\sin\{\hat{\alpha}^{1/2}(\hat{t} - \hat{t}_1)\} + \hat{\alpha}^{1/2} \hat{x} \quad (3.9)$$

In the process the term $\hat{\alpha}^{1/2} \int_{\hat{t}_1}^{\hat{t}} \frac{d\hat{x}}{d\hat{t}'} \cos\{\hat{\alpha}^{1/2}(\hat{t} - \hat{t}')\} d\hat{t}'$ appears twice, but with opposite sign. Using simple integration we can also write for the last term on the right hand side of (3.7)

$$\int_{\hat{t}_1}^{\hat{t}} (\hat{t} - \hat{t}') \sin\{\hat{\alpha}^{1/2}(\hat{t} - \hat{t}')\} d\hat{t}' = -\frac{1}{\hat{\alpha}} \sin\{\hat{\alpha}^{1/2}(\hat{t} - \hat{t}_1)\} + \frac{1}{\hat{\alpha}^{1/2}} (\hat{t} - \hat{t}_1) \quad (3.10)$$

Collecting all the terms we now obtain in place of (3.7)

$$\hat{x}(\hat{t}) = \frac{1}{\hat{\alpha}} (\hat{t} - \hat{t}_1) - \frac{1 - \hat{\alpha}}{\hat{\alpha}^{3/2}} \sin\{\hat{\alpha}^{1/2}(\hat{t} - \hat{t}_1)\} + \frac{1}{\hat{\alpha}^{1/2}} \int_{\hat{t}_1}^{\hat{t}} \hat{E}_0(\hat{t}') \sin\{\hat{\alpha}^{1/2}(\hat{t} - \hat{t}')\} d\hat{t}' \quad (3.11)$$

In order to obtain an expression for the electric field $\hat{E}(\hat{t})$ as a function of time we differentiate (3.11) twice with respect to time, substituting at one point from (3.2); we then obtain

$$\hat{E}(\hat{t}) = \hat{E}_0(\hat{t}) + \frac{1 - \hat{\alpha}}{\hat{\alpha}^{1/2}} \sin\{\hat{\alpha}^{1/2}(\hat{t} - \hat{t}_1)\} - \hat{\alpha}^{1/2} \int_{\hat{t}_1}^{\hat{t}} \hat{E}_0(\hat{t}') \sin\{\hat{\alpha}^{1/2}(\hat{t} - \hat{t}')\} d\hat{t}' \quad (3.12)$$

Since we are dealing with integral equations it is now necessary to introduce suitable boundary conditions: the (reduced) separation of the electrodes given by $\hat{x}_L = (\omega_{pe} / v_0) x_L$ and the (reduced) potential difference between the exit and entrance electrodes $\hat{\phi}_e = \hat{\phi}_L - \hat{\phi}_0$. We can express the latter in terms of the electric field.

$$\hat{\phi}_e = \hat{\phi}_L - \hat{\phi}_0 = \int_0^{\hat{x}_L} \hat{E} d\hat{x} \quad (3.13)$$

In the case of \hat{x}_L we note that at the exit electrode $\hat{x} = \hat{x}_L$ and $\hat{t} - \hat{t}_1 = \hat{t}_L - \hat{t}_1 = \hat{\tau}_L$, so that we can introduce the boundary conditions directly in (3.11) by simply writing

$$\hat{x}_L = \frac{1}{\hat{\alpha}} \hat{\tau}_L - \frac{1 - \hat{\alpha}}{\hat{\alpha}^{3/2}} \sin(\hat{\alpha}^{1/2} \hat{\tau}_L) + \frac{1}{\hat{\alpha}^{1/2}} \int_{\hat{t}_1 - \hat{\tau}_L}^{\hat{t}} \hat{E}_0(\hat{t}') \sin\{\hat{\alpha}^{1/2}(\hat{t} - \hat{t}')\} d\hat{t}' \quad (3.14)$$

It is to be noted that although \hat{x}_L is a constant, the reduced transit time of an electron is a function of time, $\hat{\tau}_L = \hat{\tau}_L(\hat{t})$ and depends on the field distribution between the electrodes. Thus (3.14) contains two unknown functions of time, $\hat{\tau}_L(\hat{t})$ and $\hat{E}_0(\hat{t})$.

The situation is more complicated in the case of (3.12) since the electric potential $\hat{\phi}$ does not appear in the equation and we have to reinterpret $\hat{\phi}_e$ in terms of the electric field, as indicated in (3.13). As a first step we substitute (3.7) in (3.13) and write

$$\hat{\phi}_e = \int_0^{\hat{x}_L} \hat{E} d\hat{x} = \int_0^{\hat{x}_L} \{\hat{E}_0(\hat{t}) - \hat{\alpha} \hat{x} + (\hat{t} - \hat{t}_1)\} d\hat{x} = \hat{E}_0(\hat{t}) \hat{x}_L - \frac{1}{2} \hat{\alpha} \hat{x}_L^2 + \int_0^{\hat{x}_L} (\hat{t} - \hat{t}_1) d\hat{x} \quad (3.15)$$

Differentiating (3.11) with respect to \hat{t}_1 , which is the moment an electron passes the entrance electrode G or G1, we obtain

$$\frac{d\hat{x}}{d\hat{t}_1} = -\frac{1}{\hat{\alpha}} + \frac{1 - \hat{\alpha}}{\hat{\alpha}} \cos\{\hat{\alpha}^{1/2}(\hat{t} - \hat{t}_1)\} - \frac{1}{\hat{\alpha}^{1/2}} \hat{E}_0(\hat{t}_1) \sin\{\hat{\alpha}^{1/2}(\hat{t} - \hat{t}_1)\} \quad (3.16)$$

Using (3.16) we can now write the last term of (3.15) in the following form

$$\begin{aligned} \int_0^{\hat{x}_L} (\hat{t} - \hat{t}_1) d\hat{x} &= \int_{\hat{t}_1}^{\hat{t} - \hat{\tau}_L} (\hat{t} - \hat{t}_1) \frac{d\hat{x}}{d\hat{t}_1} d\hat{t}_1 \\ &= - \int_{\hat{t}_1}^{\hat{t} - \hat{\tau}_L} (\hat{t} - \hat{t}_1) \left[\frac{1}{\hat{\alpha}} - \frac{1 - \hat{\alpha}}{\hat{\alpha}} \cos\{\hat{\alpha}^{1/2}(\hat{t} - \hat{t}_1)\} + \frac{1}{\hat{\alpha}^{1/2}} \hat{E}_0(\hat{t}_1) \sin\{\hat{\alpha}^{1/2}(\hat{t} - \hat{t}_1)\} \right] d\hat{t}_1 \\ &= \frac{1}{2\hat{\alpha}} \hat{\tau}_L^2 + \frac{1 - \hat{\alpha}}{\hat{\alpha}} \left[\frac{1}{\hat{\alpha}} - \frac{1}{\hat{\alpha}} \cos(\hat{\alpha}^{1/2} \hat{\tau}_L) - \frac{\hat{\tau}_L}{\hat{\alpha}^{1/2}} \sin(\hat{\alpha}^{1/2} \hat{\tau}_L) \right] \end{aligned}$$

$$+ \frac{1}{\hat{\alpha}^{1/2}} \int_{\hat{t}-\hat{\tau}_L}^{\hat{t}} \hat{E}_0(\hat{t}') (\hat{t} - \hat{t}') \sin\{\alpha^{1/2}(\hat{t} - \hat{t}')\} d\hat{t}' \quad (3.17)$$

Combining (3.15) and (3.17) we finally obtain

$$\begin{aligned} -\hat{\phi}_t + \hat{E}_0(\hat{t}) \hat{x}_L &= \frac{1}{2} (\hat{\alpha} \hat{x}_L^2 - \frac{1}{\hat{\alpha}} \hat{\tau}_L^2) + \frac{1 - \hat{\alpha}}{\hat{\alpha}^{3/2}} \left[\hat{\tau}_L \sin(\hat{\alpha}^{1/2} \hat{\tau}_L) - \frac{1}{\hat{\alpha}^{1/2}} \{1 - \cos(\alpha^{1/2} \hat{\tau}_L)\} \right] \\ &\quad - \frac{1}{\hat{\alpha}^{1/2}} \int_{\hat{t}-\hat{\tau}_L}^{\hat{t}} \hat{E}_0(\hat{t}') (\hat{t} - \hat{t}') \sin\{\alpha^{1/2}(\hat{t} - \hat{t}')\} d\hat{t}' \end{aligned} \quad (3.18)$$

In the case of a short-circuited diode $\hat{\phi}_t = 0$ and the coupled pair of integral equations (3.14), (3.18) fully describe the dynamic behaviour of the system. The equations are of the Volterra type with an additional difficulty that not only the variable \hat{t} but also the function $\hat{\tau}_L(\hat{t})$ appear in the limits of integration in both equations. In the absence of standard procedures a special computer code has been developed for the solution of the equations, as described in Appendix 2.

In the presence of a load the next step is to relate the potential difference $\hat{\phi}_t = \hat{\phi}_L - \hat{\phi}_0$ to the external current I using the concept of the continuity of current. The latter requires that, bearing in mind the usual sign convention for electron beam currents, the current in the circuit must be equal to the total current flowing inside the diode

$$-I = I_{\text{tot}} = AJ_{\text{tot}} \quad (3.19)$$

where A is the area of the electrodes. But we know from (3.3) that in a 1-D system J_{tot} remains constant so that

$$J_{\text{tot}} = J_c + J_d = J_{c0} + J_{d0} = \rho v + \varepsilon_0 \partial_t E = \rho_0 v_0 + \varepsilon_0 \partial_t E_0 = J_{\text{tot},0} \quad (3.20)$$

We can also see from Figs. 1 and 2 that in our case both v_0 and $J_{c0} = \rho_0 v_0$, the initial boundary conditions, remain constant so that at the entrance electrode all the AC phenomena are solely expressed by time variation of the electric field E_0 . We can thus write

$$-d_t I = d_t I_{\text{tot}} = d_t I_{\text{tot},0} = Ad_t J_{\text{tot},0} = A\varepsilon_0 \partial_t E_0 \quad (3.21)$$

In the system shown in Fig. 1 both DC and AC components of the current flow through the load so that in the case of a series connection we must omit the capacitor. We can

then write the following expression for the potential difference $\hat{\phi}_t$ across the diode and hence across the external load Z_t

$$\begin{aligned}\hat{\phi}_t &= -Z_t I = Z_t I_{\text{tot}} = Z_t A J_{\text{tot}} = Z_t A J_{\text{tot},0} \\ &= (L d_t J_{\text{tot},0} + R J_{\text{tot},0}) A \\ &= \{(L \varepsilon_0 \partial_{tt} E_0 + R(\rho_0 v_0 + \varepsilon_0 \partial_t E_0)) A\}\end{aligned}\quad (3.22)$$

where we have used (3.20) and (3.21) in the last line of (3.22). In terms of the reduced variables (see Appendix 1) we now have in place of (3.22)

$$\hat{\phi}_t = -\hat{x}_L \hat{Z}_t \hat{J}_{\text{tot}} = -\hat{x}_L \{\hat{R} + (\hat{L} \hat{D}^2 + \hat{R} \hat{D}) \hat{E}_0\} \quad (3.23)$$

where $\hat{L} = L C_v \omega_{pe}^2$, $\hat{R} = R C_v \omega_{pe}$, $C_v = A \varepsilon_0 / d$ (3.24)

and $\hat{D} \equiv d_t = d / dt$; here we use d for the separation of the electrodes in order to distinguish it from the inductance L . In the case of Fig. 1 the expression (3.23) should now be substituted in (3.18) in place of $-\hat{\phi}_t$.

In considering the system shown in Fig. 2 we note that only the AC component of the current flows through the load Z_t so that the load may now contain capacitance, resistance and inductance in series. Thus in place of (3.22) we can write

$$\begin{aligned}\hat{\phi}_t &= -Z_t I = Z_t I_{\text{tot}} = Z_t A J_{\text{tot}} = Z_t A J_{\text{tot},0} \\ &= (L d_t J_{\text{tot},0} + R J_{\text{tot},0} + \frac{1}{C} \int J_{\text{tot},0} dt) A \\ &= (L \varepsilon_0 \partial_{tt} E_0 + R \varepsilon_0 \partial_t E_0 + \frac{1}{C} \varepsilon_0 E_0) A\end{aligned}\quad (3.25)$$

where again we have substituted from (3.20) and (3.21) in the last line of (3.25), noting at the same time that at the entrance electrode the conduction current $J_{c0} = \rho_0 v_0$ has no AC component. In terms of the reduced variables we have in place of (3.25)

$$\hat{\phi}_t = -\hat{x}_L \hat{Z}_t \hat{J}_{\text{tot}} = -\hat{x}_L \{\hat{L} \hat{D}^2 + \hat{R} \hat{D} + \frac{1}{\hat{C}}\} \hat{E}_0 \quad (3.26)$$

where

$$\hat{C} = C / C_v \quad (3.27)$$

In the case of Fig. 2 the expression (3.26) should now be substituted in (3.18) in place of $-\hat{\phi}_t$.

4. Steady state solutions

The coupled pair of integral equations (3.14), (3.18) describing the dynamics of the system are by no means easy to interpret, especially in the presence of a load. It seemed prudent therefore to consider one of the few cases which can be solved analytically, namely that of a steady state.

At this point it is helpful to consider very briefly the general effect that the introduction of positive ions has on the dynamic behaviour of the system, Appendix 3. The main conclusion is that for $\hat{\alpha} = 0$ (no ions) the solutions are always nonperiodic, so that the system at most can sustain only a single minimum in the potential distribution function. When $\hat{\alpha} \neq 0$ (ions present) this is no longer the case, the solutions *can now be periodic* in character and therefore several intercalated minima and maxima in the potential function can now exist (see also a much more elaborate discussion of this point in ref. [33]).

In general, the two independent variables \hat{x} and \hat{t} must be carefully distinguished, as indicated in (3.1)-(3.3), where there is a clear distinction between the partial derivatives with respect to \hat{x} and \hat{t} . In a steady state \hat{t} ceases to be independent of \hat{x} and it can then be used *in place* of \hat{x} , the corresponding equations frequently acquiring a simpler form when expressed in terms of \hat{t} rather than \hat{x} . We also find that in the case of a steady state both $\hat{\tau}_L$ and \hat{E}_0 appearing in (3.14) and (3.18) no longer vary with time, but become constants of integration. We then find that the integrations indicated in (3.14), (3.18) can be carried out without difficulty and we obtain for $\hat{\alpha} = 1$

$$\hat{x}_L = \hat{\tau}_L + \hat{E}_0(1 - \cos \hat{\tau}_L) \quad (4.1)$$

$$\hat{\phi}_\ell = \hat{E}_0 \hat{x}_L + \frac{1}{2}(\hat{\tau}_L^2 - x_L^2) + \hat{E}_0(\sin \hat{\tau}_L - \hat{\tau}_L \cos \hat{\tau}_L) \quad (4.2)$$

Substituting from (4.1) for $\hat{\tau}_L$ and $\hat{\tau}_L^2$, we find that (4.2) can be further simplified to read

$$\hat{\phi}_\ell = \hat{E}_0 \sin \hat{\tau}_L [1 + \frac{1}{2} \hat{E}_0 \sin \hat{\tau}_L] \quad (4.3)$$

We now note that for a steady state and $\hat{\alpha} = 1$ the system is fully described by (4.1) and (4.3), in place of the more formidable integro-differential equations (3.14), (3.18). Here

$\hat{\alpha} = 1$ has been chosen for the sake of clarity in interpreting the physical content of the equations.

In the case of a steady state, we have $\partial_{\hat{x}} = d_{\hat{x}}$ and consequently

$$d_{\hat{t}} \hat{E} = \hat{v} d_{\hat{x}} \hat{E} \quad (4.4)$$

Multiplying (3.1) by \hat{v} , substituting from (3.2) and noting that in a steady state $d_{\hat{t}}(\hat{\rho}_e \hat{v}) = d_{\hat{t}} \hat{J}_e = 0$, we obtain for $\hat{\alpha} = 1$

$$d_{\hat{t}} \hat{E} + \hat{E} = 0 \quad (4.5)$$

Solving (4.5) for $d_{\hat{t}} \hat{E}_0 = 0$ we now have

$$\hat{E} = \hat{E}_0 \sin(\hat{t} - \hat{t}_1) \quad (4.6)$$

since from (3.1) and (4.4) $d_{\hat{t}} \hat{E}_0 = 0$ for $\hat{\alpha} = 1$ (charge balance at the entrance electrode).

Writing $\hat{E} = d_{\hat{x}} \hat{x}$ we then obtain from (4.6) by simple integration

$$\hat{v} = d_{\hat{t}} \hat{x} = 1 + \hat{E}_0 \sin(\hat{t} - \hat{t}_1) \quad (4.7)$$

$$\hat{x} = (\hat{t} - \hat{t}_1) + \hat{E}_0 \{1 - \cos(\hat{t} - \hat{t}_1)\} \quad (4.8)$$

where the corresponding boundary conditions are: $\hat{x} = 0$ and $\hat{v} = \hat{v}_0 = 1$ at $\hat{t} = \hat{t}_1$. At the exit electrode we have $\hat{x} = \hat{x}_L$ and $\hat{t}_L - \hat{t}_1 = \hat{t}_L$, so that (4.8) now becomes (4.1), both equations defining the relationship between \hat{x} and \hat{t} in the case of a steady state since, as we have mentioned, \hat{x} and \hat{t} are then no longer independent. It has also been pointed out that the use of \hat{t} in place of \hat{x} often leads to simpler expressions. In our case eliminating \hat{t} between (4.6) and (4.8) leads to an expression for $\hat{E}(\hat{x})$ which is much more involved than $\hat{E}(\hat{t})$ shown in (4.6).

So far we have briefly summarized the results presented elsewhere [14,34] in order to emphasize the physical content of (4.1); let us now consider (4.3) which, in the form shown above, arises only in the presence of a load. At this stage it is best to re-derive (4.3) directly from the definition of $\hat{E} = d_{\hat{x}} \hat{\phi}$, noting at the same time the positive sign due to the use of reduced variables, (A1.1) in Appendix 1. Thus, we can write:

$$\hat{\phi}_L = \hat{\phi}_L - \hat{\phi}_0 = \int_0^{\hat{x}_L} \hat{E} d\hat{x} = \hat{E}_0 \int_0^{\hat{x}_L} \cos(\hat{t} - \hat{t}_1) d\hat{x} = \hat{E}_0 \int_{\hat{t}_1}^{\hat{t}_L} \frac{d\hat{x}}{d\hat{t}} \cos(\hat{t} - \hat{t}_1) d\hat{t}$$

$$\begin{aligned}
&= \hat{E}_0 \int_{\hat{t}_1}^{\hat{x}_L} \{1 + \hat{E}_0 \sin(\hat{t} - \hat{t}_1)\} \cos(\hat{t} - \hat{t}_1) d\hat{t} \\
&= \hat{E}_0 \sin \hat{\tau}_L \{1 + \frac{1}{2} \hat{E}_0 \sin \hat{\tau}_L\}
\end{aligned} \tag{4.9}$$

which is the same as (4.3). Thus the two identical expression (4.3) and (4.9), simply relate the potential difference between the electrodes $\hat{\phi}_e$ to the transit time $\hat{\tau}_L$ and the electric field at the entrance electrode \hat{E}_0 . It should be noted that in the case of a steady state \hat{x}_L , $\hat{\tau}_L$, \hat{E}_0 and $\hat{\phi}_e$ are all constants; in the more general case discussed in Section 3, where the dynamic behaviour of the system is determined by the integro-differential equations (3.14) and (3.18), only $\hat{x}_L = \omega_{pe}L/v_0$ is a constant, the remaining variables being functions of time: $\hat{\tau}_L(\hat{t})$, $\hat{E}_0(\hat{t})$ and $\hat{\phi}_e(\hat{t})$. The spatial distribution of \hat{E} (or $\hat{\phi}$) will then vary as time progresses, each individual snapshot requiring separate computations.

In the case of a steady state the load can only affect the dynamic behaviour of the system shown in Fig. 1, the only possible choice being a pure resistance \hat{R} . In a system shown in Fig. 2 the DC component of the current is assumed to by-pass the load so that in a steady state, when the AC component of current does not exist by definition, the load would have no effect, the system being effectively short-circuited. Omitting the time dependent terms in (3.23) we now obtain, substituting for $\hat{\phi}_e$ in (4.9)

$$-\hat{x}_L \hat{R} = \hat{E}_0 \sin \hat{\tau}_L \{1 + \frac{1}{2} \hat{E}_0 \sin \hat{\tau}_L\} \tag{4.10}$$

The two equations, (4.1) and (4.10), are sufficient for the computation of a dispersion equation shown in Fig. 4. The best procedure in this case is to assume a fixed value for \hat{R} and then eliminate \hat{x}_L ; this leaves us with a relationship between \hat{E}_0 and $\hat{\tau}_L$ given by $F(\hat{E}_0, \hat{\tau}_L) = 0$. Assuming a value for \hat{E}_0 we can then solve a rather awkward transcendental equation in order to obtain $\hat{\tau}_L$; substituting this value back in (4.1) finally gives us the required relationship between \hat{E}_0 and $\hat{\tau}_L$.

In the case of a short-circuited diode $\hat{R} = 0$ and, as is well known, the solution of (4.10) is given by $\hat{E}_0 = 0$ or $\sin \hat{\tau}_L = 0$. Substitution of these results in (4.1) then gives an intercalated set of sloping and vertical straight lines, as is shown in Fig. 4, the dispersion curve in this case being periodic with period 2π . The periodicity of the dispersion curve mirrors the periodicity of the boundary conditions in a short-circuited diode. This is no longer the case in the presence of a load, the potential of the two electrodes now being different. Therefore it should not surprise us that the corresponding dispersion curves also lack periodicity. It is also clear from (4.10) that in the presence of a load the field at the entrance electrode \hat{E}_0 can never be equal to zero, except for $\hat{x}_L = 0$. This is simply due to the fact that for $\hat{\alpha} = 1$ we also have $(\partial_{\hat{x}} \hat{E})_{\hat{x}=0} = 0$ at the entrance electrode and there is no mechanism for the electrons to be decelerated, in order to land on the exit electrode with a velocity $\hat{v}_L < \hat{v}_0 = 1$, as would be required for $\hat{\phi}_L = \hat{\phi}_L - \hat{\phi}_0 < 0$.

In addition to the case of a short-circuited diode, we have shown in Fig. 4 the effect of a resistive load $\hat{R} = 0.01, 0.05$ and 0.1 , inductive loads having no effect and capacitive loads not being permitted in the case of a steady state, i.e. DC currents, Fig. 1. We now find that the new dispersion curves neatly fit into spaces bordered by the straight lines of the $\hat{R} = 0$ case. As \hat{R} increases the curves gradually become more obviously non-periodic and move further away from the $\hat{R} = 0$ straight lines. This trend can be better understood with the help of Figs. 5 and 6 where we have respectively a graphical representation of the RHS of (4.10) and of \hat{E}_0 as a function of $\hat{\tau}_L$ rather than \hat{x}_L , as shown in Fig. 4. Eliminating \hat{x}_L between (4.1) and (4.10) we obtain

$$-\hat{R}\{\hat{\tau}_L + \hat{E}_0(1 - \cos \hat{\tau}_L)\} = \hat{E}_0 \sin \hat{\tau}_L \{1 + \frac{1}{2}\hat{E}_0 \sin \hat{\tau}_L\} \quad (4.11)$$

Thus the dispersion equation in terms of $\hat{\tau}_L$, i.e. $\hat{E}_0(\hat{\tau}_L)$, can be obtained by finding the points of cross-section between the curves shown in Fig. 5 which are the RHS of (4.11) and a straight line with a 'wobble' due to the cosine term, the LHS of (4.11), the slope of the line being governed by the value of the load \hat{R} . For a given \hat{E}_0 and $\hat{R} \neq 0$, this line can never cut all the loops extending into infinity of the curves shown in Fig. 5, hence the

lack of periodicity shown in Figs. 4 and 6. Furthermore, as \hat{R} increases, the number of loops intercepted by the line steadily decreases, steady-state solutions then being possible only for successively lower values of \hat{x}_L , i.e. for closer separation of the electrodes or lower injection current densities defined by ω_{pe} (see A 1.1). Finally steady-state solutions cease to exist when \hat{R} is sufficiently large for a virtual cathode to appear at the exit electrode, when $\hat{\phi}_L = 0$ or $\hat{\phi}_t = -\frac{1}{2}$. Once the curves of Fig. 6 have been obtained it is quite straightforward with the help of (4.1) to convert them to those of Fig. 4 where \hat{E}_0 is shown as a function of \hat{x}_L .

Naturally the above computations provide no information on the stability of the various branches of the dispersion curve for $\hat{R} \neq 0$, as shown in Fig. 4. Judging by analogy with dispersion curves for $\hat{R} = 0$ (Fig. 3 in ref.14) one would expect stable branches for $\hat{E}_0 > 0$, the opposite being true for $\hat{E}_0 < 0$.

5. Oscillatory solutions

There is one more case which can be considered analytically, viz. that of harmonic oscillations. Assuming that the electric field at the entrance electrode varies with time as

$$\hat{E}_0(\hat{t}) = \hat{E}_{01} \cos \hat{\omega} \hat{t} \quad (5.1)$$

and substituting (5.1) in (3.14) and (3.18), we can now carry out the necessary integrations and obtain

$$\hat{x}_L = \hat{\tau}_L + \hat{E}_{01} \left[c \left(\frac{1-c_-}{2(1-\hat{\omega})} + \frac{1-c_+}{2(1+\hat{\omega})} \right) + s \left(\frac{s_-}{2(1-\hat{\omega})} - \frac{s_+}{2(1+\hat{\omega})} \right) \right] \quad (5.2)$$

$$\begin{aligned} \hat{\phi}_L = & \hat{x}_L \hat{E}_{01} c - \frac{1}{2} \hat{x}_L^2 + \frac{1}{2} \hat{\tau}_L^2 + \hat{E}_{01} \left[c \left(\frac{s_- - (1-\hat{\omega})\hat{\tau}_L c_-}{2(1-\hat{\omega})^2} + \frac{s_+ - (1-\hat{\omega})\hat{\tau}_L c_+}{2(1+\hat{\omega})^2} \right) \right. \\ & \left. + s \left(\frac{c_- - 1 + (1-\hat{\omega})\hat{\tau}_L s_-}{2(1-\hat{\omega})^2} - \frac{c_+ - 1 + (1+\hat{\omega})\hat{\tau}_L s_+}{2(1+\hat{\omega})^2} \right) \right] \quad (5.3) \end{aligned}$$

Here for the convenience of notation:

$$\begin{aligned} s &\equiv \sin \hat{\omega} \hat{t} & s_- &\equiv \sin(1-\hat{\omega})\hat{\tau}_L & s_+ &\equiv \sin(1+\hat{\omega})\hat{\tau}_L \\ c &\equiv \cos \hat{\omega} \hat{t} & c_- &\equiv \cos(1-\hat{\omega})\hat{\tau}_L & c_+ &\equiv \cos(1+\hat{\omega})\hat{\tau}_L \end{aligned} \quad (5.4)$$

Also, in order to simplify the algebra, we have assumed $\hat{\alpha} = 1$. As far as the effect of the load is concerned, (3.19)-(3.27) are not affected by the introduction of harmonic oscillations and therefore they can be used in the form shown in Section 3. It is to be noted that in view of (5.1) we now have only a single unknown function, viz. $\hat{\tau}_L = \hat{\tau}_L(\hat{t})$, which for self-consistent solutions must be *the same* in (5.2) and (5.3). It is usual to assume that the separation of the electrodes \hat{x}_L and the load \hat{Z}_L are given so that \hat{E}_{01} and $\hat{\omega}$ must be suitably chosen to assure the same $\hat{\tau}_L$ in both (5.2) and (5.3). In practice this is achieved with some help from the more general numerical computations, the exercise acting as an additional check, bearing in mind the algebraic complexity of the general case (see Appendix 3). However, in the case of harmonic oscillations we are able to derive in detail expressions for the AC and DC components of the total current. Dropping the subscript L in (5.2) we now obtain

$$\hat{v} = \hat{x}^* = \partial_{\hat{t}} \hat{x} + \partial_{\hat{i}} \hat{x} = 1 + \hat{E}_{01} \left[c \left(\frac{s_-}{2(1-\hat{\omega})} + \frac{s_+}{2(1+\hat{\omega})} \right) + s \left(\frac{c_- - \hat{\omega}}{2(1-\hat{\omega})} + \frac{-c_+ - \hat{\omega}}{2(1+\hat{\omega})} \right) \right] \quad (5.5)$$

$$\hat{E} = \hat{v}^* = \partial_{\hat{t}} \hat{v} + \partial_{\hat{i}} \hat{v} = \hat{E}_{01} \left[c \left(\frac{c_- - \hat{\omega}^2}{2(1-\hat{\omega})} + \frac{c_+ - \hat{\omega}^2}{2(1+\hat{\omega})} \right) - s \left(\frac{s_-}{2(1-\hat{\omega})} - \frac{s_+}{2(1+\hat{\omega})} \right) \right] \quad (5.6)$$

Thus in the interelectrode space we have the following expressions for the reduced convection current:

$$\hat{J}_c = \hat{p}\hat{v} = (\partial_{\hat{x}} \hat{E} + 1)\hat{v} = \hat{v}\partial_{\hat{x}} \hat{E} + \hat{v} = d_{\hat{i}} \hat{E} - \partial_{\hat{i}} \hat{E} + \hat{v} \quad (5.7)$$

where we have substituted from (3.1) for $\hat{\alpha} = 1$ and used (3.4). We now note from (5.5) and (5.6) that

$$\partial_{\hat{i}} \hat{E} + \partial_{\hat{i}} \hat{x} = -\hat{E}_{01} s = d_{\hat{i}} \hat{E}_0 = \hat{E}_0^* \quad (5.8)$$

$$\partial_{\hat{t}} \hat{E} + \partial_{\hat{t}} \hat{x} = 1 \quad (5.9)$$

Using (5.9) and bearing in mind that in general $d_{\hat{i}} = \partial_{\hat{t}} + \partial_{\hat{i}} \hat{x}$ we now obtain from (5.7)

$$\begin{aligned} \hat{J}_c &= \partial_{\hat{t}} \hat{E} + \partial_{\hat{t}} \hat{x} + \partial_{\hat{i}} \hat{x} = 1 + \partial_{\hat{i}} \hat{x} \\ &= 1 - \hat{\omega} \hat{E}_{01} \left[s \left(\frac{1 - c_-}{2(1 - \hat{\omega})} + \frac{1 - c_+}{2(1 + \hat{\omega})} \right) - c \left(\frac{s_-}{2(1 - \hat{\omega})} - \frac{s_+}{2(1 + \hat{\omega})} \right) \right] \end{aligned} \quad (5.10)$$

We can now recognise in (5.10) the d.c. component of the convection current $\hat{J}_c = 1$ and the a.c. component $\hat{J}_c^* = \partial_{\hat{i}} \hat{x}$; since the a.c. component of the convection current at the entrance electrode is zero by definition (see (5.10)) we now have $\hat{J}_c = 1 = \hat{J}_{co} = \hat{J}_{tot,0} = \hat{J}_{tot}$. The displacement current as usual, is obtained by writing from (5.6);

$$\hat{J}_d = \hat{J}_d = \partial_{\hat{i}} \hat{E} = -\hat{\omega} \hat{E}_{01} \left[s \left(\frac{c_- - \hat{\omega}^2}{2(1 - \hat{\omega})} + \frac{c_+ - \hat{\omega}^2}{2(1 + \hat{\omega})} \right) - c \left(\frac{s_-}{2(1 - \hat{\omega})} - \frac{s_+}{2(1 + \hat{\omega})} \right) \right] \quad (5.11)$$

It is to be noted that at the entrance electrode $\hat{J}_d = -\hat{\omega} \hat{E}_{01} s = d_{\hat{i}} \hat{E}_0 = \hat{E}_0^* \neq 0$ as would be expected due to the fact that the field at the entrance electrode \hat{E}_0 varies with time (see (5.1)). Finally we know that in a 1-D system the total current \hat{J}_{tot} remains constant with

\hat{x} (or \hat{t}) and only varies with \hat{t} . This is confirmed by adding (5.10) and (5.11) when we obtain

$$\hat{J}_{\text{tot}} = \hat{J}_c + \hat{J}_d = 1 - \hat{\omega} \hat{E}_{01} s = 1 + d_i \hat{E}_0 = \hat{J}_{c0} + \hat{J}_{d0} = \hat{J}_{\text{tot},0} \quad (5.12)$$

(see also (3.3), (3.5) and (3.6)).

So far we have considered the reduced currents in the interelectrode space only, viz. \hat{J}_c and \hat{J}_d , the currents individually depending on both \hat{x} and \hat{t} . However in the presence of a load we must relate \hat{x} dependent, i.e. 1-D currents to 'circuit' currents which are 0-D by definition. We do that by averaging \hat{J}_c and \hat{J}_d with respect to \hat{x} ; bearing in mind the continuity of the total current \hat{J}_{tot} , we obtain:

$$\begin{aligned} \langle \hat{J}_{\text{tot}} \rangle &= \frac{1}{\hat{x}_L} \int_0^{\hat{x}_L} \hat{J}_{\text{tot}} d\hat{x} = \hat{J}_{\text{tot}} = \frac{1}{\hat{x}_L} \int_0^{\hat{x}_L} \hat{J}_c d\hat{x} + \frac{1}{\hat{x}_L} \int_0^{\hat{x}_L} \hat{J}_d d\hat{x} \\ &= \langle \hat{J}_c \rangle + \frac{1}{\hat{x}_L} \partial_i \int_0^{\hat{x}_L} \hat{E} d\hat{x} = \langle \hat{J}_c \rangle + \frac{1}{\hat{x}_L} \partial_i \int_0^{\hat{x}_L} \partial_{\hat{x}} \hat{\phi} d\hat{x} = \langle \hat{J}_c \rangle + \frac{1}{\hat{x}_L} \partial_i (\hat{\phi}_L - \frac{1}{2}) \\ &= \langle \hat{J}_c \rangle + \frac{1}{\hat{x}_L} \partial_i \hat{\phi}_L = \hat{J}_{\text{ind}} + \hat{J}_{\text{cap}} = \hat{J}_{\text{tot},0} \end{aligned} \quad (5.13)$$

(note the positive sign in (3.15) and (A1.1)). Thus as is well known, the sum of the two 'circuit' currents, i.e. the sum of the induced current \hat{J}_{ind} and the capacity charging current \hat{J}_{cap} , is still equal to $\hat{J}_{\text{tot}} = \hat{J}_{\text{tot},0}$, although in the presence of space charge we have in general $\hat{J}_c \neq \hat{J}_{\text{ind}}$ and $\hat{J}_d \neq \hat{J}_{\text{cap}}$. We find from other consideration that the definition of \hat{J}_{ind} as a space average of the convection current $\langle \hat{J}_c \rangle$ is quite usual in 1-D system [35]. If \hat{J}_c is expressed in terms of (\hat{t}_L, \hat{t}) rather than (\hat{x}_L, \hat{t}) , as it is in our case (5.10), then the averaging procedure may be algebraically involved, although we can always write

$$\langle \hat{J}_{\text{tot}} \rangle = \langle \hat{J}_c \rangle + \langle \hat{J}_d \rangle = \hat{J}_{\text{ind}} + \hat{J}_{\text{cap}} = \hat{J}_{\text{tot},0} = 1 + \hat{E}_0^* = \hat{J}_{\text{ind}} + (\hat{J}_{\text{ind}} + \hat{J}_{\text{cap}}) \quad (5.14)$$

In a short-circuited diode we have $\hat{\phi}_L = 0$ so that by definition $\hat{J}_{\text{cap}} = \hat{J}_{\text{cap}} = 0$ and we simply have

$$\langle \hat{J}_{\text{tot}} \rangle = 1 + \hat{E}_0^* = \hat{J}_{\text{ind}} + \hat{J}_{\text{c0}} = \hat{J}_{\text{tot},0} = \hat{J}_{\text{c0}} + \hat{J}_{\text{d0}} \quad (5.15)$$

so that in this special case the induced current

$$\hat{J}_{\text{ind}} = \hat{J}_{\text{d0}} = \hat{E}_0^* = -\hat{\omega} \hat{E}_{01} s \quad (5.16)$$

In the more general case of $\hat{\phi}_\ell \neq 0$ we find from (5.14) that there are two contributions to \hat{E}_0^* , one which is due to space-charge effects and the other due to the potential difference between the electrodes $\hat{\phi}_\ell$. Thus although (5.14) is always valid, the values of \hat{E}_0^* will differ, depending on whether $\langle \hat{j}_a \rangle = 0$ (or $\hat{\phi}_\ell = 0$), as is the case in a short circuited diode, or whether $\langle \hat{J}_d \rangle \neq 0$ (or $\hat{\phi}_\ell \neq 0$) in the presence of a load.

The current inter-relationships indicated in (5.7)-(5.16) are quite general and independent of the actual form of $\hat{E}_0(\hat{t})$ which in this section was assumed to be harmonic, (5.1). In order to clarify matters even further we show the general current distribution in the two systems of Figs. 1 and 2 respectively in Figs. 7 and 8. The main difference between the two systems is that in Figs. 1 and 7 both DC and AC components of the total current \hat{J}_{tot} flow through the load \hat{Z}_ℓ , whereas in Figs. 2 and 8 only the AC component of the total current \hat{J}_{tot} is allowed to interact with the load. Since in general

$|\hat{J}_{\text{tot}}| \ll |\hat{J}_{\text{tot}}| = 1$, in the presence of a load the above difference has a profound effect on the dynamic behaviour of the system. One should also add that since on the whole $|\hat{J}_{\text{ind}}| < |\hat{J}_c|$, \hat{J}_{ind} being a spatial average of \hat{J}_c , the two currents \hat{J}_c and \hat{J}_d tend to flow in opposite directions in order to preserve the continuity of \hat{J}_{tot} , this being the case especially in a short-circuited diode. Perhaps one ought to add that the boundary conditions at the grid of the two systems of Figs. 1 and 2 are somewhat idealized, although in principle the systems are physically realizable.

We are now in a better position to test our numerical computations and compare them with the analytical results expressed by (5.2) and (5.3). In order to do that we have to choose a sensible value of the separation of the electrodes, say

$$\hat{x}_L = 2.875\pi = 9.0321 \quad (5.17)$$

and then obtain the corresponding values for $\hat{\omega}$ and \hat{E}_{01} by solving (3.14), (3.18) for $\hat{\alpha} = 1$. We then obtain

$$\hat{f} = 0.0278 \text{ or } \hat{\omega} = 2\pi\hat{f} = 0.1745 \quad (5.18)$$

$$\hat{E}_{01} = 0.112 \quad (5.19)$$

Having thus obtained the values of $\hat{\omega}$ & \hat{E}_{01} , we then substitute them in (5.2) and (5.3) with $\hat{\phi}_L = 0$ (short-circuited diode). The last step amounts to a somewhat laborious solution of the two equations in order to obtain *independently* the transit time as a function of time, $\hat{\tau}_L = \hat{\tau}_L(\hat{t})$. The two solutions are shown in Fig. 9 – they differ by less than 0.02%; bearing in mind the algebraic complexity of (3.14), (3.18) this is a very satisfactory agreement. It also indicates that in this case the oscillations are almost harmonic in nature, which of course was the initial assumption expressed by (5.1). What is of particular interest for our future investigations, especially those presented in Sections 7 & 8, is the fact that \hat{E}_{01} is quite small. Since from (5.14), (5.16) and (5.18) for a short-circuited diode

$$\hat{J}_{\text{ind}} = 1 \quad (5.20)$$

$$\left| \hat{J}_{\text{ind}} \right| = \left| \hat{E}_0^* \right| = \hat{\omega} \hat{E}_{01} = 0.0195 \quad (5.21)$$

in this case the electronic efficiency of generating this type of oscillations is very low, the AC component being only some 2% of the DC component of the total current $\hat{J}_{\text{tot}} = \hat{J}_{\text{ind}} + \hat{J}_{\text{ind}}$. However in some cases the efficiency may be as high as 30%, as can be seen in Figs. 18 and 19.

6. Method of presentation of computational results, using a short-circuited diode as an example.

In general the dynamical behaviour of the system is described by equations (3.14), (3.18) derived in Section 3 of the Report; here (3.14) is an integral equation, but in the presence of a load (3.18) becomes an integro-differential equation. Both equations are of the Volterra type and are characterized by the fact that the limits of integration are not fixed, but include a running variable, in our case \hat{t} . In the case of (3.14), (3.18) the situation is further complicated by the fact that the lower limit of integration in both cases contains not only the variable \hat{t} but also the transit time $\hat{\tau}_L(\hat{t})$, which is one of the *unknown* functions. It is not surprising therefore that no standard solutions or well established computer codes are available. It was therefore necessary to devise a special code of some complexity to deal with the problem at hand. The code for a short-circuited diode has been described in ref. 16 and a more generalized form of the code valid for the diode with a load is described in Appendix 2.

In the case of a short-circuited diode there is no practical difference between the two systems respectively shown in Figs. 1 and 2. The dynamic properties of the model can be described in several different ways. The simplest is to plot the so-called time history of the system, i.e. either \hat{E}_0 and/or $\hat{\tau}_L$ as functions of time. In Figs 10 a-d we have typical plots of $\hat{E}_0 = \hat{E}_0(\hat{t})$ for $\hat{\alpha}=1$ and different values of the parameter \hat{x}_L . Depending on the reduced separation of the electrodes \hat{x}_L we obtain, after a transient, either a steady value of \hat{E}_0 , Fig. 10a, or a time- varying value of \hat{E}_0 . For $\hat{x}_L = 2.88\pi$ the oscillations occur at a single frequency, Fig. 10b, but as \hat{x}_L decreases a bifurcation occurs, as can be seen in Fig. 10c computed for $\hat{x}_L = 2.86\pi$, the system having reached a chaotic state by the time $\hat{x}_L = 2.855\pi$, Fig. 10d. Figs. 11 a-d show the results of our computations when the separation of the electrodes \hat{x}_L is fixed and the parameter $\hat{\alpha}$ is varied. Here for the separation of the electrodes we have chosen the value of $\hat{x}_L = 2.88\pi$ used in Fig. 10b and leading to a

single frequency of oscillations when $\hat{\alpha} = 1$. We now find that for $\hat{\alpha} = 0.99$, Fig. 11a, a single frequency still prevails, although the mean value of \hat{E}_0 has become negative. However for $\hat{\alpha} = 0.988$ a bifurcation point has already been passed, Fig. 11b and for $\hat{\alpha} = 0.986$ there are strong indications of chaos, Fig. 11c, the dynamic behaviour of the system clearly being very sensitive to the value of $\hat{\alpha}$. This is further confirmed by Fig. 11d which was plotted for $\hat{\alpha} = 1.05$, the amplitude of oscillations now being five times that of Fig. 10b. Also it should be noted that for $\hat{\alpha} < 1$, when the net charge at the entrance electrode is slightly negative, the mean value of \hat{E}_0 is also negative, Figs. 11 a-c. However, when the net charge is positive, $\hat{\alpha} > 1$, the mean value of \hat{E}_0 is also positive, Fig. 11d.

Another method of presenting the dynamic properties of the system is based on the concept of the so-called phase trajectories. In our case this amounts to plotting \hat{E}_0 against $\hat{\tau}_L - \hat{x}_L$, Figs. 12 a-f. Let us first of all consider some simple phase-space trajectories. We find from (4.1) that in the absence of oscillations ($\hat{E}_0 = \text{const}$) and for $\hat{\alpha} = 1$, we have

$$\hat{x}_L = \hat{\tau}_L + \hat{E}_0[1 - \cos \hat{\tau}_L] \quad (6.1)$$

For $\hat{E}_0 = 0$ (Pierce diode) we have $x_L = v_0 \tau_L$ or in our notation $\hat{x}_L = \hat{\tau}_L$; thus in the absence of fields there is no acceleration and the initial velocity v_0 remains constant, the plot of \hat{E}_0 against $\hat{\tau}_L - \hat{x}_L$ being reduced to a single point at the origin. Since in the absence of fields between the electrodes $\hat{\tau}_L - \hat{x}_L = 0$, the variable $\hat{\tau}_L(\hat{t}) - \hat{x}_L$ can be looked at as an instantaneous measure of the departure of the diode from a field-free condition. For a steady state, Fig. 10a, where \hat{E}_0 after a transient becomes equal to a constant which is different from zero, the plot is still a single point, but it is now situated somewhere along a straight line passing through \hat{E}_0 and extending in the horizontal direction from $-2\hat{E}_0$ to $2\hat{E}_0$ (see (6.1)), its exact position being governed by the parameters of the system. For oscillatory and chaotic states, $\hat{E}_0 = \hat{E}_0(\hat{t})$, the single point

'opens up' and a more recognisable phase-space trajectory of our dynamical system finally emerges.

Let us now consider phase-space trajectories corresponding to time histories shown in Figs. 10 b - d. In the presence of a single frequency of oscillations the phase-space trajectory of the system is shown in Fig. 12a where, after a transient, a limit cycle develops. These results are in complete agreement with Fig. 10b which was computed for the same values of the parameters \hat{x}_L and $\hat{\alpha}$. The values of the parameters chosen for Fig. 12b are the same as those used in Fig. 10c -- in both cases we have a clear indication that a bifurcation has occurred, the system now exhibiting two frequencies of oscillations, the period of the corresponding trajectory now being doubled. In Fig. 12c, which corresponds to Fig. 10d, chaos appears to have set in; however, a further reduction in the separation of the electrodes leads to the appearance of three different frequencies and a tripling of the trajectory period at $\hat{x}_L = 2.855\pi$, as shown in Fig. 12d, the conditions of chaos again setting in for $\hat{x}_L = 2.8495\pi$, Fig. 12e. Finally for $\hat{x}_L = 2.8488\pi$ the phase trajectory just 'walks away', the system becoming unstable, Fig. 12f. Similar phase-space trajectories could be obtained for Figs. 11 a-d, but they are omitted in order to save space. In general time histories are particularly convenient when we wish to establish the amplitude and frequency of oscillations, but phase-space trajectories show bifurcations and the onset of chaos more clearly.

In order to condense a large amount of information, which is invariably available in numerical computations, it is very convenient to use the so-called bifurcation diagrams [37,38]. In our case this amounts to plotting $\hat{\tau}_L - \hat{x}_L$, or rather its maximum value, against \hat{x}_L for a fixed $\hat{\alpha}$, Figs. 13 - 15, or the same variable $\hat{\tau}_L - \hat{x}_L$ against $\hat{\alpha}$ for a fixed \hat{x}_L , Fig. 16. Since $\hat{\tau}_L$ now represents each consecutive maximum of $\hat{\tau}_L(t)$, when the system oscillates there will be one such value for a simply periodic motion, two for a doubly periodic motion, three for a triply periodic motion and so on; in chaos there will be a very large number of such maxima (see Figs. 10d, 11c, 12e and 13 - 16). The main advantage

of a bifurcation diagram is that it clearly indicates the values of parameters for which the system is singly periodic, multiply periodic or chaotic; in fact the construction of a bifurcation diagram is essential in order to establish a 'cascade of bifurcations', i.e. consecutive frequency doubling, which invariably precedes a truly chaotic behaviour of the system.

Let us now consider Fig. 13 in more detail. We find that for sufficiently large values of \hat{x}_L/π the system exhibits only a single frequency of oscillations, i.e. there is only one maximum value of $\hat{\tau}_L$ indicated by a dotted line which varies slightly in height (see also Figs. 10b and 12a). At $\hat{x}_L = 2.8633\pi$ a 'bifurcation' occurs, from now on the system being able to support two different frequencies of oscillations respectively indicated by two dotted lines (Figs. 10c and 12b). This situation persists until at $\hat{x}_L = 2.8585\pi$ when another bifurcation occurs, the system now being able to support four different frequencies. This process continues until we reach a state of chaos when $\hat{x}_L \approx 2.855\pi$ (also Figs 10d and 12c). As \hat{x}_L is reduced even further we encounter windows (white islands) when the system either reverts to a multiply periodic operation (Fig. 12d), or has bursts of chaotic behaviour (Fig. 12e). It is the cascade of bifurcations together with the presence of windows that are typical of a system which is capable of chaotic behaviour.

Having discussed Fig. 13 we are now in a better position to consider bifurcation diagrams which have been obtained for values of $\hat{\alpha} \neq 1$. In Figs. 14 and 15 are shown bifurcation diagrams which in some respects are similar to Fig. 13, but which have been computed respectively for $\hat{\alpha} = 0.995$ and $\hat{\alpha} = 1.05$. It can be seen that even such small changes in the value of $\hat{\alpha}$ have quite a profound effect both on the position of the first and subsequent bifurcations and on the shape and position of the windows and areas of chaos. In Fig. 16 we have therefore reversed the situation by keeping the separation of the electrodes constant at $\hat{x}_L = 2.88\pi$ and varied the initial charge ratio $\hat{\alpha}$ over a range of values. This leads to a new bifurcation diagram which is characterised by the fact that there appear to be two separate branches, indicating that certain maximum values of

$\hat{\tau}_L - \hat{x}_L$ are totally excluded, even in the chaotic state. Somewhat similar branches in Figs 13 - 15 appear to overlap.

The results of many such computations have been finally collected in Fig. 17 where the horizontal axis represents the separation of the electrodes \hat{x}_L and the vertical axis the initial charge ratio $\hat{\alpha}$. We now find that in the case of a short-circuited diode there are four distinct regimes of operation of the dynamic system shown in Figs. 1 and 2. For low values of \hat{x}_L and for the remaining values of \hat{x}_L when $\hat{\alpha} < 1$ the system is unstable, well in agreement with some earlier observations [14]. For higher values of \hat{x}_L and $\hat{\alpha} > 1$ after a short transient \hat{E}_0 and $\hat{\tau}_L$ reach constant values. Between these two regimes there is a range of \hat{x}_L and $\hat{\alpha}$ parameters for which the system is capable of sustaining stable oscillations - clearly this is the range of operation which would be of practical interest in the design of microwave devices. However this region is separated from the first (unstable) region by a band of chaos. In practice this particular range of \hat{x}_L and $\hat{\alpha}$ parameters must be avoided. It should be added that Figs. 13 - 16 can be combined together, the parameters \hat{x}_L , $\hat{\alpha}$ and $\hat{\tau}_L - \hat{x}_L$ forming a Cartesian 3-D space. Figs. 13 - 15 then represent plane cross-sections respectively occurring at $\hat{\alpha} = 1.0, 0.995$ and 1.05 , whereas Fig. 16 is a plane cross-section at a fixed value of $\hat{x}_L = 2.88\pi$. Finally Fig. 17 can be looked at as a projection of all such results on the $(\hat{x}_L, \hat{\alpha})$ -plane giving us an overall view of the dynamic behaviour of the system.

Let us now consider in more detail the oscillatory region which is clearly shown in Fig. 17. In order to explore the region more closely we have collected the results of computations obtained along two straight lines, one for variable $\hat{\alpha}$ and a fixed value of $\hat{x}_L/\pi = 2.88$, line A and the other for a variable \hat{x}_L/π and a fixed $\hat{\alpha} = 1.05$, line B, both shown in Fig. 17. The variations of amplitude and frequency are shown in Figs. 18 and 19. We find from Fig. 18 that for a fixed \hat{x}_L/π the amplitude of oscillations varies quite markedly with $\hat{\alpha}$, the highest value occurring near the upper edge of the oscillatory region, where the charge balance at the entrance electrode is slightly in favour of positive

ions. In fact over a narrow range of $\hat{\alpha}$ the amplitude tends to grow almost exponentially - probably due to the fact that our model is short circuited, rather than connected to a load, as would be the case in practice. For $\hat{\alpha} < 1$ the system rapidly becomes chaotic, as can be seen in Fig. 17; for $\hat{\alpha} > 1.13$ the system becomes stable and ceases to oscillate. We can see from Fig. 18 that the frequency of oscillations also varies with $\hat{\alpha}$ and reaches its maximum again near the edge of the region. The dependence of the amplitude of oscillations and their frequency on \hat{x}_L/π for a fixed value of $\hat{\alpha} = 1.05$ is shown in Fig. 19. We now find that the maximum amplitude of oscillations again occurs near the edge of the oscillatory region, just before the system become stable. For the values of \hat{x}_L/π below 2.7 the operation of the system becomes chaotic and for $\hat{x}_L/\pi > 3.15$ the oscillations disappear altogether and the system becomes stable. It is interesting to note that the frequency of oscillations now remains fairly constant. This should not surprise us, since one would expect the ratio of positive and negative charges to have a marked influence on the frequency; for $\hat{\alpha} = \text{constant}$ this ratio is fixed at the entrance electrode and then varies with \hat{x} probably in a manner which is fairly independent of \hat{x}_L .

Finally let us consider possible reasons for the development of oscillations near $\hat{x}_L \approx 3\pi$. It is well known that for $\alpha = 1$ the system is stable for $\hat{E}_0 = 0$, $0 < \hat{x}_L < \pi$; $\hat{E}_0 = \hat{x}_L - \pi$, $\hat{x}_L > \pi$ and also for $\hat{E}_0 = \hat{x}_L - 3\pi$, $3\pi < \hat{x}_L < 3\pi + 1$ (see Fig. 3 in [14]). In the first two ranges the corresponding potential function has a single maximum between the electrodes, but in the third range there is enough room for a maximum *and* a minimum, Fig. 20. It is this situation which allows the oscillations to develop by the process of continuous shift of the two charge bunches from right to left and back again. The formation of charged bunches and their oscillatory movements between the electrodes can be clearly observed when the electron stream is represented by sheets of charge, as explained elsewhere [28]. Using (5.20), (5.21) as a measure of efficiency in generating this type of oscillations, we find that the oscillatory current as a fraction of the DC current varies from a few percent to a maximum of some 30%.

7. Physical interpretation of the results

The dynamical behaviour of the system using the Lagrangian approach has been considered elsewhere [28]. In this report we are primarily concerned with the Eulerian approach, the summary of our investigations for a short-circuited diode being presented in Fig. 17. In principle there are four different dynamic regimes of the system: stable, oscillatory, chaotic and unstable; they are all shown in Fig. 17 where the value of the initial charge ratio at the entrance electrode $\hat{\alpha}$ is plotted vertically and the separation of the electrodes \hat{x}_L/π is plotted horizontally. Each point in Fig. 17 has been obtained by subjecting the model to a lengthy numerical analysis in order to establish which of the four regimes is the appropriate one.

Let us now consider the general conditions of the system along the horizontal line $\hat{\alpha}=1$ in Fig. 17. In the stable region the system, after a brief transient, settles down to fixed values of the transit time $\hat{\tau}_L$ and the corresponding electric field at the entrance electrode \hat{E}_0 . In the oscillatory and chaotic regions the system is best represented by a bifurcation diagram sometime called a Poincaré map. In our case we may plot for $\hat{\alpha}=1$ the maximum value of $\hat{\tau}_L - \hat{x}_L$ against \hat{x}_L/π , Fig. 13 (see also Fig. 10 in [14]). Here the following physical significance should be attached to the variable $\hat{\tau}_L - \hat{x}_L$. In the absence of electric fields in the inter-electrode space we have $\tau_L = x_L/v_0$, or $\hat{\tau}_L = \hat{x}_L$ in our notation (see 4.1 and A1.1 in Appendix 1). Thus the value of $\hat{\tau}_L - \hat{x}_L$ is a measure of departure from the field-free condition between the electrodes. In the stable region $\hat{\tau}_L - \hat{x}_L$ must assume a value which is fixed and different from zero if $\hat{E}_0 \neq 0$. In the oscillatory region the value of $\hat{\tau}_L - \hat{x}_L = \hat{\tau}_L(\hat{t}) - \hat{x}_L$ will vary in synchronism with the oscillations. In the chaotic region we only consider the amplitude (max. value) of $\hat{\tau}_L - \hat{x}_L$, and plot it against, say, \hat{x}_L/π . When the system oscillates, there will be one maximum value for a simply periodic motion, two for a doubly periodic motion and so on; in chaos there will be a very large number of such points. Figs. 13-15 show typical examples of chaotic behaviour of the system; starting with a single frequency of oscillations we have a series of bifurcations as the crucial parameter changes, until we reach the state of chaos. Further changes of \hat{x}_L/π lead to white windows when the system reverts to a multiple

frequency state - these are again followed by ranges of chaos. Finally the system enters an unstable region, where no convergent solutions of (3.14), (3.18) are possible; this seems to indicate that the system is now in a run-away situation, possibly due to the appearance of a virtual cathode, when the Eulerian approach breaks down.

Perhaps one ought to add that in principle two types of oscillations are possible in a plasma-filled diode. The first type is generated by successive appearance and disappearance of a virtual cathode in the interelectrode space - such oscillations form the basis of operation of a vircator tube and cannot be investigated by using mathematical techniques presented in this Report. The second type of oscillations is based on a flip-flop movement of space charge in the interelectrode space, the mathematical formulation of the problem being presented in Section 5 of the Report.

Let us now discuss the physics of the problem using some simple concepts as a guiding principle. In the Eulerian approach the dynamics of the system is described by three functions, $\hat{\phi}$ (or \hat{E}), \hat{v} and $\hat{\rho}_e$, all three being functions of two independent variables \hat{x} and \hat{t} . In summarising the results, e.g. as in Fig. 17, we would only consider the time history of the electric field at the entrance electrode \hat{E}_0 - this provides a clear indication of the dynamic state of the system and the way it varies with the control parameters \hat{x}_L or $\hat{\alpha}$ [14-16,36]. Now since we are concerned with the actual physics of the problem, we must use all the information provided by the hydrodynamic approach and follow both the evolution in time and space of the three function \hat{E} , \hat{v} and $\hat{\rho}_e$. The results are presented in the form of 3-D graphs which clearly reveal the physical properties of the system in different dynamical states.

Let us now consider the four possible states, i.e. stable, oscillatory, chaotic and unstable, as we move along the line $\hat{\alpha} = 1$ in Fig. 17. We start with the stable state of the system when $\hat{x}_L = 2.9778\pi$. The spatial distribution and temporal evolution of the (electron) space charge density $\hat{\rho}_e$ are plotted as a 3-D surface in Fig. 21. Similar surfaces can be drawn for $\hat{\phi}$ (or \hat{E}) and \hat{v} , but they are omitted for reasons of space. Since in this case $\hat{E}_0 = 0$ (see Fig. 3 in [14]) it is not surprising that, once the transient has died out, the surface is a horizontal plain situated at $\hat{\rho}_e = 1$. This suggests that ions and

electrons are uniformly distributed throughout the inter-electrode space, their volume density being the same, the system thus being in a stable state. As far as the phase trajectory is concerned, we must first choose a fixed point, say the middle of the inter-electrode space ($\hat{x} = 0.5$) in order to observe the evolution of the system with time. In the above case the phase trajectory collapses to a single point (1,1,0), where $\hat{\rho}_e$, \hat{v} and \hat{E} , are the state variables.

We now move to an oscillatory state for, say $\hat{x}_L = 2.8785\pi$. The electron charge density surface $\hat{\rho}_e$ is now fully developed consisting of peaks and hollows, Fig. 22a. The peaks indicate a surplus and the hollows a deficiency of electrons compared to the fixed ion density $\hat{\rho}_{io}$; they form identical arrays along the time axis, implying a single frequency of oscillation. Consequently, the corresponding phase trajectory follows a single limit cycle shown in Fig. 22b. Looking at the variation of space charge density with distance, we find a wave pattern which pulsates in time, the peaks and hollows continuously exchanging their position. One may well wonder at this point how the system retains its dynamical balance? To answer this point we look at the space charge density averaged over the inter-electrode distance, Fig. 22c. Here the solid line represents electron charge density averaged over the inter-electrode space $\langle \hat{\rho}_e \rangle$ as a function of time. We find that the average value of the curve is somewhat above the $\langle \hat{\rho}_e \rangle = 1$ line, i.e. that on average there is a surplus of electrons in the interelectrode space, although a constant exchange of electrons between the electron cloud and the electrodes takes place, as would be expected in the case of steady oscillations. Thus although the initial ratio of ions to electrons is set to be 1:1 at the entrance electrode, for some values of \hat{x}_L the system develops a slight imbalance which breaks the static equilibrium and leads to oscillations.

Decreasing the separation of the electrodes even further, we find that for $\hat{x}_L = 2.8648\pi$ the system moves beyond the first bifurcation point. This is well illustrated by a $\hat{\rho}_e$ surface possessing peaks of two different heights along the time axis,

Fig. 23a; the corresponding phase space trajectory shows a typical double limit 'cycle', Fig. 23b. Averaging as above, we now find that the corresponding curve shows double periodicity, Fig. 23c. It is to be noted that in this case the amplitude of peaks and the average charge imbalance have both increased, compared to Fig. 22c.

When \hat{x}_L is further reduced to 2.8549π the system enters the state of chaos. This again is clearly shown by the shape of space charge density surface $\hat{\rho}_e$, Fig. 24a which has an irregular collection of peaks and hollows of varying amplitude. The corresponding phase space trajectory is a typical strange attractor, Fig. 24b. The corresponding curve representing the average $\langle \hat{\rho}_e \rangle$ as a function of time, Fig. 24c, shows further increase in the amplitude of peaks and also in the charge imbalance.

Finally, the system enters an unstable state when \hat{x}_L passes 2.8488π . The surface of $\hat{\rho}_e$, the phase trajectory and the average $\langle \hat{\rho}_e \rangle$ are now respectively shown in Figs 25a-c. They clearly suggest that the surplus of electrons becomes excessive and it eventually breaks down the dynamical balance between ions and electrons, the system reaching a run-away situation, possibly via formation of one or more virtual cathodes.

The physical aspect of the dynamics of a plasma-filled diode is neatly summarized in Fig. 26 where we have simple scales supported at a height proportional to the average excess of electrons, the two ends going up and down as a given point in the interelectrode space acquires or loses electron charge (see Fig. 26). Although the model is hardly rigorous, it has the attraction of simplicity.

8. Computational results – AC currents and a load

In the presence of a load \hat{Z}_t we have to distinguish between the two systems respectively shown in Figs 1 and 2. For historical reasons we propose to consider in the first place the system shown in Fig. 2 where only the AC component of the total current \hat{J}_{tot} is allowed to interact with the load, the electron beam being generated to the left of G1 and collected to the right of G2.

Also, the concept of a load is so broad that one had to decide how to be more specific. It seemed reasonable therefore to limit our investigations to a load in the form of a simple circuit comprising resistance, inductance and capacitance in series. In the circumstances, it is prudent to start with a single element, say a resistance \hat{R} , and consider in more detail its effect on the dynamic behavior of the system.

8.1 Resistive load

In the case of a purely resistive load \hat{R} the potential difference between the exit and entrance electrodes due to the flow of an AC component of the total current is given by (see (3.6) and (3.26))

$$\hat{\phi}_t = -\hat{x}_L \hat{R} \hat{D}_i \hat{E}_0 \quad (8.1)$$

where $\hat{D}_i \hat{E}_0 = d_i \hat{E}_0 = \partial_i \hat{E}_0(\hat{t}, 0)$.

In order to get some idea of the dynamic behaviour of the diode in the presence of a load $\hat{Z}_t = \hat{R}$ we have chosen a single point in Fig. 17 ($\hat{\alpha} = 1, \hat{x}_L / \pi = 2.855$) and then plotted phase-space trajectories for different values of \hat{R} . We know from Fig. 17 that for $\hat{R} = 0$ (short-circuited diode) the system is chaotic. We then find from Figs. 27a and b that the system still remains chaotic for $\hat{R} = 10^{-4}$ and 10^{-3} , but it becomes doubly-periodic at $\hat{R} = 10^{-2}$, Fig. 27c, and finally ceases to oscillate altogether at $\hat{R} = 10^{-1}$, the phase trajectory approaching a focus at the origin in Fig. 27d; in this case the load losses must have become excessive for the oscillations to be sustained.

As the next step of computations we have decided to repeat the whole of Fig. 17 but for a load $\hat{R} = 0.01$. The results of our computations are shown in Table 1 and Fig. 28; a composite 3D presentation in color is given in Fig. 29. Comparing the two sets of results shown in Figs. 17 and 28, 29 we find that the four important dynamic regions, viz. stable, oscillatory, chaotic and unstable are shifted somewhat. In particular, Fig. 28 and Table 1 clearly indicate that on the whole the chaotic region has broadened somewhat and moved to the left, whereas the oscillatory region has expanded to the right. However in the immediate vicinity of $\hat{\alpha} = 1$ the chaotic region has narrowed under the influence of the load, as shown in Fig. 28'. The shift of the chaotic regime with $\hat{\alpha}$ is shown in the bifurcation diagrams, Figs. 30 a-c, which are respectively plotted for $\hat{\alpha} = 0.99, 1.0$ and 1.01 . These diagrams are quite revealing but the construction of each diagram consumes about 5h of computer time on a Sun Ultra Enterprise 3000. However without this information Figs. 28 and 29, which summarize the results, could not have been constructed. It is worth mentioning at this point that $\hat{R} = 0.01$ corresponds to a resistive load of $R \approx 0.1\Omega$ if we assume $A = 25\text{cm}^2$, $d = 1\text{cm}$ (hence $C_v = 2.2\text{pF}$), $\phi_0 \approx 50\text{kv}$ and $J_{c0} \approx 9.0 \text{ kA/cm}^2$.

8. 2 Capacitive load

Let us now consider the dynamic behavior of the system when a purely capacitive load is connected across the diode. We find from (3.26) that in this case the potential difference between the exit and entrance electrodes due to the AC component of the total current flowing through the load is given by

$$\hat{\phi}_t = -\hat{x}_L \frac{1}{\hat{C}} \hat{E}_0 \quad (8.2)$$

Algebraically (8.2) is rather convenient since it does not involve time derivatives on the LHS of (3.18).

We can now investigate the effect of a capacitive load using both phase and bifurcation diagrams. Choosing $\hat{x}_L = 2.85\pi$, which for $\hat{\alpha} = 1$ brings us into the middle of the chaotic regime, we find from Figs. 31 a – d that decreasing the value of \hat{C} gradually

suppresses chaos. Starting with $\hat{C} = 10^6$, Fig. 31a, which is virtually equivalent to a short circuit, we move via an almost triply-periodic state for $\hat{C} = 175$, Fig. 31b, a doubly periodic state for $\hat{C} = 55$, Fig. 31c to a virtually pure singly-periodic state for $\hat{C} = 20$, Fig. 31d. For even lower values of \hat{C} , say $\hat{C} = 5$, the oscillations cease altogether, the system entering a steady state, no AC current being induced in the system, the phase diagram now being reduced to a single point at the origin. Perhaps one ought to add that in the absence of electric fields between the electrodes we have from (3.1) $\hat{x}_L = \hat{\tau}_L$ for $\hat{\alpha} = 1$; this corresponds to the origin $\hat{\tau}_L - \hat{x}_L = 0$ in our phase diagram, so that Figs. 31a-d, where we plot \hat{E}_0 against $\hat{\tau}_L - \hat{x}_L$, indicate how the system shown in Fig. 2 departs from a steady state. For the diode dimensions mentioned above the tube capacitance $C_v \approx 2.2$ pF, so that from (3.27) the reduced capacitance \hat{C} expresses C in the units of C_v .

Another way of representing the dynamic behavior of the system is with the help of a bifurcation diagram where again we plot the maximum value of $\hat{\tau}_L - \hat{x}_L$, but this time against \hat{C} rather than \hat{x}_L , Figs. 32 a and b. This presentation is much more complete giving us an overall view of the dynamic behavior of the system, whereas previously, Figs. 31a-d, we only had a series of snapshots, each valid for a particular value of \hat{C} . We find from Figs. 32 a and b, which have been plotted for two overlapping ranges of \hat{C} , that in this case increasing \hat{C} leads, via the usual cascade of bifurcations, to a state of chaos, including typical clear windows when the system suddenly becomes multiply periodic.

Finally it is again of interest to consider the dynamic behaviour of the system as a function of $\hat{\alpha}$. For $\hat{R} = 0.0$ and $\hat{C} = 10^6$, which is virtually equivalent to a short circuit, we find from Fig. 33a that for $\hat{x}_L = 2.88\pi$ and $\hat{\alpha} = 0.9855$ the system is clearly in a quadruply-periodic state and it becomes chaotic at $\hat{\alpha} = 1$, Fig. 33b. For $\hat{\alpha} = 1.02$ the system settles down to a single-periodic state with a well defined and quite stable limit cycle, Fig. 33c. These results are in agreement with those obtained previously and shown in Fig. 17. When a capacitive load of $\hat{C} = 20$ is connected across the electrodes, the situation changes somewhat. For $\hat{\alpha} = 0.9855$, Fig. 34a, the system starts almost chaotic,

but for $\hat{\alpha} = 1$, Fig. 34b, and in particular $\hat{\alpha}=1.01$ and 1.02 , Figs. 34c and d, the system settles down to well defined single-period oscillations.

When the capacitive load is further reduced to $\hat{C}=10$, single period oscillations occur for all three values of $\hat{\alpha}$, although they start with a somewhat ill shaped limit cycle which becomes more regular as $\hat{\alpha}$ grows; at the same time the amplitude of oscillation also increases, as can be seen in Figs. 35a-c.

Finally Fig. 36 shows a bifurcation diagram constructed for a range of values of $\hat{\alpha}$ and a single value of capacitance, $\hat{C}=20$. Choosing a suitable value for \hat{x}_L we find that the system starts in an oscillatory state for $\hat{\alpha}=1$ and then progresses via a cascade of bifurcations to reach a state of chaos as $\hat{\alpha}$ is being gradually reduced; below $\hat{\alpha}=0.981$ the system becomes unstable. This behavior is quite similar to that indicated in Fig. 17 which is valid for a short-circuited diode.

We should add here that our results, comprising $\hat{\alpha} = n_{i0}/n_{e0} \neq 1$, are complementary to those of Lawson [22] who limited himself to $\hat{\alpha}=1$ and a capacitive load; both sets of results are in close agreement where they overlap, e.g. for $\hat{\alpha}=1$, $\hat{C}=20$ (extrapolated Figs. 16 in [22II] and our Fig. 31d). It is important to note, Figs. 32a and b, that in addition to \hat{C} , the charge balance at the entrance electrode $\hat{\alpha} = n_{i0}/n_{e0}$ has a strong influence on chaos.

8.3 Inductive load

As a third example of a simple load let us consider the dynamic behaviour of the system when a purely inductive load is connected across the diode. We find from (3.26) that in this case the potential difference between the exit and entrance electrodes due to the AC component of current flowing through the load is given by

$$\hat{\phi}_e = -\hat{x}_L \hat{L} \hat{D}_i^2 \hat{E}_0 \quad (8.3)$$

The above expression has now to be substituted in (3.18) converting it from an integral into an integro-differential equation.

The results of our investigations for $\hat{\alpha}=1$ and three different separations of the electrodes, $\hat{x}_L = 2.85\pi$, 2.8517π and 2.8525π are respectively shown in Figs. 37a-d, 38a-d and 39a-d. For $\hat{L}=0.0$ i.e. a short circuit, the results are in general in agreement with Fig. 17, except possibly for Fig. 38 a, where the system is bordering on chaos. As the value of the inductance \hat{L} is increased, the system goes through a doubly-periodic state, $\hat{L}=0.5$ and Figs. 37c, 38c and 39c until it reaches a singly periodic state for $\hat{L}=1.0$, Figs 37d, 38d and 39d. In order to get a clearer understanding of the dynamic behaviour of the system as a function of \hat{L} we have plotted three bifurcation diagrams respectively for three different values of \hat{x}_L , Figs. 40a-c. We now find from the diagrams that the system is extremely sensitive to the separation of the electrodes \hat{x}_L ; in general the diagrams are shifted to the left as \hat{x}_L increases, i.e. the first bifurcation occurs at a steadily decreasing value of \hat{x}_L . The sensitivity of the system to variation in \hat{x}_L is further confirmed by bifurcation diagrams shown in Figs. 41a and b where we have used the separation of the electrodes \hat{x}_L as an independent variable. We can see that a 1% change in \hat{x}_L can move the system from single-period oscillations to chaos, and vice versa. Thus the position of chaos can be controlled quite effectively by varying \hat{x}_L (see also Figs. 17, 28 & 29).

8.4 Inductance, resistance and capacitance in series

In the case of a load comprising inductance, resistance and capacitance connected in series, the number of possible variations is very large indeed. We will therefore attempt to provide only an overview of the situation by specifying in fairly general terms how the three modes of behaviour, i.e. chaotic, oscillatory and stable are affected by an $\hat{R}, \hat{L}, \hat{C}$ load. We have already noticed in Sections 3.1 - 3.3 that a purely resistive, capacitive or inductive load can control chaos and even induce the diode to move into an oscillatory regime. We will now extend our investigations by first analyzing the effect of a load where \hat{R}, \hat{C} or \hat{R}, \hat{L} are connected in pairs, the third component being absent or kept constant.

8.4.1 Variable \hat{R} and \hat{C}

The results of our investigations for a load consisting of a resistance \hat{R} and a capacitance \hat{C} connected in series are shown in Tables 2a-c. In order to reduce the number of parameters we have decided to fix the value of $\hat{\alpha}$ by putting $\hat{\alpha}=1$ and then chose three different values of the capacitance, $\hat{C}=11, 20, 1000$, at the same time shifting the value of \hat{x}_L so that for $\hat{R}=0$ the system would always start in a chaotic state. The behaviour of the system as the resistance \hat{R} is varied over a wide range of values is shown in Tables 2 a-c. When the capacitance \hat{C} is relatively small, Table 2a, chaotic behaviour ceases when \hat{R} reaches 0.028. Using the same values for the tube parameters ($A = 25\text{cm}^2$, $x_L = 1\text{cm}$, $\phi_0 \approx 50\text{kV}$) this corresponds to $R \approx 0.3\Omega$. For larger values of \hat{R} the system breaks out into oscillations, their amplitude decreasing with increasing \hat{R} , until the oscillations cease altogether, the system reaching a stable state for $\hat{R} > 0.12$. Figs. 42a-d show the corresponding phase-space trajectories for $\hat{\alpha}=1$, $\hat{C}=11$, $\hat{x}_L = 2.77\pi$ and $\hat{R} = 0.0001, 0.001, 0.01$ and 0.1 .

In Table 2b the capacitance has been virtually doubled to $\hat{C}=20$; at the same time \hat{x}_L has been slightly increased from 2.77π to 2.82π in order to start with chaos for $\hat{R}=0$. We now find that as \hat{R} increases, the system ceases to be chaotic and enters the oscillatory state for $\hat{R}=0.025$; it then ceases to oscillate altogether for $\hat{R} > 0.108$. A graphical representation of these results is shown in Fig. 43a-d. We find from Figs. 43 a-b that the system starts by being chaotic for $\hat{R} = 10^{-4}$ and 10^{-3} , almost doubly-periodic at $\hat{R} = 10^{-2}$ and finally singly-periodic at $\hat{R} = 10^{-1}$. When the resistive component is further increased to $\hat{R} = 1$, the phase trajectory approaches a focus at the origin, the oscillations ceasing altogether, presumably due to excessive load losses. It is interesting to note that again the chaotic behaviour of the system can be quenched by a judicious addition to the output load of resistance \hat{R} . Assuming $\hat{R} = 10^{-4} \approx 0$ our Fig. 43a agrees in principle with Fig. 16 of Lawson [22II] for $\hat{x}_L = 2.82\pi$ (his $\alpha/\pi = 2.82$).

So far the behaviour of the system was very similar for $\hat{C}=11$ and $\hat{C}=20$. This situation changes quite drastically when the value of the capacitance is increased to $\hat{C}=1000$, Table 2c which corresponds to $C \approx 2000\text{pF}$, assuming the same physical dimensions for the diode. Now the chaotic behaviour of the system ceases when the resistive component of the load reaches $\hat{R} = 0.01$ ($R = 0.1\Omega$), the oscillatory state lasting only till we reach $\hat{R} = 0.06$ ($R = 0.6\Omega$); beyond this point the system settles down to a stable state. Since for $\hat{C}=1000$ the effect of the capacitance on the system is very small, the above results are in agreement with those obtained in Section 8.1 and shown in Figs. 28 and 29. Not surprisingly the chaos quenching effect of \hat{R} increases as the effect of the capacitance \hat{C} diminishes.

8.4.2 Fixed \hat{R} , Variable \hat{L} and \hat{C}

Having considered the effect of a load consisting of a resistance and a capacitance in series, let us now investigate the effect of the third element, viz. an inductance. In order to avoid varying too many parameters at the same time, let us keep the resistance constant and equal to $\hat{R} = 0.01$ ($R \approx 0.1\Omega$) and just vary the capacitance \hat{C} and the inductance \hat{L} .

The results of our investigations are shown in Tables 3 a-c. Here we have chosen again three different values of the capacitance, viz. $\hat{C}=11.0$, 20.0 and 1000.0 and allowed \hat{L} to vary over a reasonable range of values. We find from Table 3a that for $\hat{R} = 0.01$, $\hat{C}=11.0$ and $\hat{L}=0$ the system is in a chaotic state, in agreement with the results obtained in section 3.3.1 and shown in Table 2a. The state of chaos persists until $\hat{L}=5.0$ (or $L=0.25\mu\text{H}$ using our chosen tube parameters) when a single limit cycle or what we call an 'oscillatory state' is reached. In the process the system goes in reverse through the usual bifurcation cascade, passing one quadruply, and two doubly-periodic limit cycles respectively at $\hat{L}=2.0$, 2.4 and 2.5. For values of $\hat{L}>5.0$ the amplitude of oscillations steadily decreases and so does the rate of convergence of our computational process. One gets the impression that the system is approaching an unstable state.

The results shown in Table 3b have been obtained for $\hat{C} = 20.0$. As the value of \hat{L} is allowed to vary from zero to ten, the system again remains chaotic until we reach $\hat{L} = 2.4$, when the first bifurcation occurs, the system now exhibiting a clear limit cycle between $\hat{L} = 2.4$ and 10.0. Beyond $\hat{L} = 10.0$ the oscillations begin to fade away and the convergence process becomes progressively less well defined; again one suspects the approach of an unstable state.

Finally in Table 3c we have the results for $\hat{C} = 1000.0$, at which value the influence of the capacitance is very small. We now find that for $\hat{R} = 0.01$ and $\hat{L} = 0$ the system exhibits a doubly-periodic limit cycle and reaches a single limit cycle at $\hat{L} = 10$ (or $L = 0.5\mu H$). Beyond this point further increase in \hat{L} leads to diminishing amplitude of oscillations and possible instability. In general inductance tends to act like resistance and appears to hinder chaotic behaviour.

8.4.3 A Purely Reactive \hat{L} and \hat{C} load

In order to clarify matters somewhat we have investigated a system with a purely reactive, \hat{L} & \hat{C} load. Here, for the sake of brevity, we have assumed the capacitance to be constant and equal to $\hat{C} = 20.0$ and varied the inductance between zero and 5.0, as shown in Table 4. We find that the results are similar to those presented in Table 3b, except that now the system reaches an oscillatory state a little earlier at $\hat{L} = 5.0$ rather than 10.0; also, without the steadyng effect of a resistive component of the load, it has a tendency to go unstable a bit earlier. In fact the results appear to be closer to those shown in Tables 3a, where removing the resistive component, $\hat{R} = 0.0$, appears to require a higher capacitive susceptance.

9. Computational results – AC+DC currents and a load

At this point of our investigations it seemed appropriate to consider a system where both DC and AC components of the total current \hat{J}_{tot} would be allowed to interact with the load \hat{Z}_t , as shown in Fig. 1. This means that, in our notation, instead of writing $\hat{J}_{\text{tot}} = \hat{\tilde{J}}_{\text{tot}} = \hat{D}_i \hat{E}_0$ we have $\hat{J}_{\text{tot}} = \hat{\tilde{J}}_{\text{tot}} + \hat{\tilde{J}}_{\text{tot}} = 1 + \hat{D}_i \hat{E}_0$. Substituting this in an expression for $\hat{\phi}_t$ we obtain (3.23) which is repeated here for our convenience

$$\hat{\phi}_t = -\hat{x}_L \hat{Z}_t \hat{J}_{\text{tot}} = -\hat{x}_L \left[\hat{R} + \left(\hat{L} \hat{D}_i^2 + \hat{R} \hat{D}_i \right) \right] \hat{E}_0 \quad (9.1)$$

It is to be noted that in view of the presence of the DC component of the total current \hat{J}_{tot} , the load can no longer contain a series capacitance \hat{C} and at most it can consist of a resistance \hat{R} and an inductance \hat{L} in series.

9.1 Resistive load

In the case of a purely resistive load the potential difference between the exit and entrance electrodes due to the flow of the total current \hat{J}_{tot} is obtained from (9.1) by putting $\hat{L} = 0$,

$$\hat{\phi}_t = -\hat{x}_L \hat{R} \left(1 + \hat{D}_i \right) \hat{E}_0 \quad (9.2)$$

It is of interest to compare (8.1) and (9.2). Although the difference merely amounts to the addition of an extra term $-\hat{x}_L \hat{R} \hat{E}_0$, in practice this, as we shall see, has a profound effect on the dynamic behaviours of the system. This happens largely due to the fact that in most cases $|\hat{\tilde{J}}_{\text{tot}}| \gg |\hat{\tilde{J}}_{\text{tot}}|$, thus in the case of oscillations, the conversion of the kinetic energy of the electrons into the AC component of the electromagnetic field is rather poor, varying between 3-30% (see also Figs. 18 and 19).

Let us now consider the results of some more detailed investigations. We start with $\hat{\alpha} = 1$, $\hat{x}_L = 2.837\pi$ and a range of values of \hat{R} , the corresponding phase-space trajectories being shown in Figs 44a-d. Comparing this with Figs 27a-d, where only the

AC component of the current was allowed to interact with the load, we find that in the presence of the DC component the values of \hat{R} and their range are much smaller. Although for $\hat{R} = 0.001$, the corresponding trajectories look somewhat similar (allowing for a small change in \hat{x}_L), Figs. 44a and 27b, the system becomes doubly-periodic already for $\hat{R} = 0.0018$, Fig. 44c as opposed to $\hat{R} = 0.01$ in Fig. 27c and singly periodic for $\hat{R} = 0.0025$, Fig. 44d; for values of $\hat{R} > 0.0025$ the system ceases to oscillate altogether, whereas in the absence of the DC component of the current this does not happen until $\hat{R} \approx 0.1$. This extreme sensitivity to the value of \hat{R} in the presence of the DC component of current must be due to the fact that, as usual, for a given load, the system losses are proportional to \hat{J}_{tot}^2 which now includes $\hat{\tilde{J}}_{tot}$. The fact that in many cases $|\hat{\tilde{J}}_{tot}| \gg |\hat{J}_{tot}|$ has also been confirmed independently (see Section 5 of this Report).

The corresponding bifurcation diagram for the range $\hat{R} = (0.8 - 2.0) \times 10^{-3}$ is shown in Fig. 46a and gives more information about the dynamic behaviour of the system as a function of \hat{R} .

In order to investigate the system more closely we now repeat our computations for a slightly larger separation of the electrodes, $\hat{x}_L = 2.84\pi$. The corresponding phase-space trajectories, Figs. 45a-d are quite similar to those shown in Figs. 44a-d, except that now the system reaches doubly and singly-periodic states even earlier i.e. respectively for $\hat{R} = 0.0015$ and $\hat{R} = 0.002$. This appears to be consistent with (9.1), where $\hat{\phi}_t$ is shown to be proportional to $-\hat{x}_L \hat{R}$. The corresponding bifurcation diagram is shown in Fig. 46b where comparable bifurcation points are respectively shifted to lower values of \hat{R} compared to Fig. 46a. Finally in Fig. 49b we have a bifurcation diagram against the separation of the electrodes \hat{x}_L rather than the load \hat{R} . This presentation will be useful when we choose to compare results obtained for values of $\hat{\alpha} \neq 1$.

Bearing in mind the strong control that the initial ion/electron charge ratio $\hat{\alpha}$ exerts over the chaotic behaviour of the system we have carried out further computations respectively for $\hat{\alpha} = 0.99$ and 1.01 . In order to make it easier to compare the results, we

have now decided to choose the separation of the electrodes \hat{x}_L as a variable parameter, as we have already done in Figs. 30a-c, at the same time setting the load at $\hat{R} = 0.001$. We now find from Figs. 47 a-d that as we reduce \hat{x}_L the system gradually moves from a singly-periodic state, Fig. 47a through a doubly-periodic state, Fig. 48b to chaos, Fig. 47c and d. These results are further confirmed by a bifurcation diagram shown in Fig. 49a. Similar computations for $\hat{\alpha} = 1.01$ and $\hat{R} = 0.001$ again show a transition from a singly-periodic state, Fig. 48a, through a doubly-periodic state, Fig. 48b to chaos, Fig. 48d; here Fig. 48c seems to indicate a borderline between a doubly-periodic state and chaos; the above results are in agreement with the corresponding bifurcation diagram, Fig. 49c. It should be noted that in general an increase in $\hat{\alpha}$ tends to shift bodily the whole bifurcation diagram and hence the chaotic region to lower values of \hat{x}_L , without substantially changing the pattern. Also comparing Figs. 49a-c with Fig. 30a-c we find that a somewhat similar effect can be observed when the DC component of current is not allowed to interact with the load. In all cases, however, the state of chaos is approached from the right, i.e. bifurcations leading to chaos develop as the separation of the electrodes \hat{x}_L is being gradually reduced (see also Figs. 17, 28 and 29).

9.2 Resistance and inductance in series

In the presence of a DC component of the total current a series capacitance is not permitted since it would act as an open circuit; at most we can then have a resistance and an inductance in series. We have considered a similar load before in Section 8.4.2, but since the DC component of the total current is usually much greater than the corresponding AC component, we would now expect a substantially different dynamic behaviour of the system.

The expression for $\hat{\phi}_t$ which now has to be substituted on the LHS of (3.18) is given by (9.1). We start our investigations cautiously with a very small value of a series resistance, $\hat{R} = 0.0001$, the corresponding phase-space trajectories for four different values of \hat{L} being shown in Figs. 50a – d. As was to be hoped Figs. 50a-d a very similar

to Figs. 37a-d which have been computed for $\hat{R} = 0$. This is an encouraging test of the reliability of our computations. We have then repeated our computations for another value of \hat{x}_L , this time $\hat{x}_L = 2.8525\pi$, Figs. 51 a-d and again have found close similarity to the corresponding trajectories shown in Figs. 39 a - d. We then increased tenfold the value of the resistive component of the load by putting $\hat{R} = 0.001$ and altered \hat{x}_L slightly in order to start with chaos, Figs. 52 a - d. We now find that chaos persists a bit longer, $\hat{L} = 0.1$ and Fig. 52b, the doubly-periodic trajectories being somewhat 'cleaner', $\hat{L} = 0.5$ and Fig. 52c. In order to get a better overview corresponding bifurcation diagrams are shown in Figs. 53a-c. The first two diagrams are somewhat similar, but the third one, Fig. 53c, shows a clear shift to the right, in agreement with our earlier comments. As a cross-reference bifurcation diagrams against \hat{x}_L and for $\hat{R} = 0.001$ and two values of inductance, $\hat{L} = 0.1$ and 0.5 are respectively shown in Figs 54a and b; they should be compared with similar diagrams plotted for $\hat{R} = 0$ and shown respectively in Figs. 41a and b. The two sets of diagrams are similar in character, but the addition of a resistive component to the load shifted the pattern bodily to the left, i.e. chaos now starting at slightly lower values of \hat{x}_L . Finally a bifurcation diagram of the system for fixed \hat{x}_L , \hat{L} and variable \hat{R} is shown in Fig. 55, which agrees with Fig. 53b plotted for the same values of the parameters.

So far we have assumed in this Section that the important ion/electron charge density ratio at the entrance electrode $\hat{\alpha} = 1$. In order to complete our investigations we have carried out our computations for two values of $\hat{\alpha}$ different from unity, viz. $\hat{\alpha} = 0.99$ and 1.01. Here we have primarily considered the dependence of the dynamic behaviour of the system on the value of \hat{x}_L , keeping the other parameters constant. We start with $\hat{\alpha} = 0.99$ i.e. with slight preponderance of electrons at the entrance electrode; as can be seen from Figs. 17, 28 and 29 this is always a less stable region. We now find from Figs. 56a - d and 57a - d that a tenfold increase in the resistive component of the load tends to stabilize matters somewhat. This is accompanied by a shift to the left of the corresponding bifurcations diagram, as shown in Figs. 58a and b. Similar computations have been carried out for $\hat{\alpha} = 1.01$, the corresponding phase-space trajectories being

shown in Figs. 59a-d and 60a-d. As is often the case the system appears to be more stable for $\hat{\alpha} > 1$ i.e. when there is a preponderance of positive ions at the entrance electrode. However this may be a spurious effect since we have assumed throughout that the positive ions are immobile, whereas the electrons are not. The corresponding set of bifurcation diagrams for $\hat{\alpha} = 1.01$ is shown in Figs. 61a and b, where the usual shift to the left with increasing \hat{R} is clearly noticeable.

Finally bifurcation diagrams for two different values of \hat{x}_L and $\hat{\alpha}$ as an independent variable are shown respectively in Figs. 62a and b; they conveniently summarise the strong dependence of the dynamic behaviour of the system on the two important parameters \hat{x}_L and $\hat{\alpha}$, and at the same time act as additional check on the consistency of our computations. This is of some importance in view of the complexity of the two governing equations (3.14) and (3.18)

10. Conclusions and suggestions for future work

In general there are two different approaches to the problem of controlling chaos. Some authors are primarily concerned with altering the actual phase-space behavior of the system by subtle perturbations [40-43] or by a form of negative feedback [44-45]. Other authors are more concerned with the generation or suppression of chaos using various techniques, frequently by altering the external parameters of the system [45-47]. When we use the term 'control' we have in mind the latter approach to the problem.

In the past most of the work on a plasma-filled diode, including our own [14-16,24] was concentrated on the physics of the space between the entrance and exit electrodes, the process of beam generation and its injection being left severely alone. In real life such a simplified system is physically unrealisable – clearly some kind of emission surface has to precede the entrance electrode (i.e. grid) of a plasma filled diode. Elsewhere [25] we have already expressed our reservations of the habit of ignoring the beam generating element, when analysing the behaviour of the diode. We were then guided by the thought that in electronics it is frequently unsafe to analyse or model systems which are physically unrealisable. Having considered the matter further, we have come to the conclusion that if we wish to include in our model the appearance of a virtual cathode and the possibility of double-stream flow in a plasma-filled diode, then for reasons of consistency we must include in our analysis the cathode/grid region. This is of particular importance if we choose to treat the diode as a model for the interaction space of a virtual cathode oscillator (vircator) since, as we know, the strongest oscillations in such a tube are generated precisely by the process of virtual-cathode formation and annihilation. It is then essential to know what happens to the beam when it goes back into the cathode/grid

region, assuming, as usual, that the grid is ideally permeable, its sole purpose being the establishment of a fixed potential at the entrance to the plasma-filled diode. We would like to suggest that the usual approach is then inadequate since what is required is a Lagrangian rather than an Eulerian formulation of the problem where the analysis would be extended to the complete system comprising both the beam generating Region I and the beam/plasma interaction Region II; in the case of Fig. 2 the collector, Region III, should then also be included.

Conclusions

Having restated the framework of our investigations let us now consider the main conclusions.

1. It has been shown, that the hydrodynamic model of a short-circuited diode initially developed by B. B. Godfrey and based on a coupled pair of integral equations [14] can be generalized to include a load. This has been achieved by converting one of the integral equations into an intrgro-differential equation and then suitably developing the associated computer code (see [48] and Section 3 and Appendix 2 of this Report).
2. It has been established by solving the above equations that the system is able to support the following four distinct dynamic regimes of operation: stable, oscillatory, chaotic and unstable. This applies equally to a short-circuited diode and when a load is connected across the diode, as shown in Figs. 1 and 2 (see also Figs. 17, 28 and 29).

3. The transition from one dynamic regime to another, e.g. chaos control, is governed by the load and more directly by two important parameters of the system:

$\hat{\alpha} = n_{i0} / n_{e0}$ which is the ratio of ion to electron density at the entrance electrode and

\hat{x}_L which is the reduced separation of the electrodes, G and A in Fig. 1 and G1 and G2 in Fig. 2(see also Appendix 1). The strong influence that the two parameters $\hat{\alpha}$ and \hat{x}_L exert on the system is fully revealed by Figs. 17 and 28 and by numerous bifurcation diagrams, Figs. 13-16, 30, 32, 36, 41, 49, 54, 58, 61 and 62.

4. The effect of the load on the dynamic behaviour of the system is less marked but, as would be expected, in general the resistive component of the load tends to dampen both chaos and oscillations. In order to be more specific one can draw the following conclusions from detailed investigations:

Section 8 - AC current only.

8.1 Resistive load – increasing \hat{R} in general suppresses chaos and moves the system towards an oscillatory regime; eventually even the oscillations are quenched and the system reaches a stable state.

8.2 Capacitive load – the influence is more subtle but again in general a *reduction* in \hat{C} tends to suppress chaos and if anything encourages oscillations.

8.3 Inductive load – the effect is similar to that of \hat{R} except that excessive values of \hat{L} tend to destabilise the system, possibly by a momentary appearance of a virtual cathode (note the $\hat{D}_{\pi}\hat{E}_0$ term in (8.3)).

8.4.1 Variable \hat{R} and \hat{C} in series – chaos quenching effect of \hat{R} increases as the effect of the capacitance \hat{C} diminishes, i.e. as \hat{C} increases.

8.4.2 Fixed \hat{R} , variable \hat{L} and \hat{C} – in general excessive values of \hat{L} again tend to push the system towards a dynamically unstable state; the joint influence of \hat{R} and \hat{C} is as indicated in 8.4.1.

8.4.3 Purely reactive \hat{L} and \hat{C} load ($\hat{R} = 0$) – starting from chaos an oscillatory state is reached more readily, but so does instability due to the presence of \hat{L} .

Section 9 – AC + DC currents.

9.1 Resistive load – due to the fact that now the DC component of \hat{J}_{tot} is also allowed to interact with the load, the effect of \hat{R} is at least ten times greater than in 8.1; this means that very small variations in \hat{R} affect the system quite strongly. The explanation lies in the fact that in most cases the DC component of \hat{J}_{tot} is much greater than the corresponding AC component, the transformation of the kinetic energy of the electron beam into the electromagnetic energy of the field being rather poor (see also Figs. 44a-d and 45a-d).

9.2 \hat{R} and \hat{L} in series – in this case the inductive component \hat{L} seems to help \hat{R} is moving the system from chaos into an oscillatory state, its

tendency to cause instability having disappeared (see also Figs. 50a-d, 51a-d, 52a-d and 53).

5. In most cases the generation of flip-flop oscillations is not very effective. Although this type of oscillation based on the lateral movement of the space-charge cloud is relatively 'clean', its efficiency is not high, ranging from 3-30% (see Section 5, in particular (5.20) (5.21) and Fig. 20).

Future work

The following suggestions for future work are based on the results of the investigations presented above.

1. According to current investigations, the electronic efficiency in generating the space-charge flip-flop oscillations is quite low. Since most high power microwave generators operate at electron beam velocities in excess of 500 kV, it is suggested that above investigations should be extended to relativistic kinematics in the hope of improving the efficiency. We have reasons to believe that Godfrey's formulation of the problem [14] and equations (3.14) (3.18) could be generalized to encompass relativistic kinematics.
2. In systems shown in Figs. 1 and 2 there exists another type of oscillation which is typical of vircators and which depends on the appearance and disappearance of a virtual cathode. Regrettably such interaction process goes well beyond a hydrodynamic model and requires a Lagrangian rather than Eulerian formulation of the problem. We would like to suggest that a code call MAGIC would be well suited to tackle the problem.

3. At present it is assumed that the ions form a stationary background of uniform density. Although this assumption is quite realistic when we consider the first few nanoseconds in the operation of the device, it is excessively simplistic in the long run. In fact it may affect our conclusions concerning the stability of the system when $\hat{\alpha} \neq 1$. It is therefore suggested that further investigations should be carried out by modelling the actual ionisation process which generates the cloud of positive ions in the interelectrode space and then subject them to the usual forces of the electromagnetic field. Such task could probably be accomplished using one of the more recent versions of the computer code called MAGIC.

Appendix 1: Notation

In order to reduce the number of independent parameters it is customary to use two different sets of variables.

The first set is a logical development of the reduced variables used by B.B.Godfrey [14].

$$\begin{aligned}\hat{x} &= (\omega_{pe} / v_0)x, \quad \hat{t} = \omega_{pe} t, \quad \hat{v} = v / v_0, \quad \hat{\phi} = \phi / 2\phi_0, \quad \hat{\rho}_e = \rho_e / \rho_{e0} > 0, \\ \hat{\rho} &= \hat{\rho}_e - \hat{\rho}_i = (\rho_e + \rho_{i0}) / \rho_{e0}, \quad \hat{E} = -\frac{e}{m_0 \omega_{pe} v_0} E = \partial_{\hat{x}} \hat{\phi} \quad (A1.1) \\ \hat{J}_c &= \hat{\rho}_e \hat{v} = J_c / J_{c0}, \quad \hat{J}_d = \partial_{\hat{t}} \hat{E} = J_d / J_{c0}, \quad \hat{J}_{tot} = \hat{J}_c + \hat{J}_d = J_{tot} / J_{c0}\end{aligned}$$

Here, as usual:

x	-	position of an electron
v	-	velocity of an electron
m_0	-	rest mass of an electron
ρ_e	-	electron charge density (negative)
ρ_i	-	ion charge density (positive)
$\rho = \rho_e + \rho_i$	-	total charge density
$J_c = \rho_e v$	-	convection current
$J_d = \epsilon_0 \partial_x E$	-	displacement current
$J_{tot} = J_c + J_d$	-	total current
$\omega_{pe} = -(e\rho_{e0} / m_0 \epsilon_0)^{1/2}$	-	electron plasma frequency at the entrance electrode

the subscript zero indicating the value of the corresponding variable at the entrance electrode. Similarly, the subscript L indicates the value of the corresponding variable at the exit electrode, e.g. the reduced separation of the electrodes is written as

$$\hat{x}_L = (\omega_{pe} / v_0)x_L \quad (A1.2)$$

\hat{x} and x being zero at the entrance electrode.

The use of reduced variables (A1.1-A1.2) eliminates as separate parameters the initial values of electron velocity v_0 and electron space charge density ρ_{e0} , or stating it differently, the values of the injection current density J_{e0} , and the electron plasma frequency ω_{pe} . Since now by definition $\hat{v}_0 = \hat{\rho}_{e0} = \hat{J}_{e0} = 1$, the only remaining parameters are \hat{x}_L , the reduced separation of the electrodes and the initial ratio of the ion/electron charge densities $\hat{\alpha} = n_{i0} / n_{e0}$, the charge density of the immobile positive ions being kept constant throughout, $n_i = n_{i0}$. An additional advantage of the reduced notation is that \hat{E} is defined as a positive rather than negative slope of $\hat{\phi}$, as shown in (A1.1); frequently this is more convenient in the discussion of field distribution inside a plasma-filled diode.

In addition to the above 'hat' variables, sometimes it is more convenient to use 'bar' variables which have been introduced in the late thirties at the Bell Laboratories, when suspected hysteresis effects in screen grid/anode space of a tetrode had to be considered [52]. The 'bar' variables can be defined by writing:

$$\begin{aligned}\bar{x} &= x/d, \quad \bar{t} = t/t_0, \quad \bar{v} = v/v_0, \quad \bar{\phi} = \phi/\phi_0, \quad \bar{\rho}_e = \frac{d^2}{\epsilon_0 \phi_0} \rho_e, \\ \bar{\rho} &= \bar{\rho}_e - \alpha \bar{\rho}_{e0} = \frac{d^2}{\epsilon_0 \phi_0} (\rho_e + \rho_{i0}), \quad \bar{E} = \frac{d}{\phi_0} E = -\partial_{\bar{x}} \bar{\phi} \quad (A1.3) \\ \bar{J}_c &= \bar{\rho}_e \bar{v} = \frac{d^2}{\epsilon_0 \phi_0 v_0} J_c, \quad \bar{J}_d = \partial_{\bar{t}} \bar{E} = \frac{d^2}{\epsilon_0 \phi_0 v_0} J_d, \quad \bar{J}_{tot} = \bar{J}_c + \bar{J}_d = \frac{d^2}{\epsilon_0 \phi_0 v_0} J_{tot}\end{aligned}$$

Here

$$\begin{aligned}d &\quad - \quad \text{separation of the electrodes} \\ t_0 = d/v_0 &\quad - \quad \text{electron transit time in the absence of fields}\end{aligned}$$

so that $\bar{x} = 1$ at the exit electrode; at the entrance electrode $\bar{x} = 0$ as before. The injection current density is now defined in terms of a reduced current 'iota':

$$\iota = (-J_c) / (-J_{spl}) \quad (A1.4)$$

where

$$-J_{spl} = \frac{4}{9} \epsilon_0 \sqrt{\frac{2t}{m_0}} \frac{\phi_0^{3/2}}{d^2} = \frac{4}{9} \epsilon_0 \frac{\phi_0 v_0}{d^2} \quad (A1.5)$$

is the current density in an equivalent space-charge limited diode [52].

A table of relations between 'hat' and 'bar' variables is included for the convenience of the reader.

$$\begin{aligned}
 \hat{x} &= \frac{\bar{x}}{3}\sqrt{2\bar{t}}, \quad \hat{x}_L = \frac{1}{3}\sqrt{2\bar{t}}, \quad \hat{t} = \frac{\bar{t}}{3}\sqrt{2\bar{t}}, \quad \hat{v} = \bar{v} \\
 \hat{\phi} &= \frac{1}{2}\bar{\phi}, \quad \hat{\rho}_e = \bar{\rho}_e / \bar{\rho}_{e0} > 0, \quad \hat{\rho} = (\bar{\rho}_e / \bar{\rho}_{e0}) - \alpha, \quad \hat{E} = -\bar{E}/\frac{2}{3}\sqrt{2\bar{t}} \quad (\text{A1.6}) \\
 \hat{J}_c &= \bar{J}_c / \bar{J}_{c0}, \quad \hat{J}_d = \bar{J}_d / \bar{J}_{c0}, \quad \hat{J}_{\text{tot}} = \bar{J}_{\text{tot}} / \bar{J}_{c0}
 \end{aligned}$$

Appendix 2: Numerical Solutions of the Integral Equations

We have already pointed out in Section 3 that the dynamic behaviour of our system is going to be expressed in terms of two coupled integral equations of the Volterra type, (3.14) and (3.18). The kernels of the two equations are respectively given by $\sin[\alpha^{1/2}(\hat{t} - \hat{t}')]$ and $(\hat{t} - \hat{t}') \sin[\alpha^{1/2}(\hat{t} - \hat{t}')]$, the first kernel being antisymmetric, $K(\hat{t}'|\hat{t}) = -K(\hat{t}|\hat{t}')$ and the second symmetric $K(\hat{t}'|\hat{t}) = K(\hat{t}|\hat{t}')$. The equations have several peculiarities which add to the difficulties in obtaining numerical solutions. First of all in place of the usual Volterra type limits of integrations (a, \hat{t}) , we have $(\hat{t} - \hat{\tau}_L, \hat{t})$, where $\hat{\tau}_L = \hat{\tau}_L(\hat{t})$ is one of the unknown functions. In addition the function $\hat{\tau}_L(\hat{t})$ also appears in a complicated and *nonlinear* manner outside the integral in both equations. The other unknown function $\hat{E}_0(\hat{t})$ appears under the integral sign in (3.14) and (3.18) and also on the LHS of (3.18). Thus the equations resemble somewhat the Volterra equation of the second kind. In general as long as the kernel is bounded, no eigenvalues are associated with the equations; equally there is no indication in our case that solutions would only exist for some particular values of the important parameters $\hat{\alpha}$ and \hat{x}_L . However, in the presence of a load, one of the equations become integro-differential, see (3.23) or (3.26), which further adds to the difficulties in obtaining a solution.

Not surprisingly there are no readily available standard methods of solution of (3.14), (3.18), either analytical or numerical [15,16] and therefore it proved necessary to develop our own computer codes. In this we had to assume that the function $\hat{x}(\hat{t})$ is both continuous and twice differentiable, as is required by the transition from (3.11) to (3.12). Also, following common practice, we have assumed that $\hat{E}_0(\hat{t})$ and $\hat{\tau}_L(\hat{t})$ are L^2 functions, i.e. they are Lebesgue square integrable. In our opinion both assumptions are quite reasonable in practice.

As is invariably the case with nonlinear systems of differential equations a great deal depends on the accuracy with which an initial solution can be guessed. In linear systems the initial accuracy of a trial solution merely affects the rate of convergence, but in nonlinear systems it may well affect our ability to obtain any solution at all. Fortunately in our case we can be guided by a steady-state solution which, for given \hat{x}_L and $\hat{\alpha}$, at

least provides an approximate relationship between \hat{E}_0 and $\hat{\tau}_L$. Thus, assuming $\hat{E}_0 = \text{const}$ in (3.11) we can now solve it without too much difficulty obtaining the required steady state relationship

$$\alpha^{3/2} \hat{x}_L = \alpha^{1/2} \hat{E}_0 \{1 - \cos(\alpha^{1/2} \hat{\tau}_L)\} - (1 - \alpha) \sin(\alpha^{1/2} \hat{\tau}_L) + \alpha^{1/2} \hat{\tau}_L \quad (\text{A2.1})$$

Let us now turn to Fig. A2.1 which indicates the general computational procedure we have to follow. First of all (3.14) and (3.18) must be discretized by using the first two terms of Taylor's series and writing

$$f(\hat{t}_{i+1}) = f(\hat{t}_i) + f'(\hat{t}_i) \delta \hat{t} \quad (\text{A2.2})$$

The above equation makes it possible to compute an approximate value for $f(\hat{t}_{i+1})$ once $f(\hat{t}_i)$ is known.

As the next step we now have to calculate the derivatives with respect to time of (3.14), (3.18). Starting with $\phi_t = 0$ and using some simple abbreviations we now obtain the following expressions for $\hat{E}_0(\hat{t})$, $\hat{\tau}_L(\hat{t})$ and their respective derivatives:

$$f_1(\hat{t}) = \hat{E}_0(\hat{t}) = \frac{1}{\hat{x}_L} \left[\frac{1}{2} \left\{ \hat{\alpha} \hat{x}_L^2 - \frac{1}{\hat{\alpha}} \hat{\tau}_L^2 \right\} + \frac{1 - \hat{\alpha}}{\hat{\alpha}^{3/2}} [\hat{\tau}_L \sin(\hat{\alpha}^{1/2} \hat{\tau}_L) - \frac{1}{\hat{\alpha}^{1/2}} \{1 - \cos(\hat{\alpha}^{1/2} \hat{\tau}_L)\}] - \frac{1}{\hat{\alpha}^{1/2}} F_1 \right] \quad (\text{A2.3})$$

$$f_1'(\hat{t}) = d_{\hat{t}} \hat{E}_0(\hat{t}) = \frac{1}{\hat{x}_L} \left[\hat{\tau}_L F_4 - \frac{1}{\hat{\alpha}^{1/2}} F_2 - F_3 \right] \quad (\text{A2.4})$$

$$f_2(\hat{t}) = \hat{\tau}_L(\hat{t}) = \hat{\alpha} \hat{x}_L + \frac{1 - \hat{\alpha}}{\hat{\alpha}^{1/2}} \sin(\hat{\alpha}^{1/2} \hat{\tau}_L) - \hat{\alpha}^{1/2} F_2 \quad (\text{A2.5})$$

$$f_2'(\hat{t}) = d_{\hat{t}} \hat{\tau}_L(\hat{t}) = \frac{\hat{\alpha}^{1/2} \hat{E}_0(\hat{t} - \hat{\tau}_L) \sin(\hat{\alpha}^{1/2} \hat{\tau}_L) - \hat{\alpha} F_4}{1 - (1 - \hat{\alpha}) \cos(\hat{\alpha}^{1/2} \hat{\tau}_L) + \hat{\alpha}^{1/2} \hat{E}_0(\hat{t} - \hat{\tau}_L) \sin(\hat{\alpha}^{1/2} \hat{\tau}_L)} \quad (\text{A2.6})$$

where

$$F_1(\hat{t}) = \int_{\hat{t} - \hat{\tau}_L}^{\hat{t}} \hat{E}_0(\hat{t}') (\hat{t} - \hat{t}') \sin\{\hat{\alpha}^{1/2} (\hat{t} - \hat{t}')\} d\hat{t}' \quad (\text{A2.7})$$

$$F_2(\hat{t}) = \int_{\hat{t} - \hat{\tau}_L}^{\hat{t}} \hat{E}_0(\hat{t}') \sin\{\hat{\alpha}^{1/2} (\hat{t} - \hat{t}')\} d\hat{t}' \quad (\text{A2.8})$$

$$F_3(\hat{t}) = \int_{\hat{t}-\hat{\tau}_L}^{\hat{t}} \hat{E}_0(\hat{t}')(\hat{t} - \hat{t}') \cos\{\hat{\alpha}^{1/2}(\hat{t} - \hat{t}')\} d\hat{t}' \quad (A2.9)$$

$$F_4(\hat{t}) = \int_{\hat{t}-\hat{\tau}_L}^{\hat{t}} \hat{E}_0(\hat{t}') \cos\{\hat{\alpha}^{1/2}(\hat{t} - \hat{t}')\} d\hat{t}' \quad (A2.10)$$

In practice it proved convenient to separate the \hat{t} and \hat{t}' variables by writing, e.g. $\sin\{\hat{\alpha}^{1/2}(\hat{t} - \hat{t}')\} = \sin(\hat{\alpha}^{1/2}\hat{t})\cos(\hat{\alpha}^{1/2}\hat{t}') - \cos(\hat{\alpha}^{1/2}\hat{t})\sin(\hat{\alpha}^{1/2}\hat{t}')$. In view of the algebraic complexity of (A2.3)-(A2.6) the usual Runge-Kutta or predictor-corrector methods of integration are not feasible. The four functions $f_1 \dots f_2'$ all contain integrals with a lower limit in the form $\hat{t} - \hat{\tau}_L(\hat{t})$, where $\hat{\tau}_L(\hat{t})$ is one of the unknown functions, as indicated in (A2.7) – (A2.10). This means that the values of $\hat{\tau}_L(\hat{t}_i)$ for the first n steps must be guessed until we reach $i = n + 1$, as shown in Fig. A2.1. Here the horizontal axis represents the time variable \hat{t} and the vertical axis the starting time of consecutive trial trajectories \hat{t}' , the straight line inclined at 45° simply tracing $\hat{t}' = \hat{t}$. Along this line are indicated the values of $\hat{E}_0(\hat{t})$ for different values of $\hat{t} = \hat{t}_i$, whereas in the downward vertical direction are plotted the corresponding values of the transit time $\hat{\tau}_L(\hat{t}_i)$. We now use (A2.1) to guide us in the right choice of $\hat{\tau}_L(\hat{t}_{n+1})$ and $\hat{E}_0(\hat{t}_{n+1})$. These values are then substituted in F_2 on the RHS of (A2.5); in order to be able to carry out the indicated integration, we have to assume some values for $\hat{E}_0(\hat{t}_1)$ to $\hat{E}_0(\hat{t}_n)$. Experience has shown that the quickest convergence can be obtained when we assume a random distribution of \hat{E}_0 for all values of \hat{t}_i from \hat{t}_1 to \hat{t}_n . It is now possible to carry out the computations indicated on the RHS of (A2.5), in order to obtain $\hat{\tau}_L(\hat{t}_{n+1})$ appearing on the LHS of the equation. The new value is then substituted back on the RHS of (A2.5), keeping the values $\hat{E}_0(\hat{t}_1) - \hat{E}_0(\hat{t}_n)$ *unchanged*. This process is repeated until the two values of $\hat{\tau}_L(\hat{t}_{n+1})$ converge. We then move to (A2.3), first substituting $\hat{E}_0(\hat{t}_1) - \hat{E}_0(\hat{t}_{n+1})$ on the RHS of the equation. Carrying out the integration indicated by F_1 , we are provided with a new value for $\hat{E}_0(\hat{t}_{n+1})$ which we then substitute back on the RHS of (A2.3). This process is again repeated until the two values of $\hat{E}_0(\hat{t}_{n+1})$ converge. Once the values of $\hat{\tau}_L(\hat{t}_{n+1})$

and $\hat{E}_0(\hat{t}_{n+1})$ have been obtained, we can proceed to the next step, which is the calculation of $\hat{\tau}_L(\hat{t}_{n+2})$ and $\hat{E}_0(\hat{t}_{n+2})$ using (A2.2) and (A2.3)-(A2.6), the corresponding limit of integration $\hat{t}_i - \hat{\tau}_L(\hat{t}_i)$ being shown as a broken line in Fig.A2.1. This process is then continued as long as necessary, i.e. until the solutions settle down.

In order to complete the description of our computing process we still have to agree on a suitable value for the time interval $\delta\hat{t}$. One might think that the first choice would be to write

$$\delta\hat{t} = \hat{\tau}_L(\hat{t}_i)/i \quad (A2.11)$$

However this would mean that $\delta\hat{t}$ would have to vary with $\hat{\tau}_L$, which is very inconvenient. We have decided therefore to adopt a different approach by choosing a reasonable value for $\delta\hat{t}$ and then keeping it constant throughout. This means of course that $\hat{\tau}_L$ could no longer be expressed as a multiple of $\delta\hat{t}$, but must now be written as

$$\begin{aligned} \hat{\tau}_L(\hat{t}_{n+1}) &= (n+1-j)\delta\hat{t} + \varepsilon \\ &= \hat{\alpha}\hat{x}_L + \frac{1+\hat{\alpha}}{\hat{\alpha}^{1/2}} \sin(\hat{\alpha}\hat{\tau}_L) - \hat{\alpha}^{1/2} \int_{\hat{t}_j}^{\hat{t}_{n+1}} \hat{E}_0(\hat{t}') \sin\{\hat{\alpha}^{1/2}(\hat{t}-\hat{t}')\} d\hat{t}' \end{aligned} \quad (A2.12)$$

The corresponding flow diagram for obtaining ε is shown in Fig. A2.2.

We now possess all the information required for setting up a computer code for the numerical solution of (3.14), (3.18) in the absence of a load. In general there are three different ways in which the functions \hat{E}_0 and $\hat{\tau}_L$ can settle down - they may reach a constant value (stable region), they may oscillate with a fixed frequency or frequencies (oscillatory region), or they may become chaotic (chaotic region). Finally, for some ranges of the parameters \hat{x}_L and $\hat{\alpha}$, no numerically stable solutions of (3.14), (3.18) can be obtained (unstable region). In a short-circuited diode we have used the above code extensively for a wide range of parameters \hat{x}_L and $\hat{\alpha}$, the results of our investigations being presented in Section 6 of the Report (see also [15], [16], [24], [36], [49-51]). Since our current investigations are primarily concerned with the effect of a load on the dynamics of our system, we now have to consider the relevant extension of our computational procedure.

In the presence of a load, one of the equations, viz. (3.18), becomes integro-differential. This is clearly shown in (3.22) and (3.26) where first and even second order derivatives of \hat{E}_0 with respect to time appear in corresponding expressions defining $\hat{\phi}_t$ in terms of \hat{R} and \hat{L} . These derivatives are associated with the displacement current which in the reduced notation is simply given by $\hat{J}_{d,0} = \partial_i \hat{E}(\hat{t}, 0) = d_i \hat{E}_0$, subscript zero indicating the conditions at the entrance electrode. Thus in the presence of a load we must discretize the LHS of (3.18) by expressing the derivatives in terms of the corresponding differences. In practice it is best to use backward differences and write, say

$$\begin{aligned} f_i' \delta \hat{t} &= \nabla_i + \frac{1}{2} \nabla_i^2 + \dots \\ &= \frac{1}{2} (3f_i - 4f_{i-1} + f_{i-2}) \end{aligned} \quad (A2.13)$$

$$\begin{aligned} f_i'' (\delta \hat{t})^2 &= \nabla_i^2 + \dots \\ &= f_i - 2f_{i-1} + f_{i-2} \end{aligned} \quad (A2.14)$$

higher order approximations being used when required. The addition of the difference expressions on the LHS of (A2.3) further complicates the code, Fig. A2.3, which is already quite involved even when the diode is just short-circuited; this in turn increases the CPU time, especially in the case of bifurcation diagrams.

Appendix 3 General observations on the effect of positive ions

In view of the complexity of responses of the system and its nonlinearity of behaviour it would seem advisable to consider in some detail the simplest case of a steady state (uniform flow) and the corresponding effect that the introduction of positive ions has on the system.

Let us start with the Poisson equation combined with the conservation of energy equation which in our notation can be written as

$$\frac{d^2\hat{\phi}}{d\hat{x}^2} = \hat{\rho} = \frac{1}{\sqrt{2\hat{\phi}}} \quad \text{electrons only} \quad (\text{A3.1a})$$

$$\frac{d^2\hat{\phi}}{d\hat{x}^2} = \hat{\rho} - \hat{\alpha} = \frac{1}{\sqrt{2\hat{\phi}}} - \hat{\alpha} \quad \text{electron + positive ions} \quad (\text{A3.1b})$$

The difference between the two equations is clearly shown in Figs A3.1 and A3.2. In the absence of ions we must have $d^2\hat{\phi}/d\hat{x}^2 > 0$ for all values of $\hat{\phi}$ so that the solution of (A3.1a), i.e. $\hat{\phi} = \hat{\phi}(\hat{x})$ must be concave upwards and therefore $\hat{E}_0 = (d\hat{\phi}/d\hat{x})_0 \leq 0$, subscript zero indicating conditions at the entrance electrode. In the presence of ions this is no longer the case, $d^2\hat{\phi}/d\hat{x}^2$ can now be positive, negative or even zero when $\hat{\phi} = \frac{1}{2}\hat{\alpha}^2$. This permits periodic solutions for an appropriate choice of boundary conditions, a type of solution which was not possible in the absence of positive ions.

Let us now consider the first integral of (A3.1a) and (A3.1b). Multiplying both by $2d\hat{\phi}/d\hat{x}$ and integrating we obtain:

$$\hat{E} = \frac{d\hat{\phi}}{d\hat{x}} = \pm \sqrt{2\sqrt{2\hat{\phi}} + c_0}, \quad c_0 = \hat{E}_0^2 - 2 = -2\sqrt{2\hat{\phi}_m} \quad (\text{A3.2a})$$

$$\hat{E} = \frac{d\hat{\phi}}{d\hat{x}} = \pm \sqrt{2\sqrt{2\hat{\phi}} - 2\hat{\alpha}\hat{\phi} + c}, \quad c = \hat{E}_0^2 - 2 + \hat{\alpha} \quad (\text{A3.2b})$$

Here $\hat{\phi}_m$ in (A3.2a) stands for the value of a single minimum potential between the electrodes. In (A3.2b) on the other hand we may have a minimum and a maximum, either given by

$$\hat{\phi}_m = \frac{1}{4\hat{\alpha}^2} \{1 \mp \sqrt{1 + \hat{\alpha}c}\} \quad (A3.3)$$

The above expressions are obtained by putting $\hat{E} = 0$ and $\hat{\phi} = \hat{\phi}_m$ in either (A3.2a) or (A3.2b).

At the entrance electrode $\hat{\phi} = 1/2$ by definition. If we wish to avoid the appearance of a virtual cathode between the electrodes we must have $\hat{\phi}_m > 0$ in (A3.2a); this requires $c_0 < 0$ or $-\sqrt{2} < \hat{E}_0 < 0$. In fact it can be shown that the solutions are stable only over a narrower range $-1 \leq \hat{E}_0 < 0$, the rest of the range leading to physically unrealizable solutions due to hysteresis effects [26]. In the presence of ions the situation is more complex, since we have an additional variable in the form of $\hat{\alpha}$. Now it is best to plot $\hat{E} = d\hat{\phi}/d\hat{x}$ as a function of $\hat{\phi}$, (A3.2b) and Fig. A3.3. We find that $\hat{E} = 0$ either when $\hat{\phi} = \hat{\phi}_{\min}$ or $\hat{\phi} = \hat{\phi}_{\max}$, the two values being given by (A3.3). In order to avoid the appearance of a virtual cathode between the electrodes, we again must have $\hat{\phi}_{\min} > 0$ or from (A3.3), $c < 0$. Substituting for c from (A3.2b) we now find that we also have

$$\hat{E}_0^2 < 2 - \hat{\alpha} \quad (A3.4)$$

which is a general restriction on the values of \hat{E}_0 . The curve $c = 0$ is shown in Fig. A3.4, the allowed values of \hat{E}_0 being shaded. It is to be noted that for $\hat{\alpha} = 1$ we have $-1 < \hat{E}_0 < 1$ as noted by Godfrey [14]. The limitation on $\hat{\alpha}$ to values which are less than two is simply due to the fact that for $\hat{\alpha} > 2$ the slope \hat{E}_0 would have to be so large, that it would inevitably lead to the appearance of a virtual cathode, or $\hat{\phi}_{\min} < 0$; this is also expressed by the properties of the function $\hat{E} = \hat{E}(\hat{\phi})$, Eq. (A3.2b) and the corresponding Fig. A3.3. In fact since from (A3.2b) and (A3.3) $\hat{\phi}$ cannot be negative, the electrons being initially emitted with zero velocity from a cathode at zero potential, the curve shown in Fig. A3.3 fails to cut the horizontal axis for $c > 0$ and assumes a value $\hat{E}_0 \neq 0$ at $\hat{\phi} = 0$ (shown dotted). There is one exception to the above restrictions on the value of \hat{E}_0 and $\hat{\alpha}$ shown in Fig. A3.4. When $0 < \hat{x}_L < \pi$ only a single min/max is possible between the electrodes. Thus if we choose $\hat{E}_0 > 0$, the solutions for $\hat{E}_0 < 0$ being unstable

in this case, we can have \hat{E}_0 or $\hat{\alpha}$ as large as we like, since there is no limitation on the value of $\hat{\phi}_{\max}$. Also it should be noted that in the absence of ions the curve shown in Fig. A3.3 becomes a parabola, Eq. (A3.2a); we then find from (A3.3) that for $\hat{\alpha} \rightarrow 0$ we have $\hat{\phi}_{\max} \rightarrow \infty$ and $\hat{\phi}_{\min} \rightarrow c^2/8$ in agreement with (A3.2a).

This brief discussion shows with the help of very simple algebra that the introduction of positive ions can enrich the dynamical behaviour of the system by substantially altering its physical properties.

$\hat{\alpha}$	First unstable point(\hat{x}_L/π)	First bifurcation point(\hat{x}_L/π)	First stable point(\hat{x}_L/π)
1.1250	2.54680	2.55385	2.87500
1.1125	2.54133	2.58714	2.87000
1.1000	2.58378	2.62345	2.91000
1.0750	2.66260	2.68955	2.95000
1.0620	2.70543	2.73750	2.97000
1.0500	2.72437	2.75273	3.10000
1.0250	2.79000	2.81416	3.15000
1.0100	2.82013	2.83875	2.92000
1.0000	2.84378	2.85817	2.89500
0.9900	2.86261	2.87160	2.89200
0.9850	2.87260	2.87940	2.89500
0.9840	2.97590	2.88100	2.89600
0.9830	2.87674	2.88286	
0.9820	2.87880	2.88400	

Table 1. Some critical points on the bifurcation diagrams with $\hat{R} = 0.01$

\hat{R}	Dynamic behaviour	
0-0.028	Chaos	
0.028-0.120	Limit cycle (Oscillations)	As \hat{R} increases, the amplitude of oscillation decreases
0.120 & above	Stable	No oscillations

Table 2a. $\hat{C} = 11$, $\hat{x}_L = 2.77\pi$, $\hat{\alpha} = 1$

\hat{R}	Dynamic behaviour	
0-0.025	Chaos	
0.025-0.108	Limit cycle (Oscillations)	As \hat{R} increases, the amplitude of oscillation decreases
0.108 & above	Stable	No oscillations

Table 2b. $\hat{C} = 20$, $\hat{x}_L = 2.82\pi$, $\hat{\alpha} = 1$

\hat{R}	Dynamic behaviour	
0-0.01	Chaos	
0.01-0.06	Limit cycle (Oscillations)	As \hat{R} increases, the amplitude of oscillation decreases
0.06 & above	Stable	No oscillations

Table 2c. $\hat{C} = 1000$, $\hat{x}_L = 2.857\pi$, $\hat{\alpha} = 1$

Table 2.

\hat{L}	Dynamic behaviour	
0.0 - 1.0	Chaos	
2.0	Period 4 cycle	
2.4	Period 2 cycle	
2.5	Period 2 cycle	
5.0	Limit cycle (Oscillations)	Amplitude of oscillations steadily decreases, so does the rate of convergence

Table 3a. $\hat{C} = 11.0$, $\hat{x}_L = 2.77\pi$, $\hat{R} = 0.01$, $\hat{\alpha} = 1$

\hat{L}	Dynamic behaviour	
0-1.0	Chaos	
0.5	Period 3 cycle	
1.0	Period 2 cycle	
2.4	First bifurcation point	
10.0 and beyond	Limit cycle (Oscillations)	Amplitude of oscillations steadily decreases, so does the rate of convergence

Table 3b. $\hat{C} = 20.0$, $\hat{x}_L = 2.82\pi$, $\hat{R} = 0.01$, $\hat{\alpha} = 1$

\hat{L}	Dynamic behaviour	
0.0	Period 2 cycle	
10.0 and beyond	Limit cycle (Oscillations)	Amplitude of oscillations steadily decreases, so does the rate of convergence

Table 3c. $\hat{C} = 1000.0$, $\hat{x}_L = 2.857\pi$, $\hat{R} = 0.01$, $\hat{\alpha} = 1$

Table 3.

\hat{L}	Dynamic behaviour	
0.0	Chaos	
1.0	Period 2 cycle	
1.5	Period 2 cycle	
5.0 and beyond	Limit cycle (Oscillations)	Amplitude of oscillations steadily decreases, so does the rate of convergence

Table 4. $\hat{x}_L = 2.82\pi$, $\hat{R} = 0.0$, $\hat{C} = 20.0$

References

1. L. D. Smullin & P. Chorney, Propagation in ion-loaded waveguides, Proc. Symp. on Electronic Waveguides, Brooklyn Polytechnic Press, Brooklyn N.Y., 1958, pp. 229-247.
2. G. D. Boyd, L. M. Field & R. W. Gould, Excitation of plasma oscillations and growing plasma waves, *ibid*, pp. 367-375.
3. M. A. Allen & G. S. Kino, Interaction of an electron beam with a fully ionized Plasma, *Phys. Rev. Letters*, vol.6, 1961, pp. 163.
4. Z. S. Chernov and G. A. Bernashevski, Amplification of microwaves by means of plasma, Proc. Symp. on Electromagnetics and Fluid Dynamics of Gaseous Plasma, Brooklyn Polytechnic Press, Brooklyn N.Y., 1961, pp. 31-35.
5. M. T. Vlaardingerbroek, K. R. V. Weimer and H.J.C.A.Nunnink, On wave propagation in beams-plasma systems, *Philips Res. Rep.*, vol.17, 1962, pp. 344-362.
6. P. B. Curtis, R. L. Ferrari and W.I. Moore, A study of the plasma travelling-wave amplifier, *Microwaves*, Proc. 4th Int. Congress, Centrex Publishing Co., Eindhoven 1963, pp. 317-321.
7. R. J. Briggs, Electron stream interaction with plasmas, Research Monograph No.29, MIT Press, Cambridge, MA, 1964.
8. F. J. Agee, Basic research in high power microwaves, The US Program; Digest of Technical Papers, Int. Workshop on High Power Microwave Generation and Pulse Shortening, Eginburgh, 10-12 June 1997, pp. 1-8.
9. H. Yoshida, M. Masuzaki, S. Ooyama, R. Ando and K. Kamada, Measurements of broad-band millimeter-wave radiation from an IREB-plasma interaction system, *IEEE Trans. Plasma Science*, vol.27, 1999, pp. 682-687.
10. W. Jiang, K. Woolverton, J. Dickens and M. Kristiansen, High power microwave generation by a coaxial virtual cathode oscillator, *IEEE Trans. Plasma Science*, vol.27, 1999, pp. 1538-1542.
11. J. R. Pierce, Limiting stable current in electron beams in the presence of ions, *J. Appl. Phys.*, vol.15, 1994, pp. 721-726.

- 12 J. R. Cary and D.S. Lemons, Unstable oscillatory Pierce modes of neutralized electron beams, *J. Appl. Phys.*, vol.53, 1982, pp.3303-3304.
- 13 T. L. Crystal and S. Kuhn, Particle simulation of the low- α Pierce diode, *Phys. Fluids*, vol. 28, 1985, pp. 2116-2124.
- 14 B. B. Godfrey, Oscillatory nonlinear electron flow in a Pierce diode, *Phys. Fluids*, vol. 30, 1987, pp.1553-1560.
- 15 P.A. Lindsay, X. Chen and M. Xu, Plasma/e-m field interaction and chaos, *Int. J. Electronics*, vol. 79, 1995, pp.237-250.
- 16 X. Chen and P.A. Lindsay, Oscillations and chaos in plasma-filled diodes, *IEEE Trans. Plasma Science*, vol. 24, 1996, pp. 1005-1014.
- 17 M. A. Raadu and M. B. Silevitch, Circuit effects on Pierce instabilities, *J. Appl. Phys.*, vol. 54, 1983, pp.7192-7194.
- 18 S. Kuhn and M. Hoerhager, External-circuit effects on Pierce-diode stability behavior, *J. Appl. Phys.*, vol. 60, 1986, pp.1952-1959.
- 19 X. Chen, P. A. Lindsay, and J. Zhang, The effect of load on chaos and oscillations in a plasma-filled diode, *6th International Workshop on Nonliear Dynamics of Electronic Systems*, Budapest, Hungary, 16-18 July 1998, pp. 293-298.
- 20 W.S. Lawson, The Pierce diode with an external circuit: simulations in the linear region, *J. Appl. Phys.*, vol.64, 1988, pp.4838-4842.
- 21 W.S. Lawson, Particle simulation of bounded 1D plasma systems, *J. Computational Phys.*, vol.80, 1989, pp.253-276.
- 22 W.S. Lawson, The Pierce diode with an external circuit. I. Oscillations about nonuniform equilibria, *Phys. Fluids B*, vol.1, 1989, pp. 1483-1492; II Chaotic behavior, *ibid*, pp.1493-1501.
- 23 S. Kuhn, Linear longitudiual oscillations in collisionless plasma diode with thin sheaths Part I. Method, *Phys. Fluids*, vol. 27, 1984, pp.1821-1833;Part II, Application to an extended Pierce-type problem, *ibid.*, pp.1834-1851
- 24 X. Chen and P.A. Lindsay, Some features of chaos and oscillations in plasma-filled diodes, *4th International Workshop on Nonlinear Dynamics of Electronic Systems*, Seville, Spain, 27-28 June 1996, pp. 471-476.

25 P.A. Lindsay, X. Chen, J. Watkins and J. Zhang, Controlling Chaos in Plasma-filled Diodes, AFOSR Grant No. F49620-97-1-0035, Progress Report, August'97-July'98.

26 C. K. Birdsall and W. B. Bridges, Electron dynamics of diode regions, Academic Press, New York 1966.

27 C. K. Birdsall and A. B. Langdon, Plasma physics via computer simulation, McGraw-Hill, New York 1985.

28 P. A. Lindsay, J. Watkins and X. Chen, Controlling chaos in plasma filled diodes, EOARD Grant F49620-92-J-0219, P00001; Final Report May 1992-Nov 93.

29 C. K. Birdsall, Particle-in-cell charged-particle simulations, plus Monte Carlo collisions with neutral atoms, PIC-MICC, IEEE Trans. Plasma Science vol.19, 1991, pp. 65-85.

30 Rohde, H. Klostermann and A. Piel, Particle-in-cell simulation of grid sheath oscillations in a double-plasma device, IEEE Trans. Plasma Science vol. 25, 1997, pp. 1144-1149.

31 L.D. Ludeking, B. Goplen, D. Smithe, MAGIC User's Manual, Mission Research Corp., VA, USA, August, 1997.

32 B. Goplen, L. Ludeking, D. Smithe, and G. Warren, User-configurable MAGIC Code for Electromagnetic PIC Calculations, Computer Physics Communications, vol.87, pp. 54-86, 1995.

33 V. M. Smirnov, Instability of nonlinear stationary potential oscillations in electron-ion beams, Soviet Physics-JETP, vol. 23, 1966, pp. 668-672.

34 W.S. Lawson, Particle simulation of bounded 1D plasma systems, J. Computational Phys., vol.80, 1989, pp.253-276.

35 W. J. Kleen, Electronics of microwave tubes, Academic Press, New York 1958; Ch. 3, pp. 21-27.

36 X. Chen and P.A. Lindsay, Investigation of oscillations and chaos in a plasma-filled diode, Intense Microwave Pulses III, SPIE vol. 2557, 1995, pp.88-97.

37 J. M. T. Thompson and H. B. Stewart, Nonlinear Dynamics and Chaos. New York: Wiley, 1986.

38 A. J. Lichtenberg and M. A. Lieberman, Regular and chaotic dynamics. Berlin: Springer-Verlag, 1992.

39 E. A. Coutsias and D. J. Sullicvan, Space-charge -limit instabilities in electron beams, Phys. Rev. A, vol. 27, 1983, pp. 1535-1543.

40 E. Ott, C. Grebogi and J.A. Yorke, 'Controlling chaos', Phys. Rev. Lett., vol. 64, pp.1196-1199,1990.

41 Troy Shinbrot, Edward Ott, Celso Grebogi and James A. Yorke, 'Using chaos to direct trajectories to targets', Phys. Rev. Lett., vol. 65, pp.3215-3218, 1990.

42 W. L. Ditto, S. N. Rauseo and M. L. Spano, 'Experimental control of chaos', Phys. Rev. Lett., vol. 65, pp. 3211-3214, 1990.

43 Troy Shinbrot, William Ditto, Celso Grebogi, Edward Ott, Mark Spano and James A. Yorke, 'Using the sensitive dependence of chaos (the 'butterfly effect') to direct trajectories in an experimental chaotic system', Phys. Rev. Lett., vol. 68, pp. 2863-2866, 1992.

44 J. Singer, Y-Z. Wang and Haim H. Bau, 'Controlling a chaotic system', Phys. Rev. Lett., vol. 66, pp. 1123-1125, 1991.

45 T. C. Newell, P. M. Alsing, A. Gavrielides and V. Kovanis, 'Synchronization of chaotic diode resonators by occasional proportional feedback', Phys. Rev. Lett., vol. 72, pp. 1647-1650, 1994.

46 Y. Braiman and I. Goldhirsch, 'Taming chaotic dynamics with weak periodic perturbations', Phys. Rev. Lett., vol. 66, pp. 2545-2548, 1991.

47 Holger Friedel, Rainer Grauer and Karl H. Spatschek, 'Controlling chaotic states of a Pierce diode', Phys. Plasmas, vol. 5, pp. 3187-3194, 1998.

48 X. Chen, P. A. Lindsay and J. Zhang, Chaos and oscillations in a loaded plasma-filled diode, Trans. IEEE Plasma Science, vol. 28, 2000 (accepted for publication).

49 X.Chen and P.A.Lindsay, Chaos in a plasma-filled diode, Conference on Vacuum Electronics and Displays, Garmisch-Partenkirchen, 1995; Published in ITG-Fachbericht 132/IEEE, pp.1-5. VDE-Verlag, Berlin 1995.

50 X.Chen and P.A.Lindsay, Physical interpretation of oscillations and chaos in a plasma-filled diode, 39th Annual Meeting, American Physical Society, Division of Plasma Physics, Pittsburgh PA. 1997.

- 51 P.A. Lindsay, X.Chen, J.Watknis, C.Xiong and J.Zhang, Oscillations and chaos in a plasma-filled diode-three different computational methods, IEEE Int. Conference on Plasma Science, Raleigh NC, 1998.
- 52 C. E. Fay, A. L. Samuel and W. Shockley, On the theory of space charge between parallel plane electrodes, BSTJ, vol. 17, pp. 49-79, 1938.

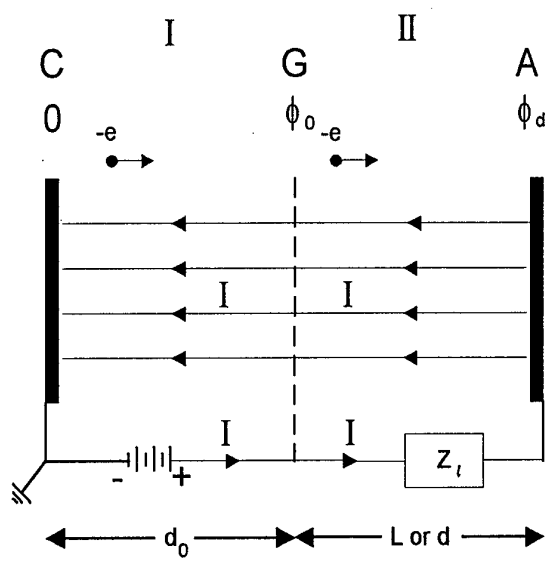


Fig.1 Plasma-filled diode where both DC and AC components of current flow through the load

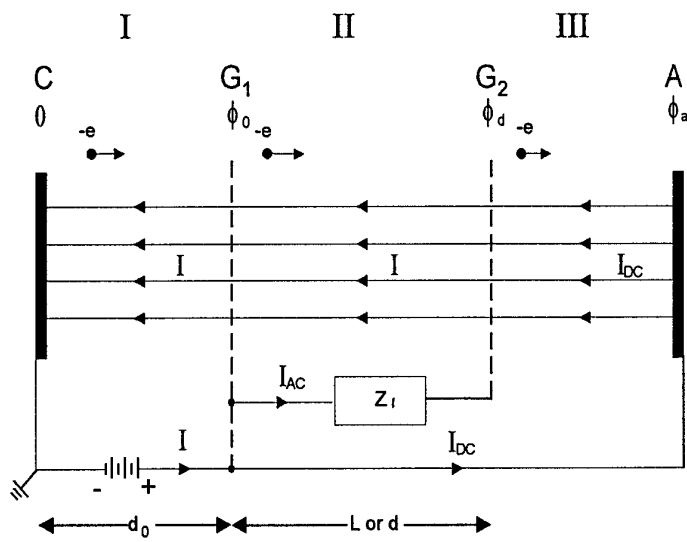


Fig.2 Plasma-filled diode where only the AC component of current flows through the load

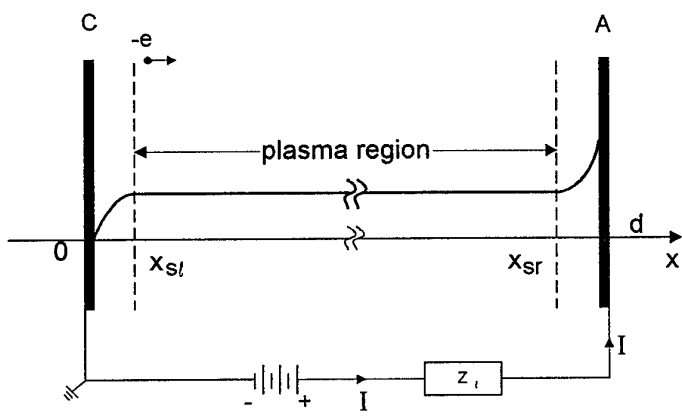


Fig.3 Q-machine with a load.

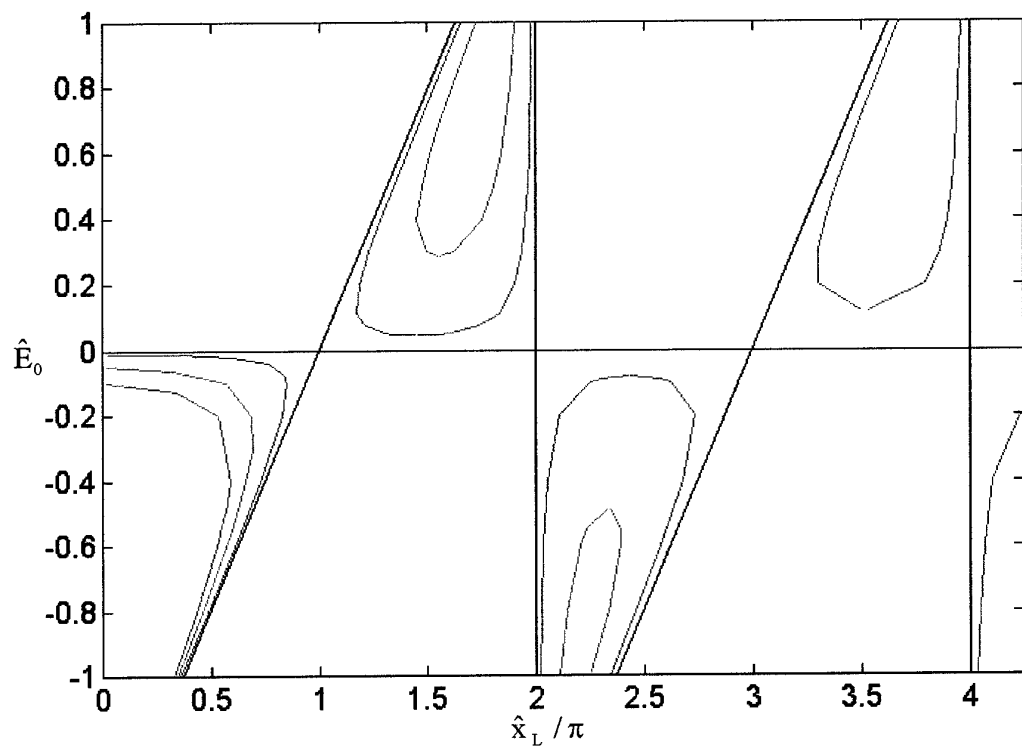


Fig. 4 Dispersion curves $\hat{E}_0(\hat{x}_L)$
 (Red: $\hat{R} = 0.01$; Blue: $\hat{R} = 0.05$; Green: $\hat{R} = 0.1$; Black: $\hat{R} = 0$)

f

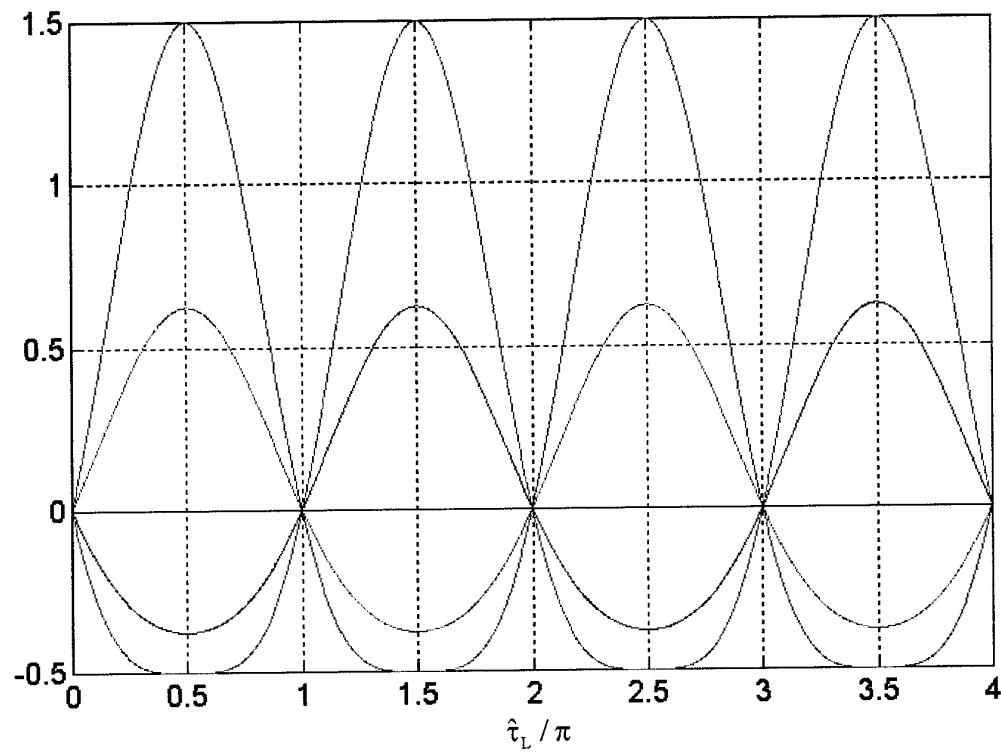


Fig.5 ($f = \hat{E}_0 \sin \hat{\tau}_L + \frac{1}{2} \hat{E}_0^2 \sin^2 \hat{\tau}_L$)

Red: $\hat{E}_0 = 1.0$; Blue: $\hat{E}_0 = 0.5$; Black: $\hat{E}_0 = 0.0$; Peach: $\hat{E}_0 = -0.5$; Green: $\hat{E}_0 = -1.0$

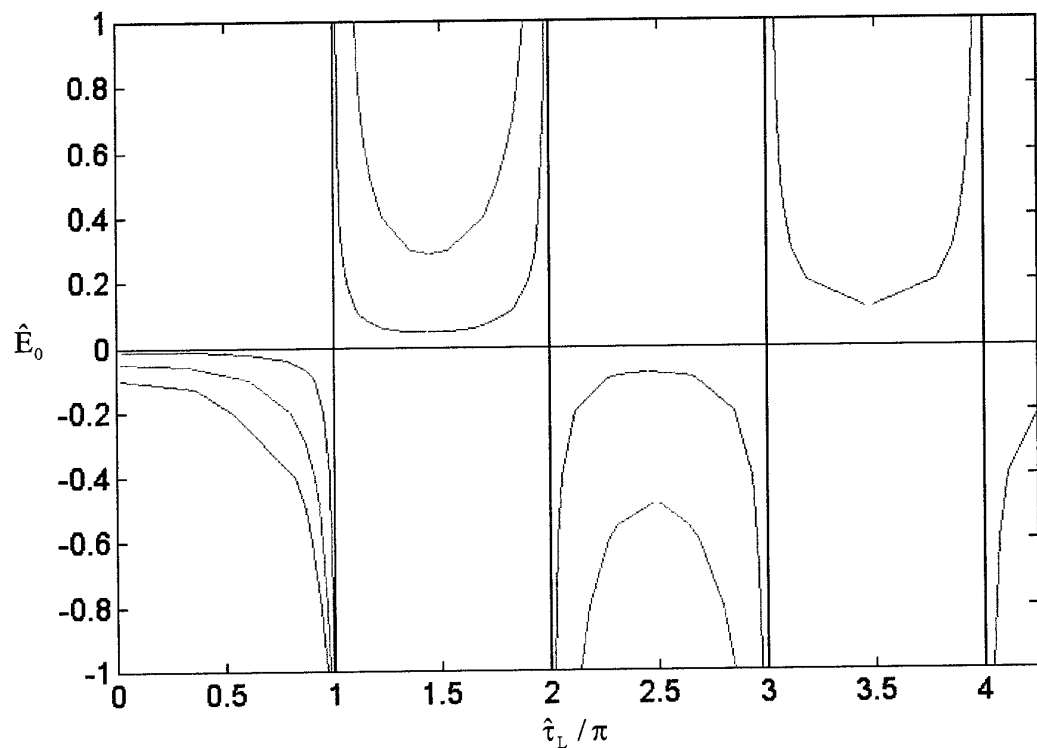


Fig 6 Dispersion curves $\hat{E}_0(\hat{\tau}_L)$
 (Red: $\hat{R} = 0.01$; Blue: $\hat{R} = 0.05$; Green: $\hat{R} = 0.1$; Black: $\hat{R} = 0$)

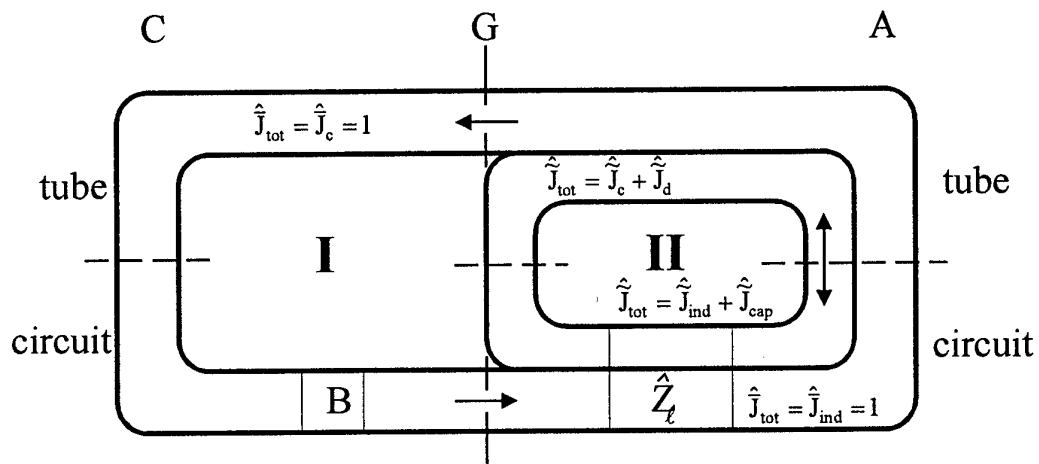


Fig. 7 Distribution of currents in a system shown in Fig. 1; B- battery, \hat{Z}_t - load.

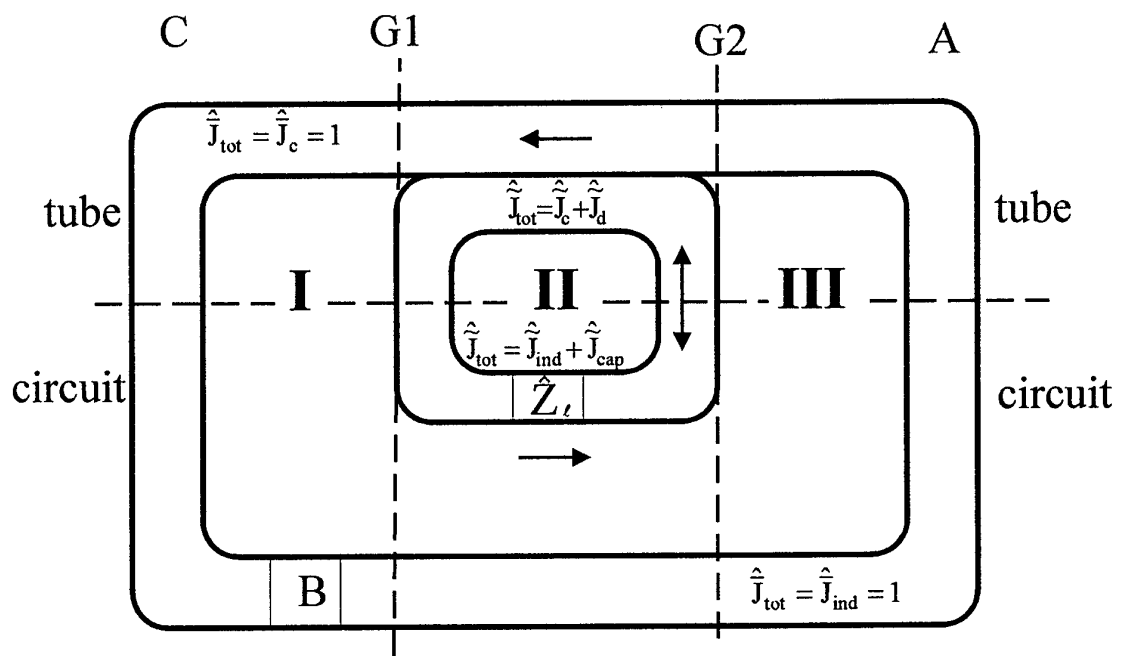


Fig.8 Distribution of currents in a system shown in Fig. 2; B- battery, \hat{Z}_t - load.

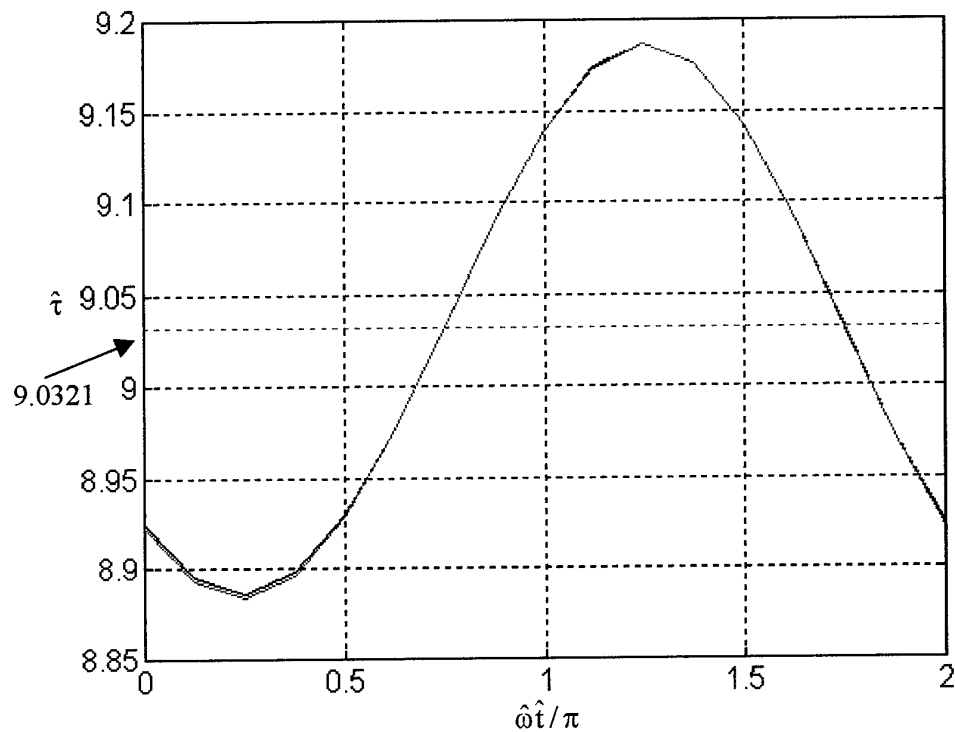


Fig.9 Transit time $\hat{\tau}$ as a function of the phase of oscillations $\hat{\omega}t/\pi$:
 black – from (5.2), red – from (5.3).

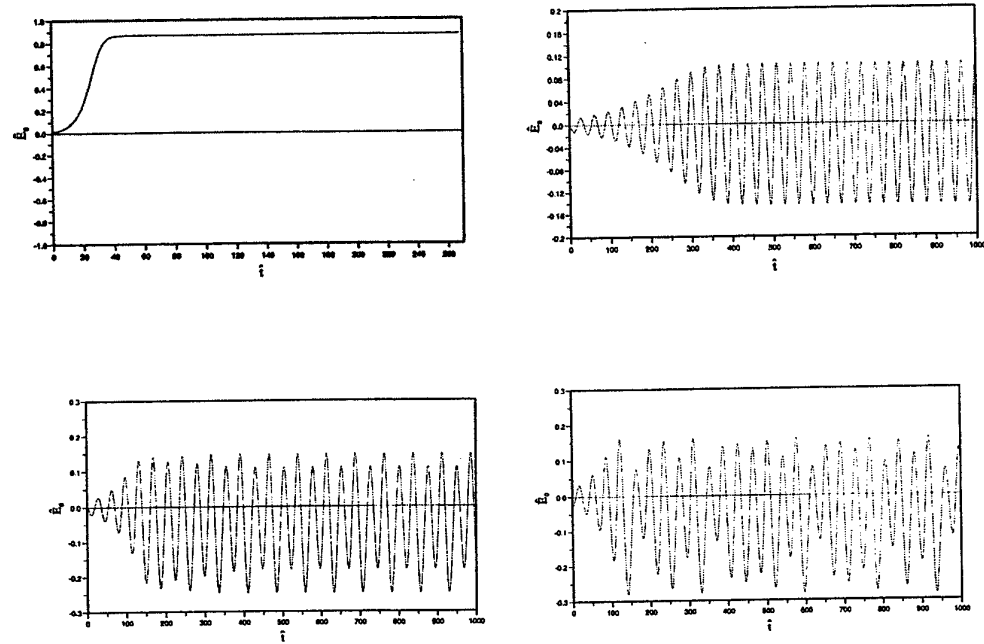
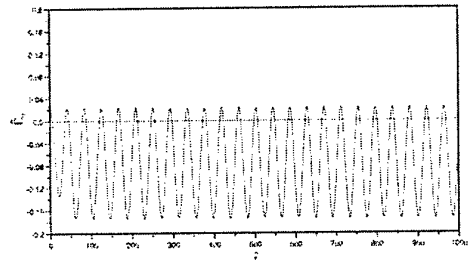
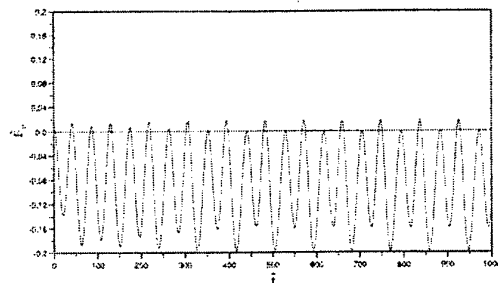


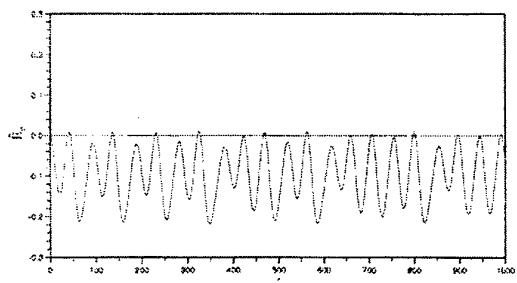
Fig. 10. The time history of the system for $\hat{\alpha} = 1$:
 (a) $\hat{x}_L = 1.5594\pi$, (b) $\hat{x}_L = 2.88\pi$, (c) $\hat{x}_L = 2.86\pi$ and (d) $\hat{x}_L = 2.855\pi$.



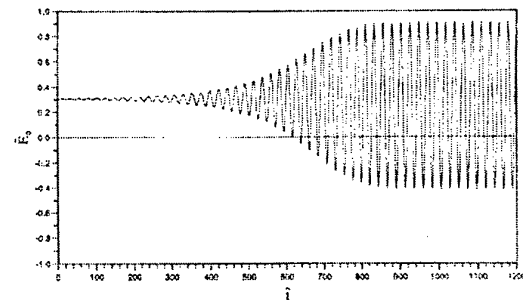
(a)



(b)

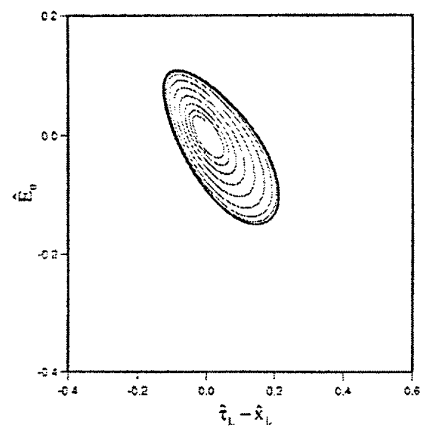


(c)

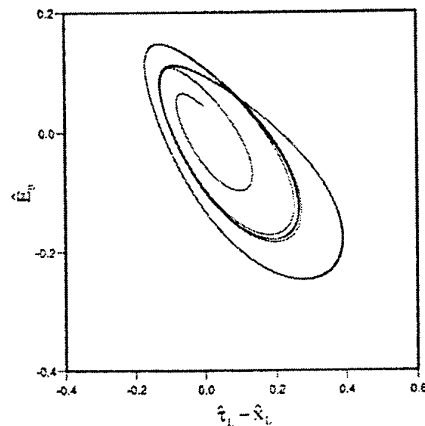


(d)

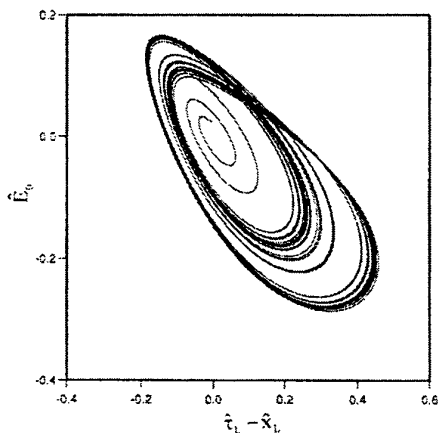
Fig. 11. The time history of the system for $\hat{x}_L = 2.88\pi$:
 (a) $\hat{\alpha} = 0.990$, (b) $\hat{\alpha} = 0.988$, (c) $\hat{\alpha} = 0.986$ and (d) $\hat{\alpha} = 1.05$.



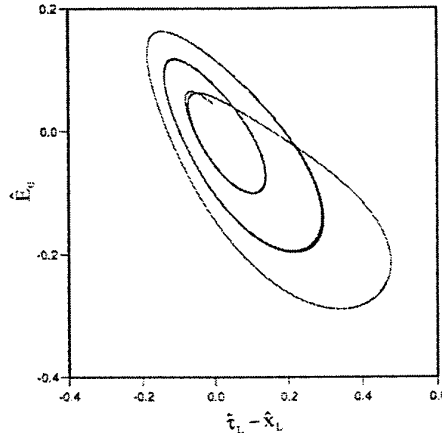
(a)



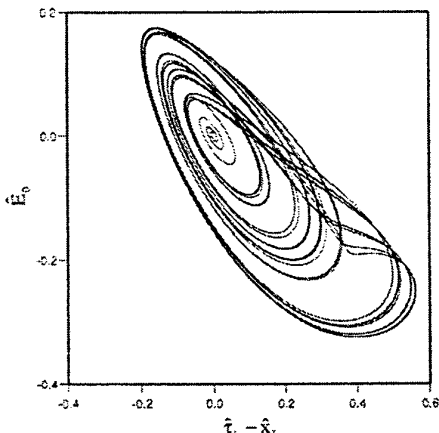
(b)



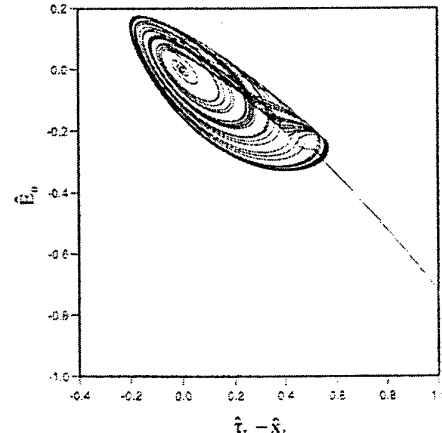
(c)



(d)



(e)



(f)

Fig. 12. Phase-space trajectories for $\hat{\alpha} = 1$: (a) $\hat{x}_L = 2.88\pi$, (b) $\hat{x}_L = 2.86\pi$, (c) $\hat{x}_L = 2.855\pi$, (d) $\hat{x}_L = 2.8541\pi$, (e) $\hat{x}_L = 2.8495\pi$ and (f) $\hat{x}_L = 2.8488\pi$

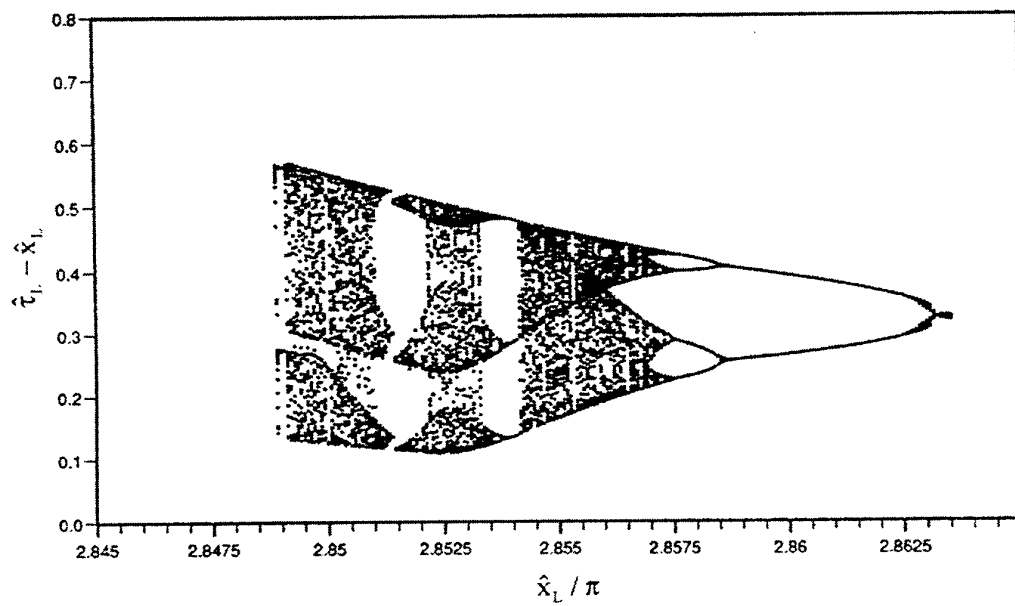


Fig.13 Bifurcation diagram for $\hat{\alpha} = 1$ and a range of \hat{x}_L

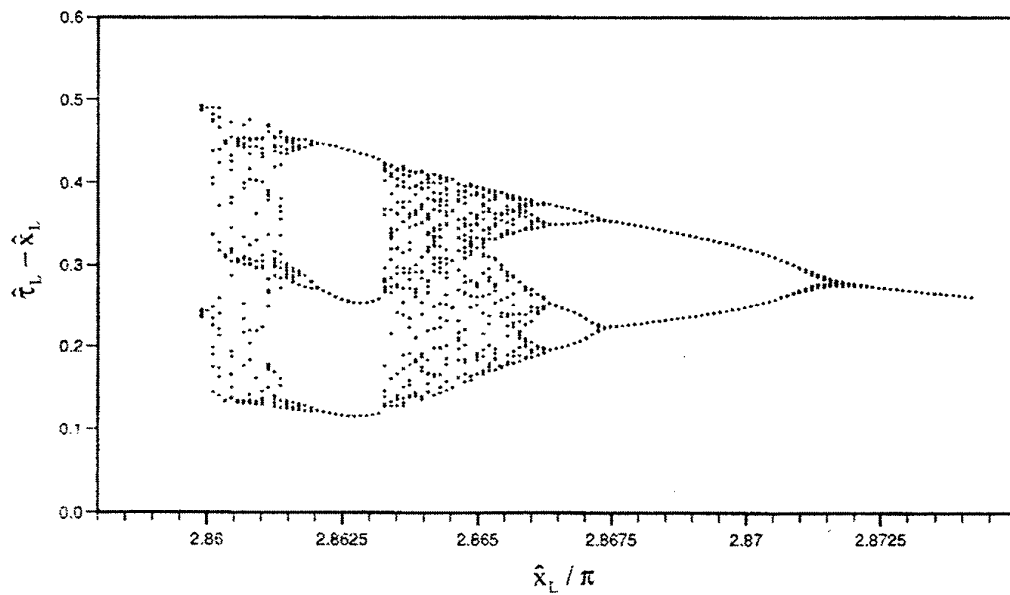


Fig.14 Bifurcation diagram for $\hat{\alpha} = 0.995$ and a range of \hat{x}_L

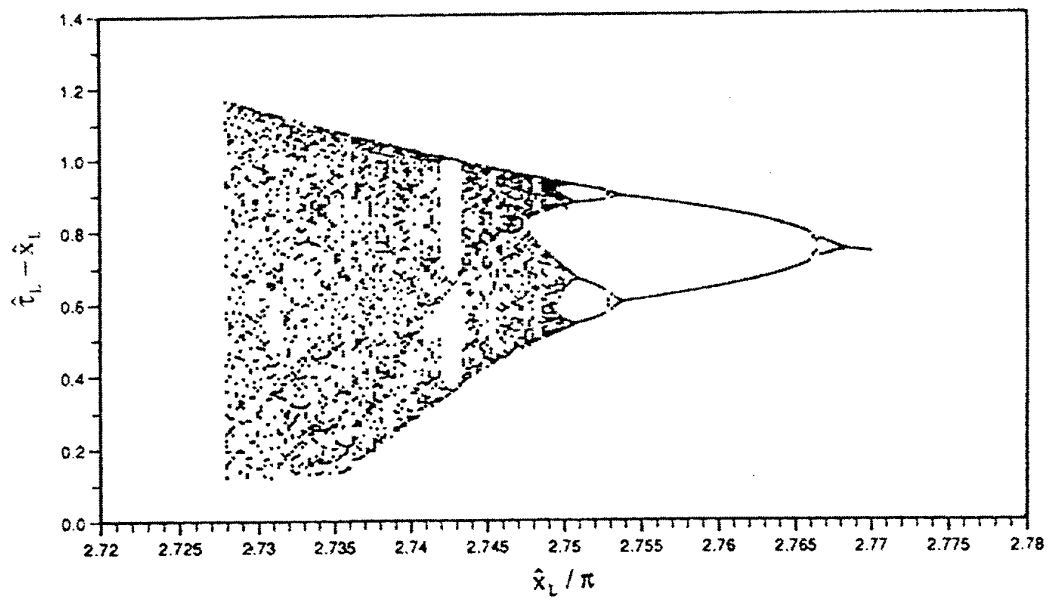


Fig.15 Bifurcation diagram for $\hat{\alpha} = 1.05$ and a range of \hat{x}_L

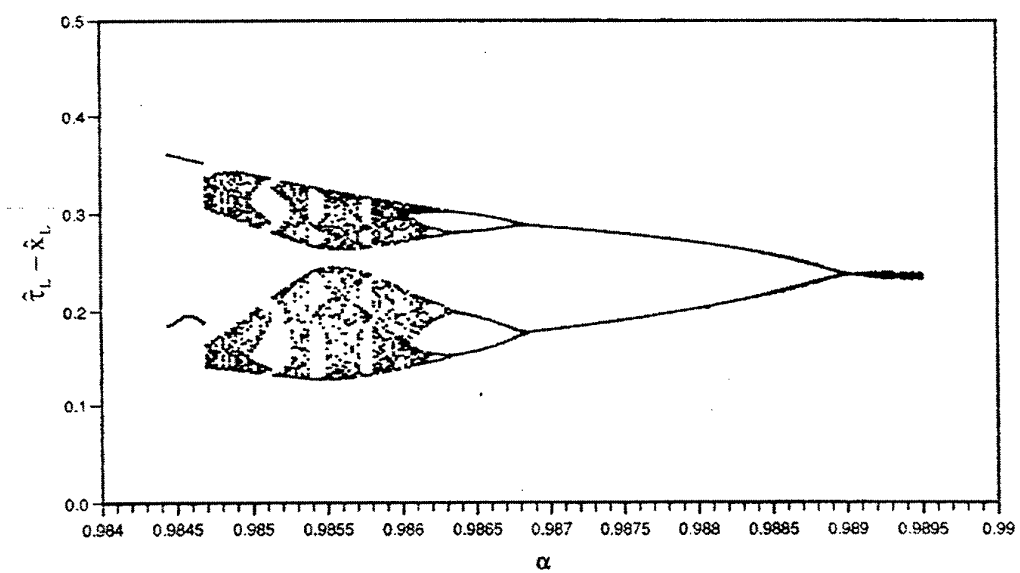


Fig.16 Bifurcation diagram for $\hat{x}_L = 2.88\pi$ and a range of $\hat{\alpha}$

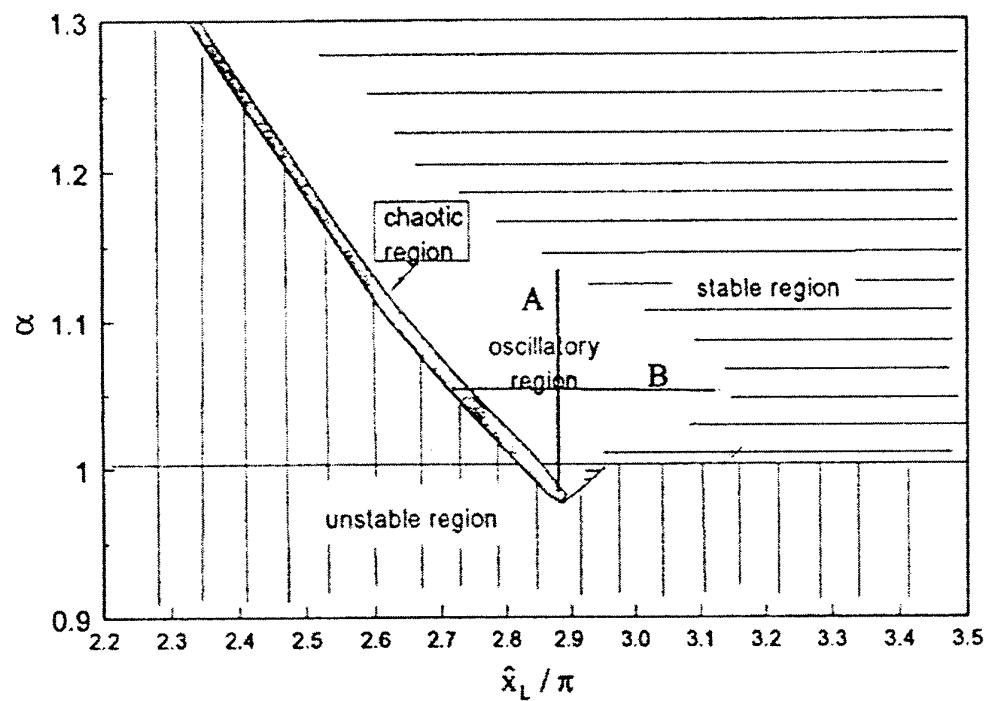


Fig. 17 An overall diagram of the dynamical behaviour of our model when short-circuited

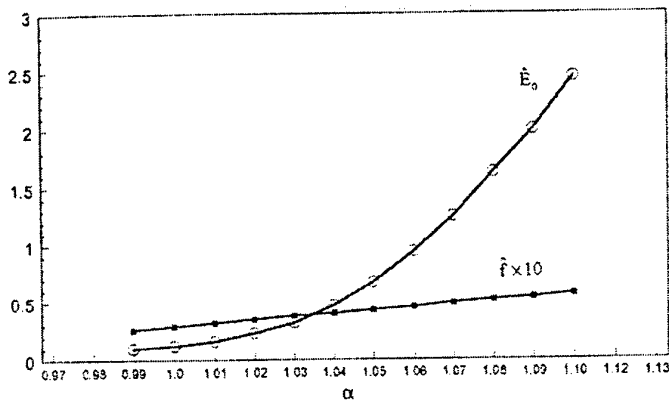


Fig.18 The amplitude $\hat{E}_{0,\max}$ and the frequency $\hat{f} = f / \omega_p$ along line A of Fig. 17.

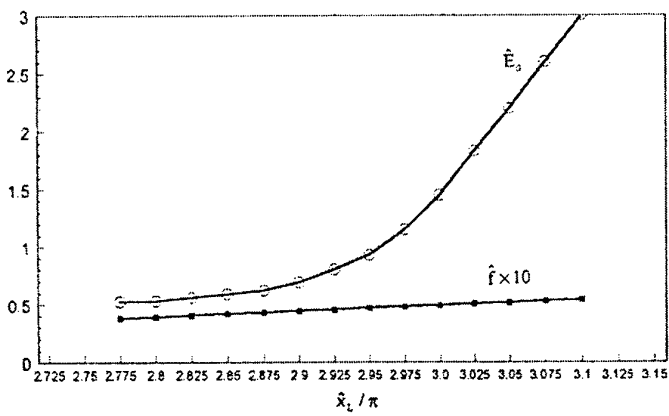


Fig.19 The amplitude $\hat{E}_{0,\max}$ and the frequency $\hat{f} = f / \omega_p$ along line B of Fig. 17.

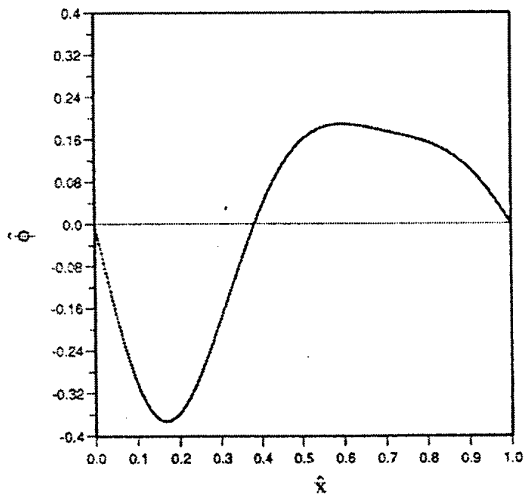


Fig.20 A typical potential distribution in the oscillatory regime

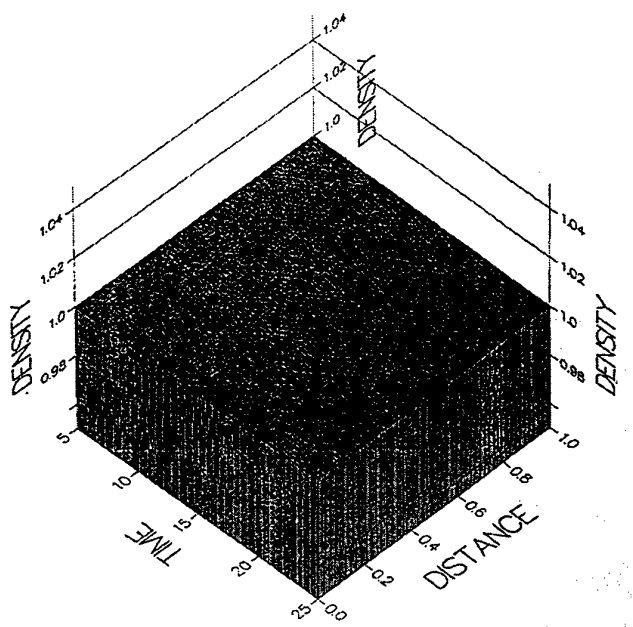
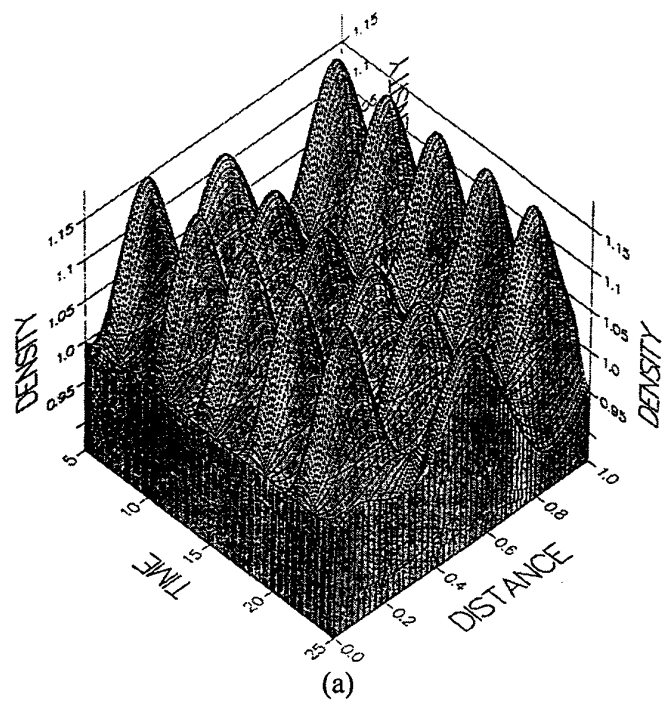
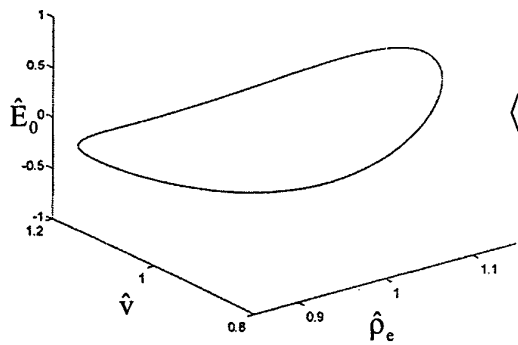


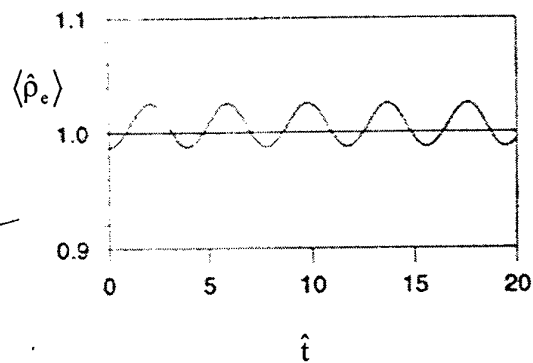
Fig. 21 Charge density $\hat{\rho}_e$ as a function of time \hat{t} and interelectrode distance \hat{x}



(a)

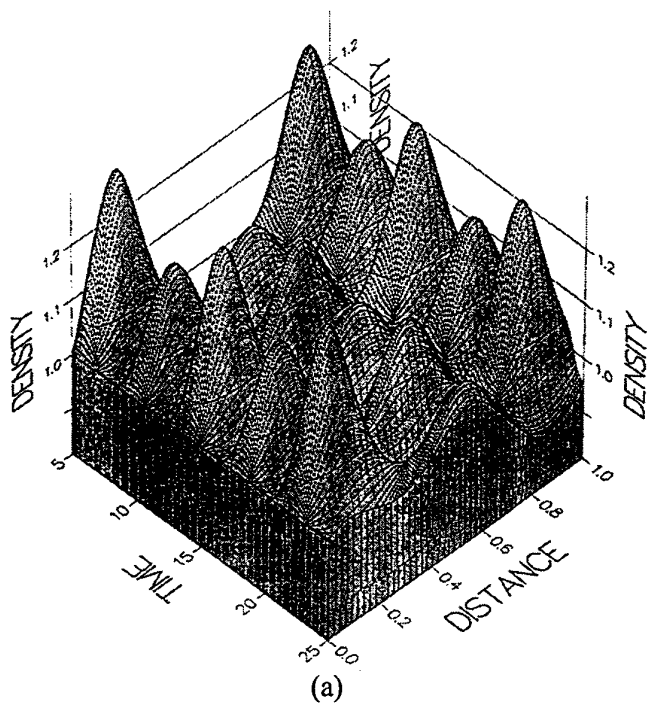


(b)

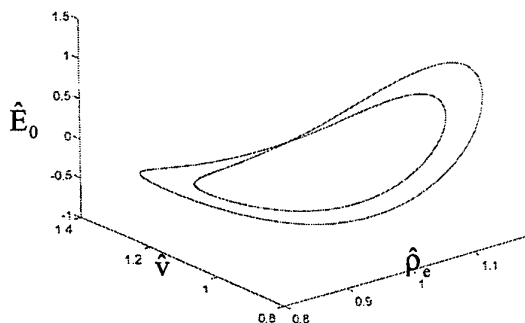


(c)

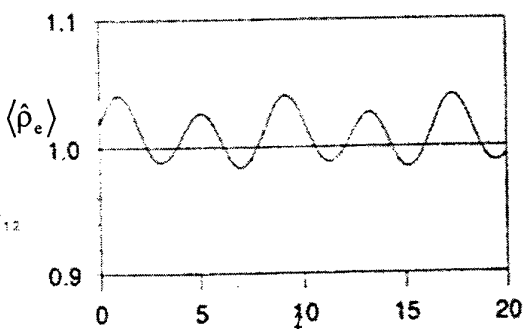
Fig.22 (a) Charge density $\hat{\rho}_e$ as a function of time \hat{t} and interelectrode distance \hat{x} ;
 (b) Corresponding phase space trajectory of the system;
 (c) Average interelectrode charge density $\langle \hat{\rho}_e \rangle$ as a function of time \hat{t} .



(a)

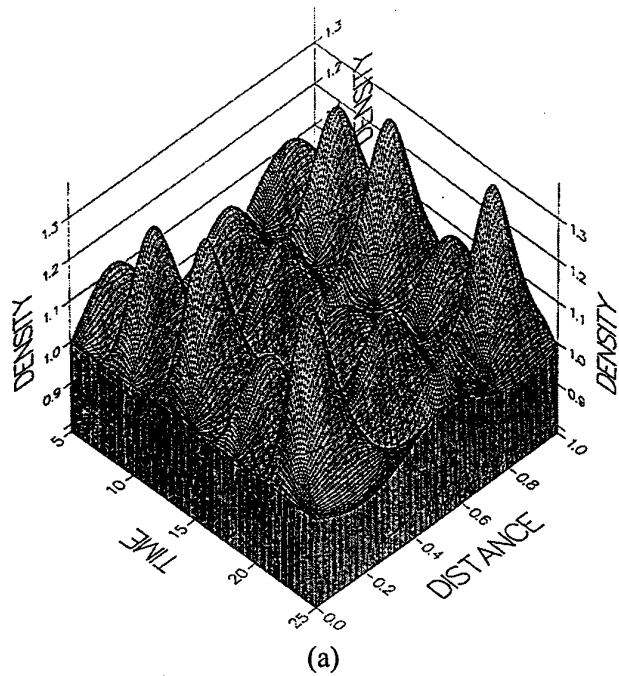


(b)

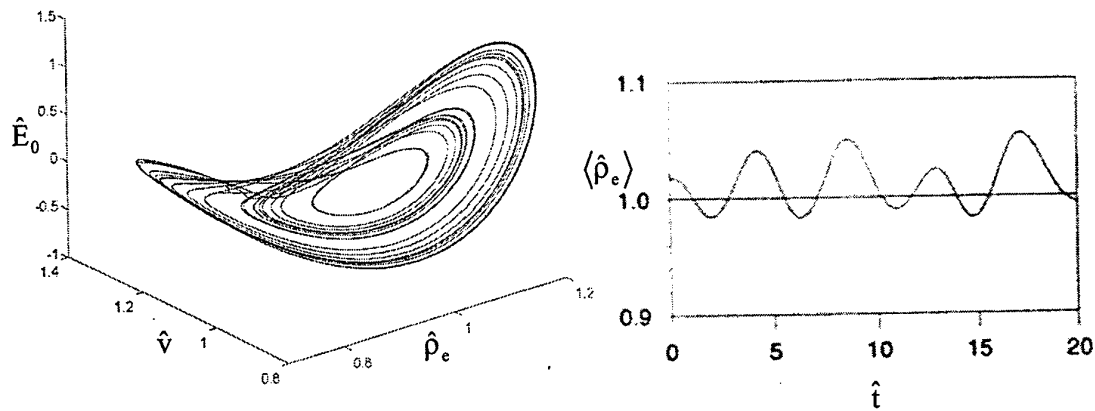


(c)

Fig. 23 (a) Charge density $\hat{\rho}_e$ as a function of time \hat{t} and interelectrode distance \hat{x} ;
 (b) Corresponding phase space trajectory of the system;
 (c) Average interelectrode charge density $\langle \hat{\rho}_e \rangle$ as a function of time \hat{t} .



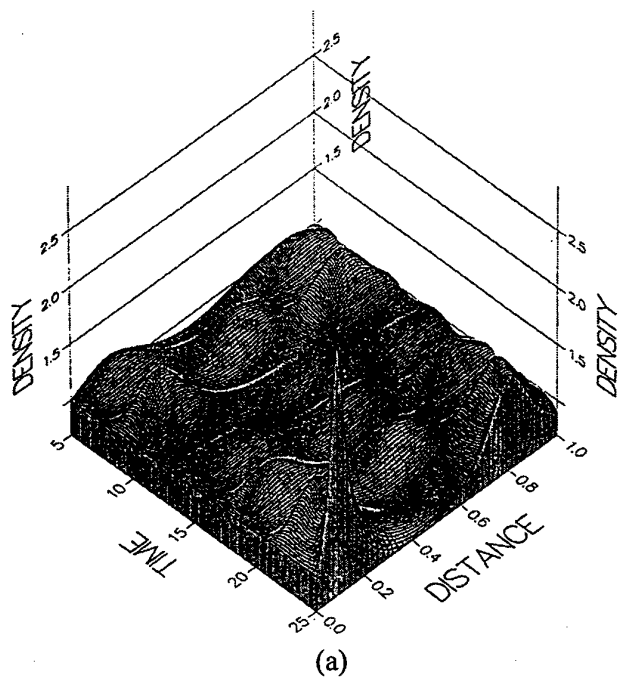
(a)



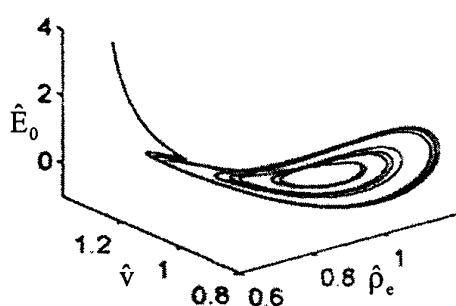
(b)

(c)

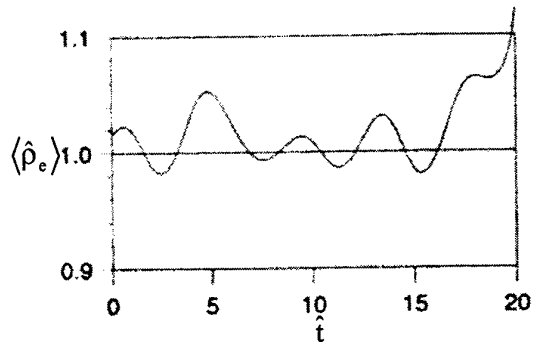
Fig. 24 (a) Charge density $\hat{\rho}_e$ as a function of time \hat{t} and interelectrode distance \hat{x} ;
 (b) Corresponding phase space trajectory of the system;
 (c) Average interelectrode charge density $\langle \hat{\rho}_e \rangle$ as a function of time \hat{t} .



(a)



(b)



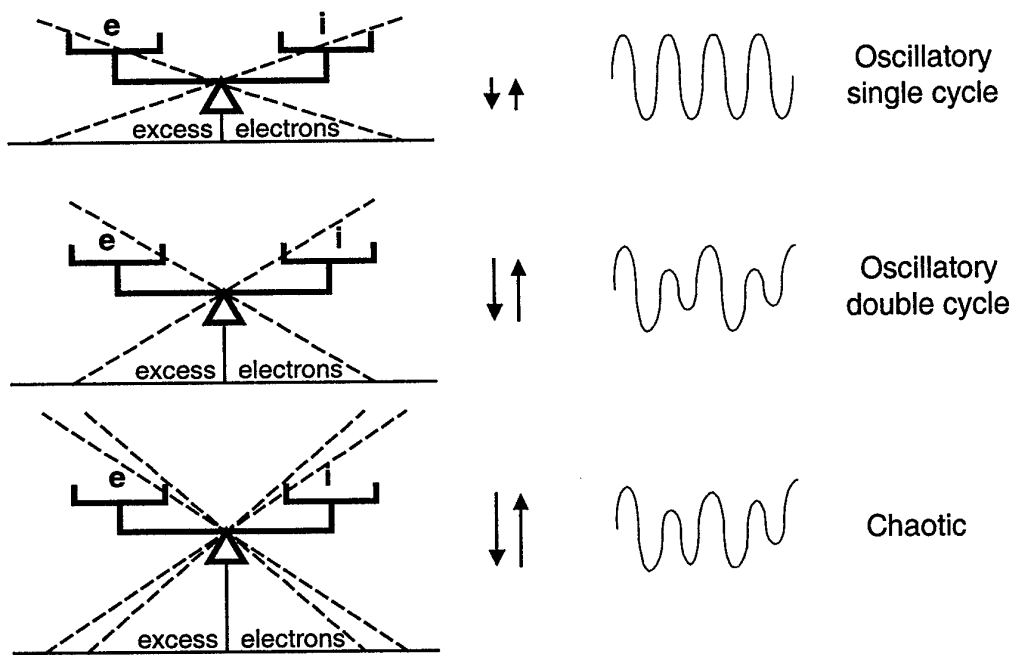
(c)

Fig. 25 (a) Charge density $\hat{\rho}_e$ as a function of time \hat{t} and interelectrode distance \hat{x} ;
 (b) Corresponding phase space trajectory of the system;
 (c) Average interelectrode charge density $\langle \hat{\rho}_e \rangle$ as a function of time \hat{t} .

Static Balance



Dynamic Balance



Out of Balance

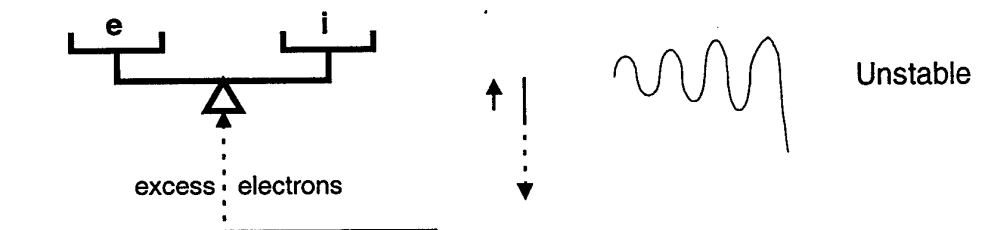


Fig.26 Diagrammatic representation of the four dynamic states of the diode ($\hat{\alpha} = 1$): stable, oscillatory chaotic and unstable;
e – electrons, i - ions

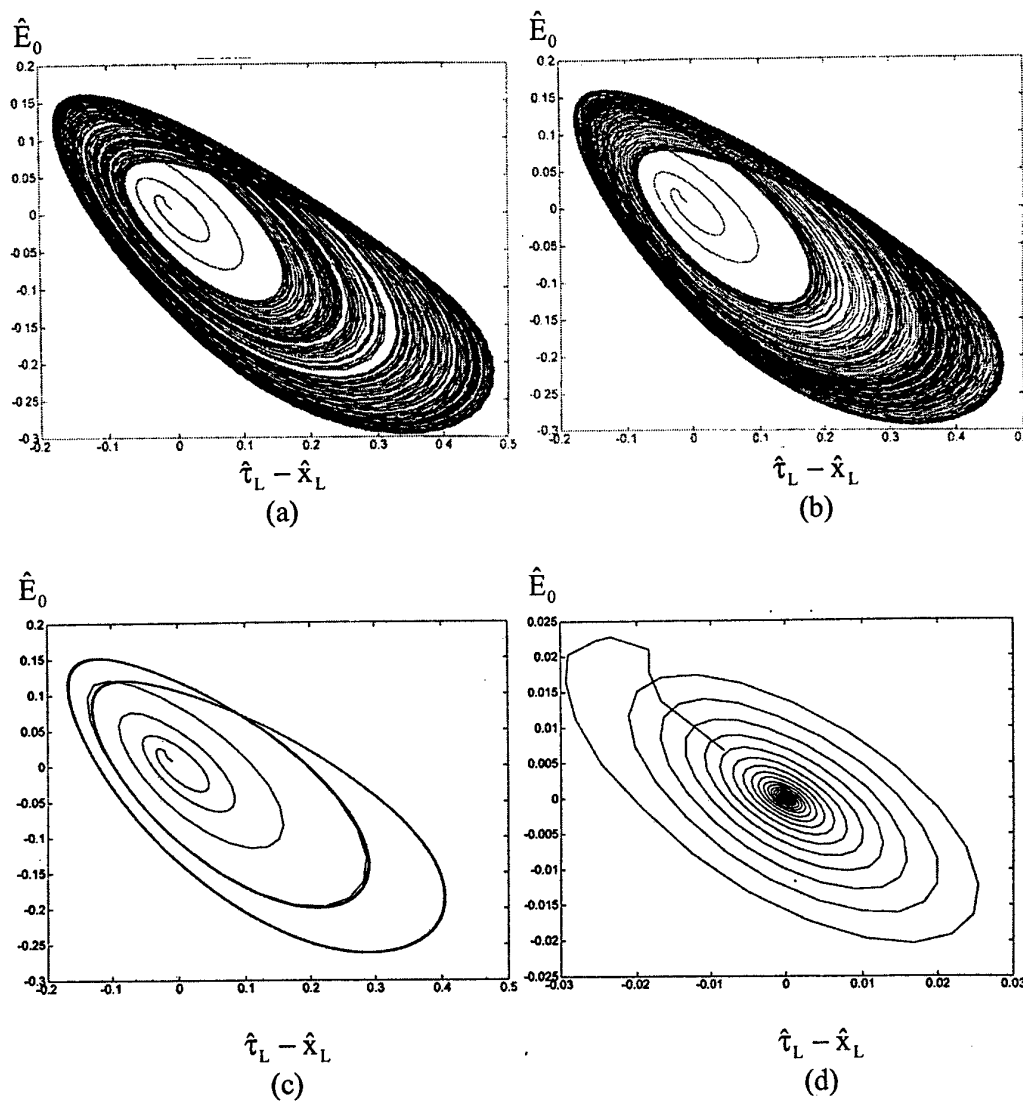


Fig. 27 Phase-space trajectories for $\hat{\alpha} = 1$, $\hat{x}_L = 2.855\pi$ and $\hat{C} = 10^6$;
 (a) $\hat{R} = 0.0001$, (b) $\hat{R} = 0.001$, (c) $\hat{R} = 0.01$ and (d) $\hat{R} = 0.1$.

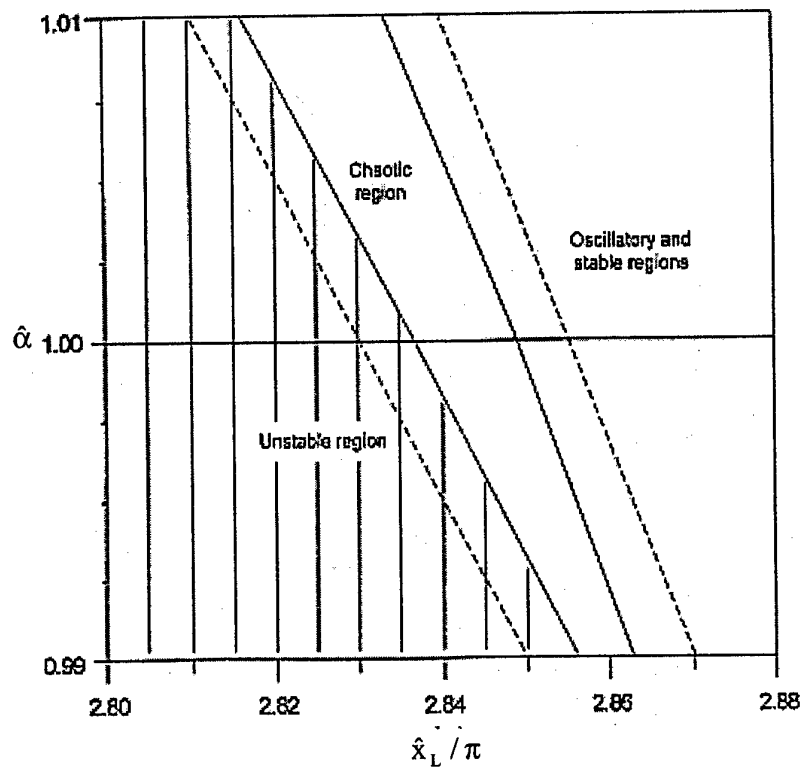


Fig. 28' A detail from Fig. 28 showing a shift in the chaotic band due to the load
 $\hat{R} = 0.01$; dotted lines indicate the position of the band when the diode is short-circuited.

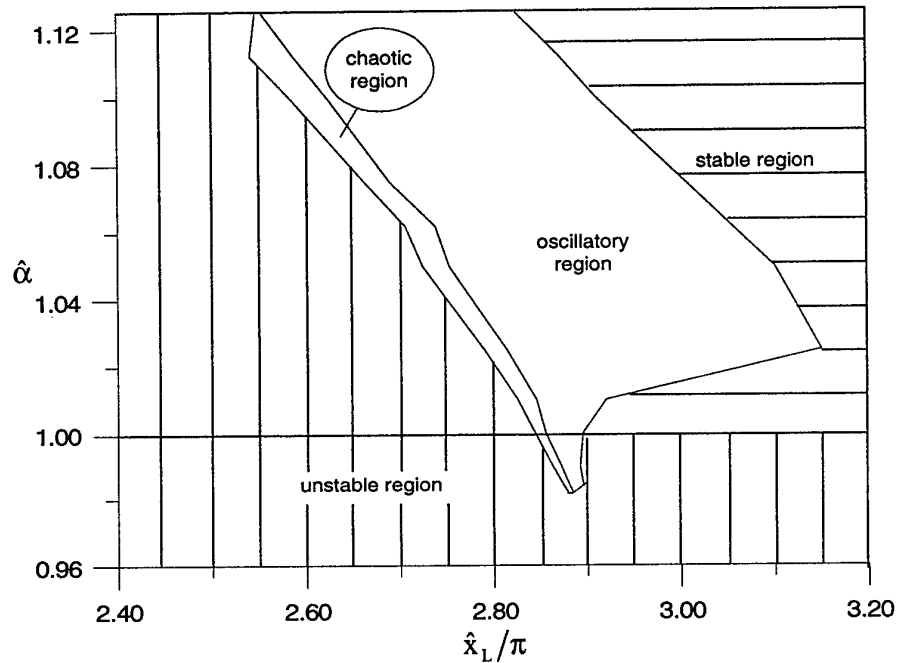


Fig. 28 An overall diagram of the dynamical behavior of the system with a purely resistive load $\hat{R} = 0.01$.

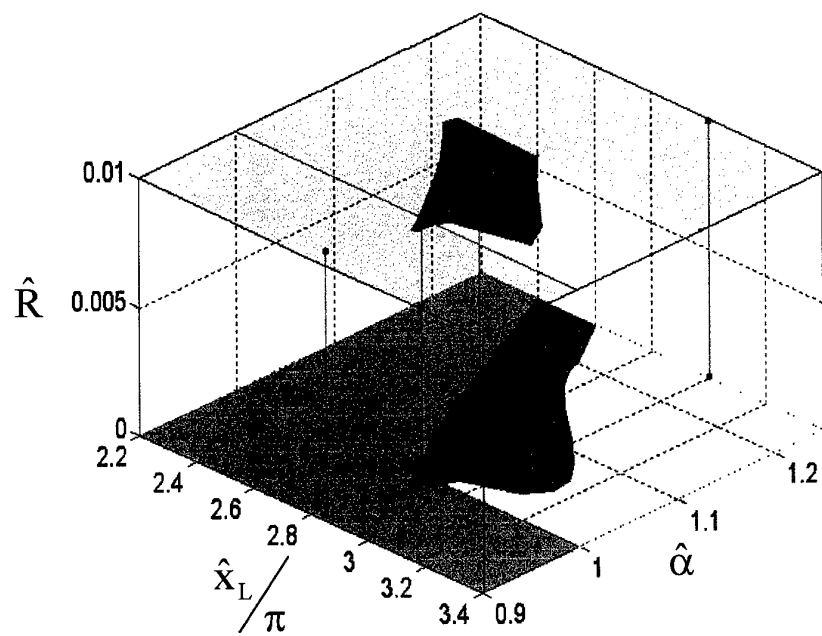


Fig. 29. A 3D representation of the dynamical behaviour of the diode for $\hat{R} = 0$ and $\hat{R} = 0.01$.

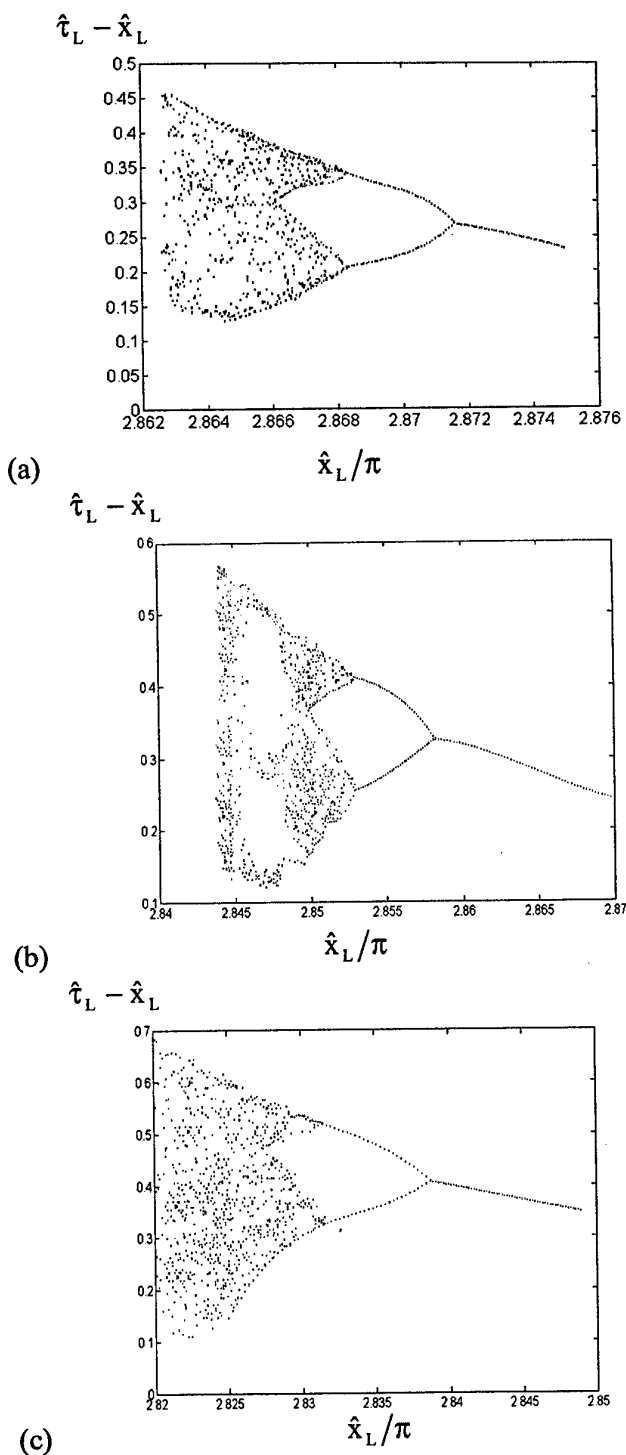


Fig. 30 Bifurcation diagrams: $\hat{R} = 0.01$ and a range of values of $\hat{\alpha}$;
 (a) $\hat{\alpha} = 0.99$, (b) $\hat{\alpha} = 1.0$ and (c) $\hat{\alpha} = 1.01$.

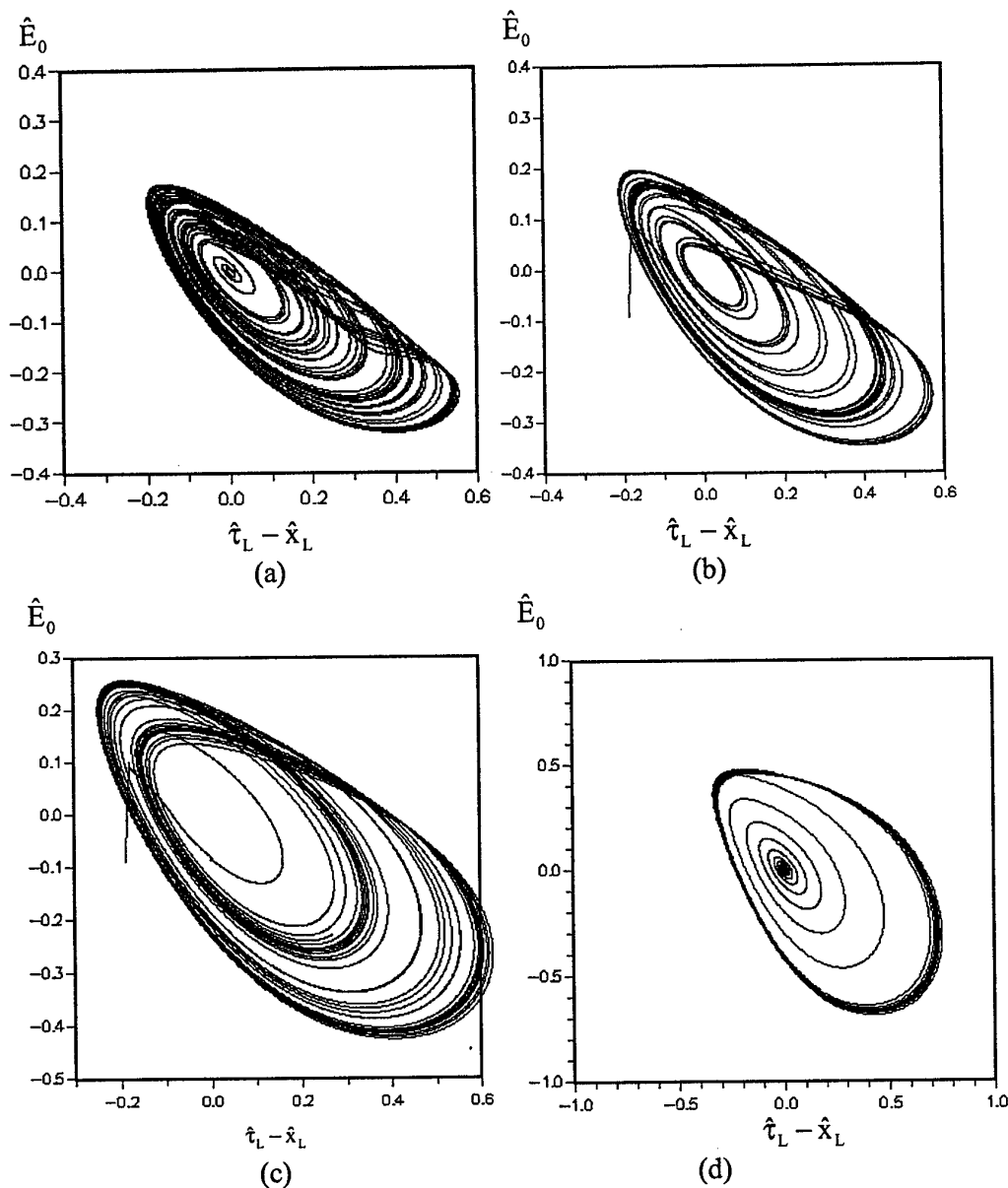


Fig. 31 Phase-space trajectories: $\hat{\alpha} = 1$, $\hat{x}_L = 2.85\pi$;
 $\hat{C} = 10^6$, (b) $\hat{C} = 175$, (c) $\hat{C} = 55$ and (d) $\hat{C} = 20$.

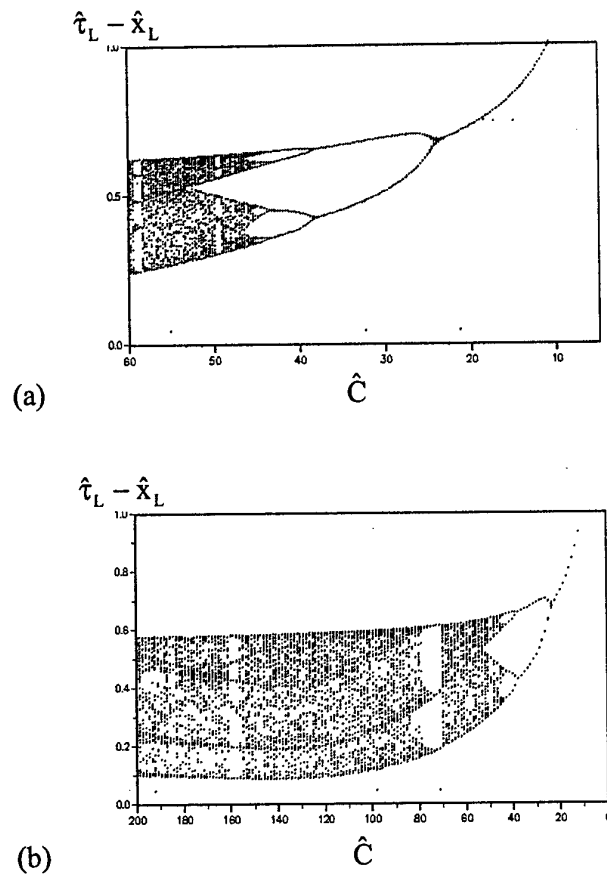


Fig.32 Bifurcation diagrams: $\hat{\alpha} = 1$, $\hat{x}_L = 2.85\pi$;

(a) $\hat{C} = 60-10$ and (b) $\hat{C} = 200-10$.

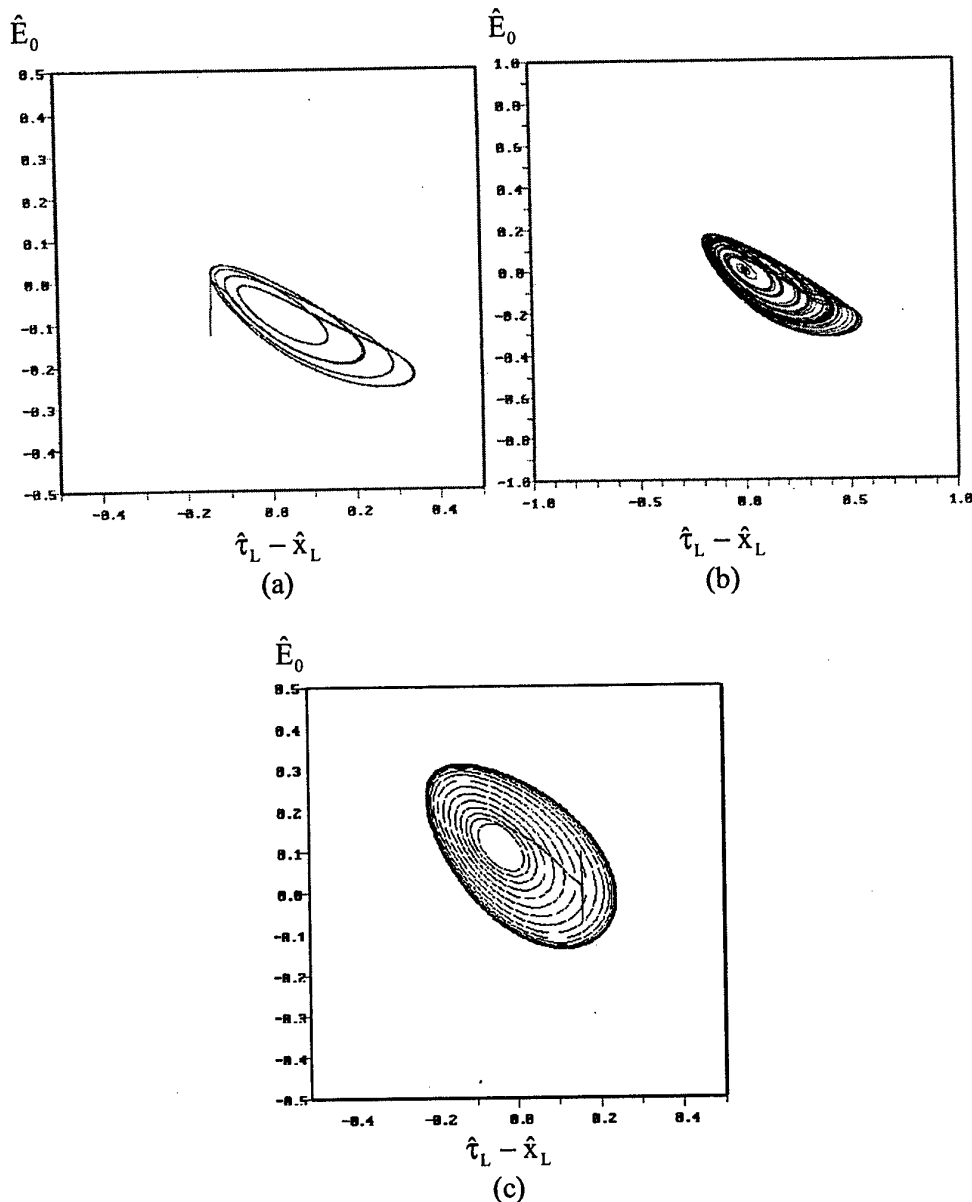


Fig. 33. Phase-space trajectories: $\hat{x}_L = 2.88\pi$, $\hat{R} = 0.0$, $\hat{C} = 10^6$;
 (a) $\hat{\alpha} = 0.9855$, (b) $\hat{\alpha} = 1.0$, (c) $\hat{\alpha} = 1.02$.

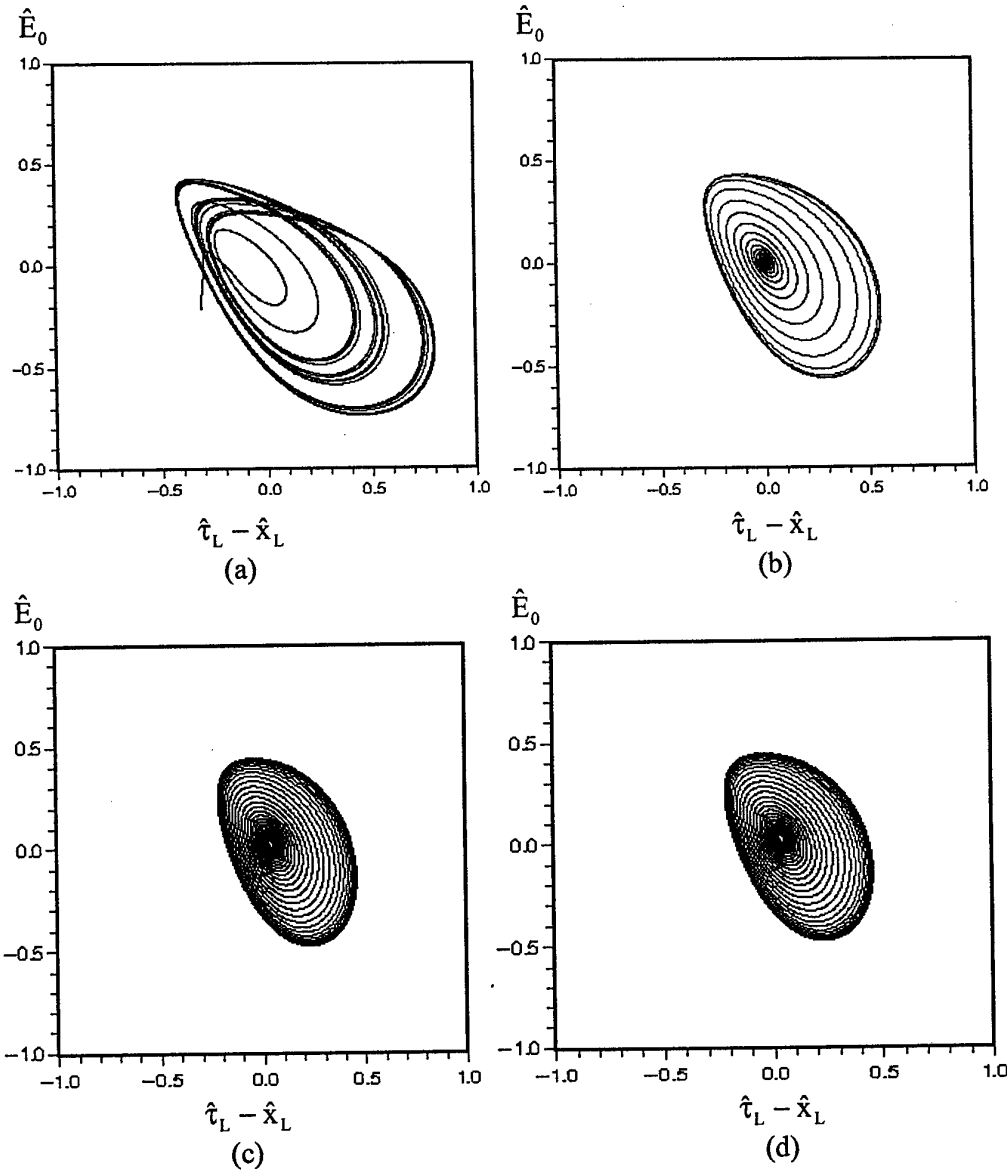


Fig. 34. Phase-space trajectories: $\hat{x}_L = 2.88\pi$, $\hat{R} = 0.0$, $\hat{C} = 20$;
 (a) $\hat{\alpha} = 0.9855$, (b) $\hat{\alpha} = 1.0$, (c) $\hat{\alpha} = 1.01$, (d) $\hat{\alpha} = 1.02$.

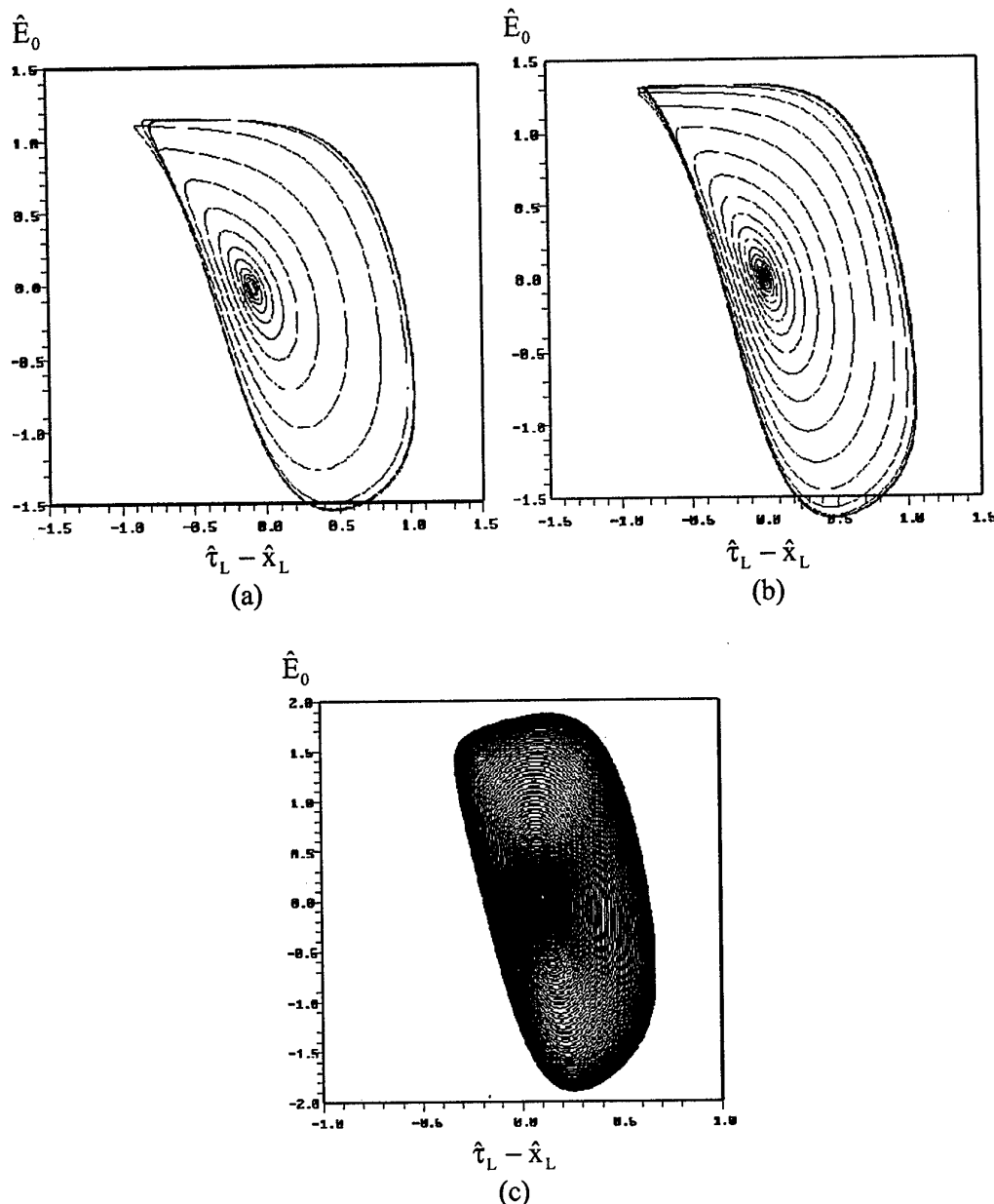


Fig. 35. Phase-space trajectories: $\hat{x}_L = 2.88\pi$, $\hat{R} = 0.0$, $\hat{C} = 10$;
 (a) $\hat{\alpha} = 0.9855$, (b) $\hat{\alpha} = 1.0$, (c) $\hat{\alpha} = 1.02$.

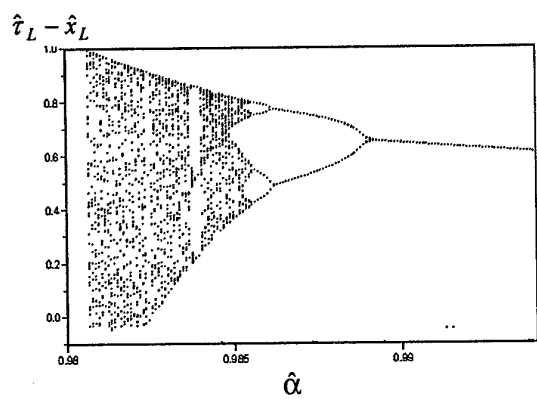


Fig.36. Bifurcation diagram for $\hat{x}_L = 2.88\pi$, $\hat{R} = 0.0$, $\hat{C} = 20$, and $\hat{\alpha} = 0.980-0.994$.

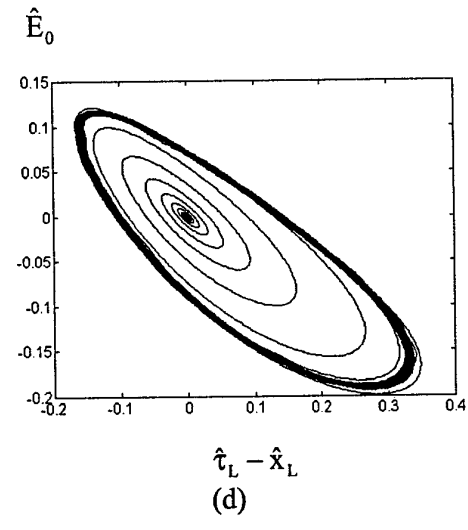
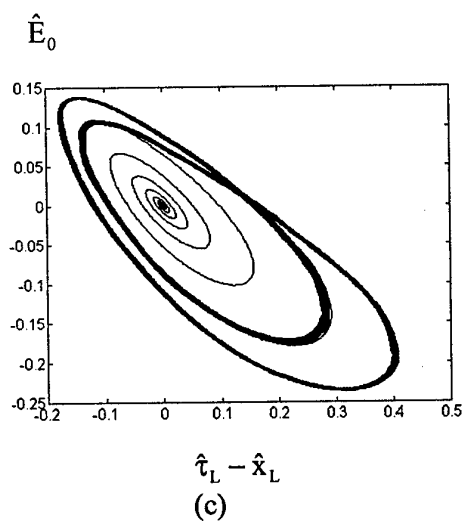
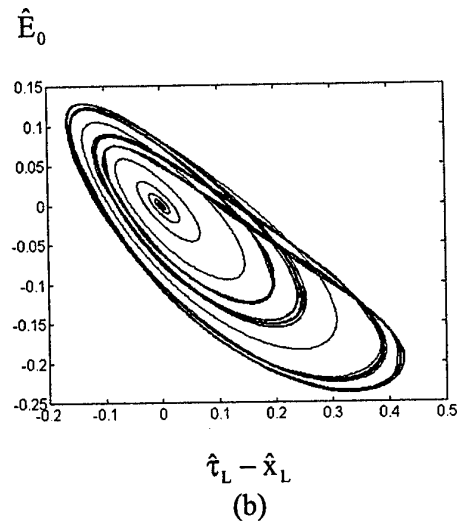
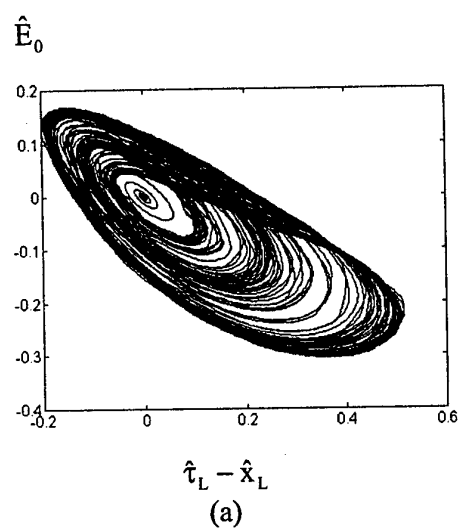
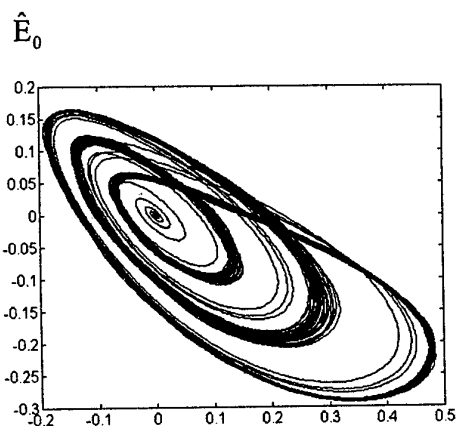
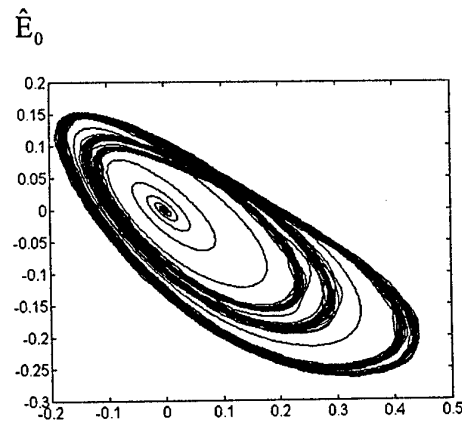


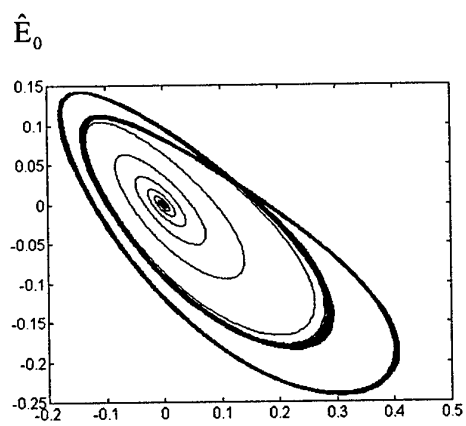
Fig. 37 Phase-space trajectories: $\hat{\alpha} = 1$, $\hat{x}_L = 2.85\pi$ and $\hat{R} = 0.0$;
 (a) $\hat{L} = 0.0$, (b) $\hat{L} = 0.3$, (c) $\hat{L} = 0.5$ and (d) $\hat{L} = 1.0$.



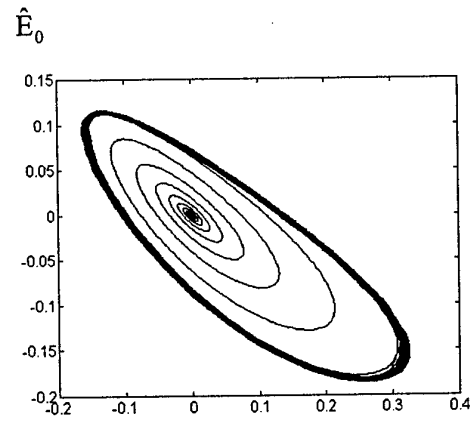
(a)
 $\hat{\tau}_L - \hat{x}_L$



(b)
 $\hat{\tau}_L - \hat{x}_L$

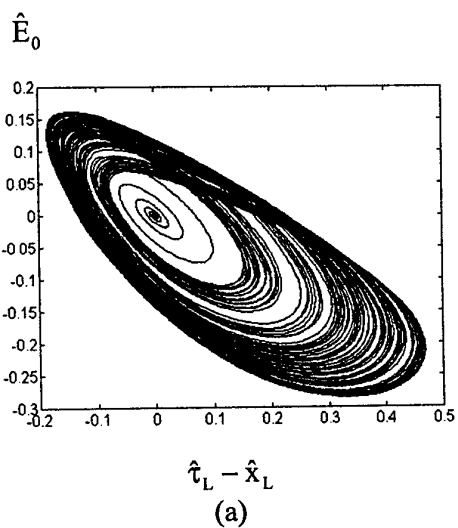


(c)
 $\hat{\tau}_L - \hat{x}_L$

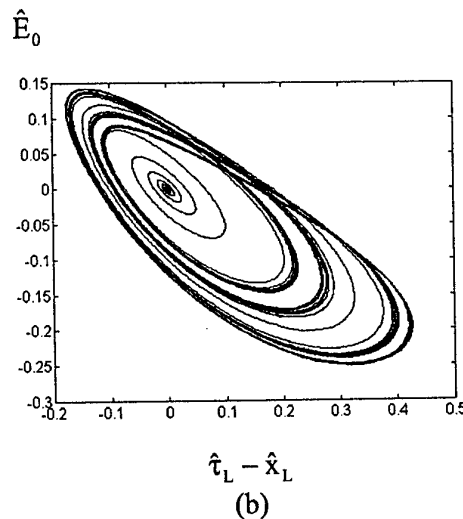


(d)
 $\hat{\tau}_L - \hat{x}_L$

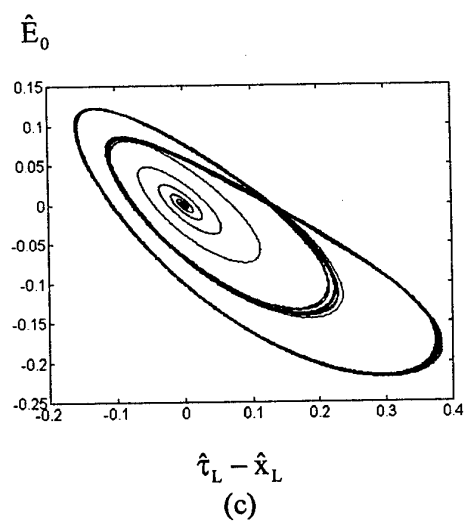
Fig. 38 Phase-space trajectories: $\hat{\alpha} = 1$, $\hat{x}_L = 2.8517\pi$ and $\hat{R} = 0.0$;
 (a) $\hat{L} = 0.0$, (b) $\hat{L} = 0.2$, (c) $\hat{L} = 0.4$ and (d) $\hat{L} = 1.0$.



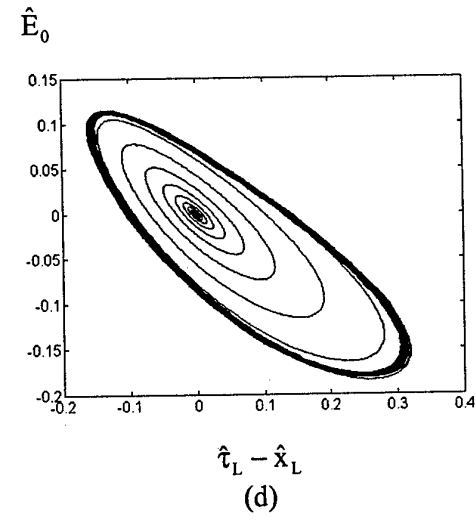
(a)



(b)



(c)



(d)

Fig. 39 Phase-space trajectories for $\hat{\alpha} = 1$, $\hat{x}_L = 2.8525\pi$ and $\hat{R} = 0.0$;
 (a) $\hat{L} = 0.0$, (b) $\hat{L} = 0.25$, (c) $\hat{L} = 0.3$ and (d) $\hat{L} = 1.0$.

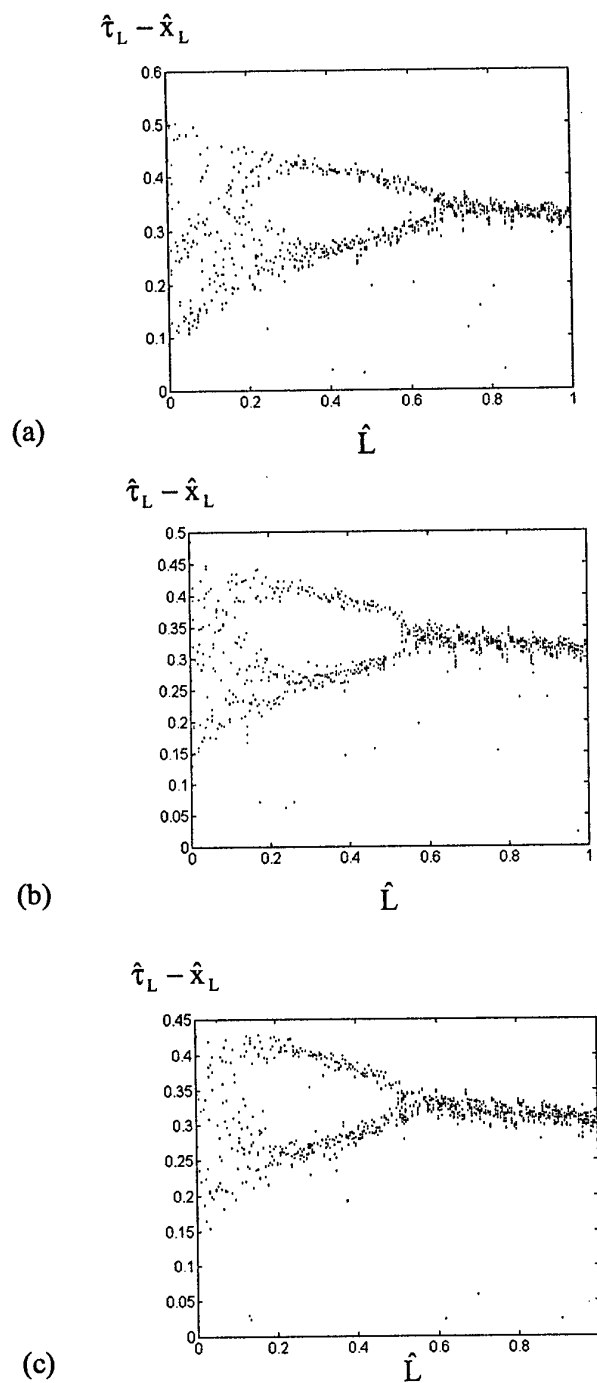


Fig.40 Bifurcation diagrams: $\hat{\alpha} = 1$ and $\hat{R} = 0.0$;
 (a) $\hat{x}_L = 2.85\pi$, (b) $\hat{x}_L = 2.8517\pi$, (c) $\hat{x}_L = 2.8525\pi$

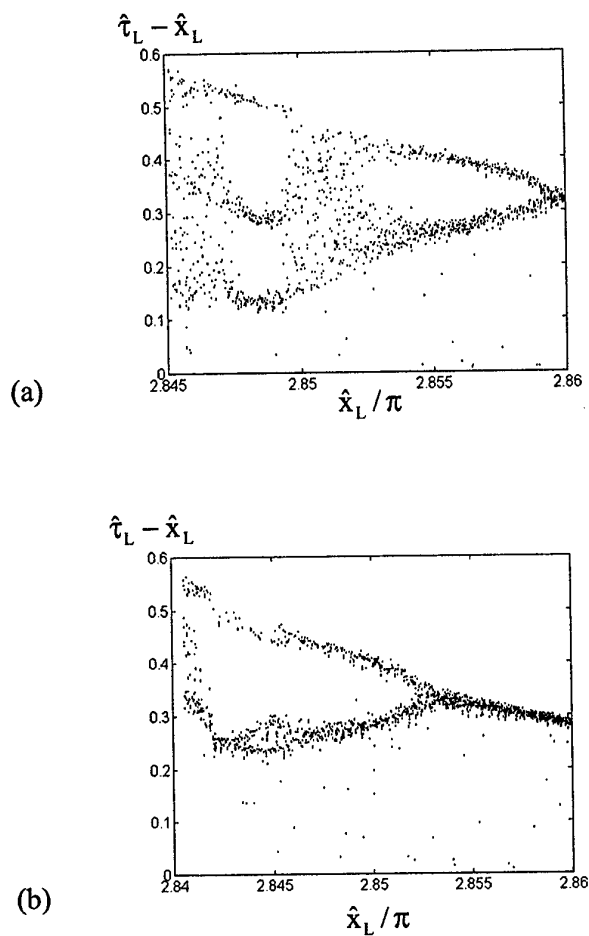


Fig.41 Bifurcation diagrams: $\hat{\alpha} = 1$ and $\hat{R} = 0.0$;
 (a) $\hat{L} = 0.1$ and (b) $\hat{L} = 0.5$

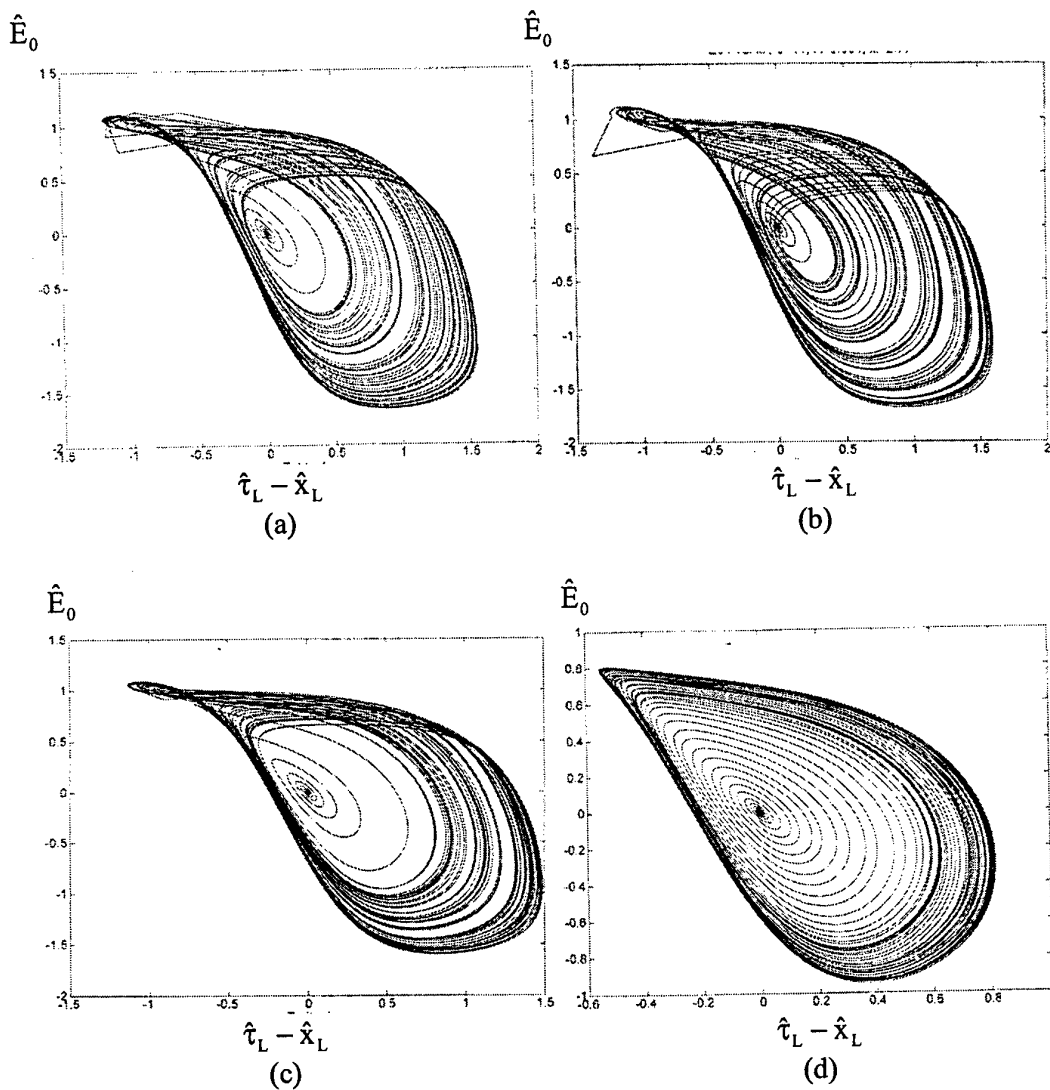
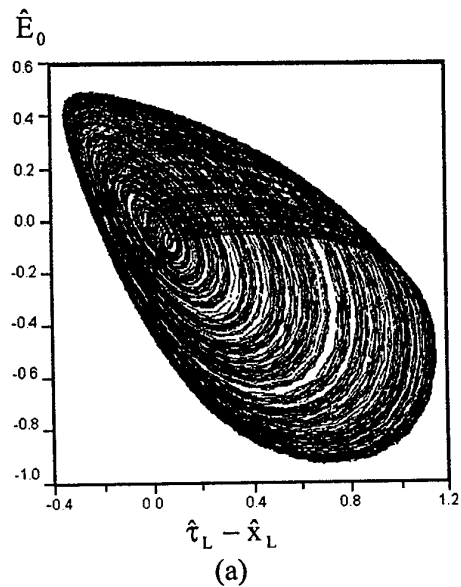
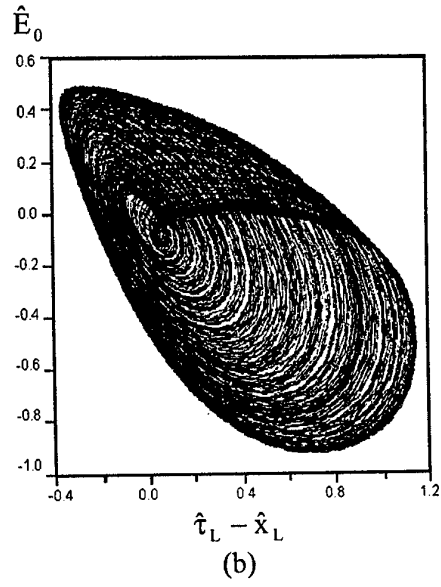


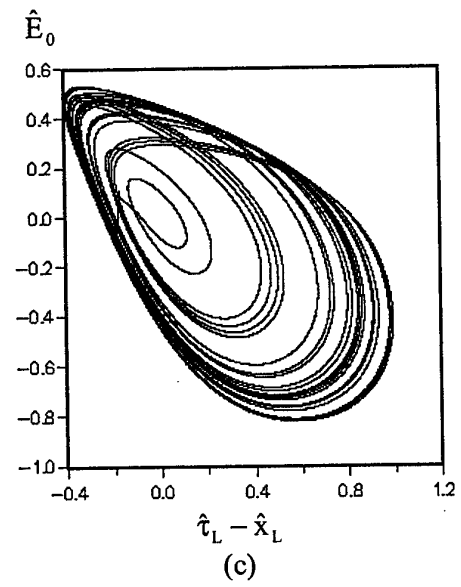
Fig. 42 Phase-space trajectories for $\hat{\alpha} = 1$, $\hat{x}_L = 2.77\pi$ and $\hat{C} = 11$;
 (a) $\hat{R} = 0.0001$, (b) $\hat{R} = 0.001$, (c) $\hat{R} = 0.01$ and (d) $\hat{R} = 0.1$.



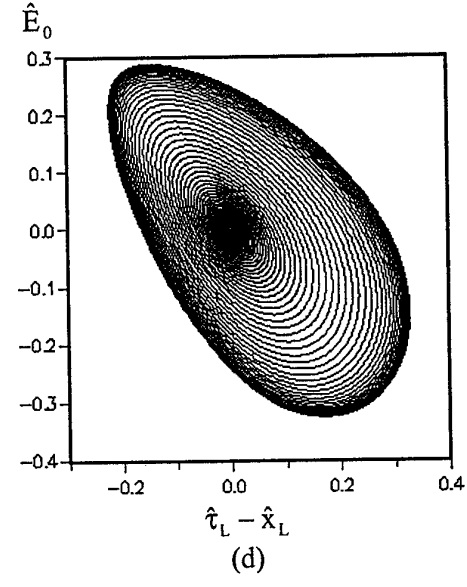
(a)



(b)

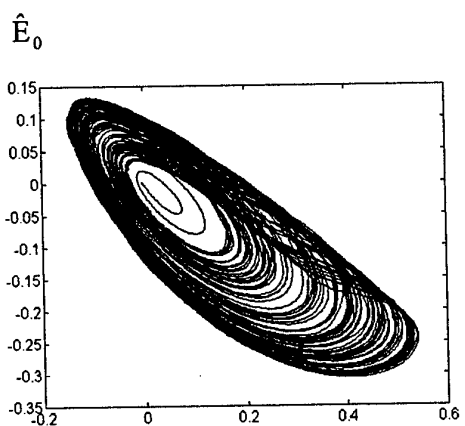


(c)

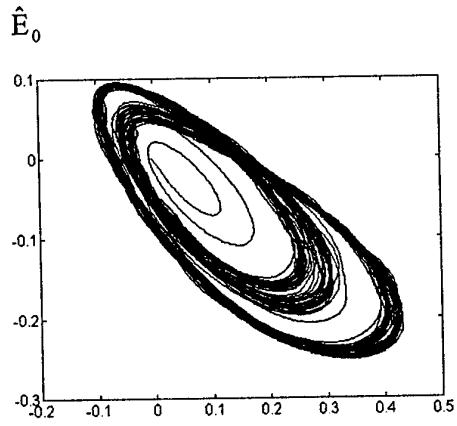


(d)

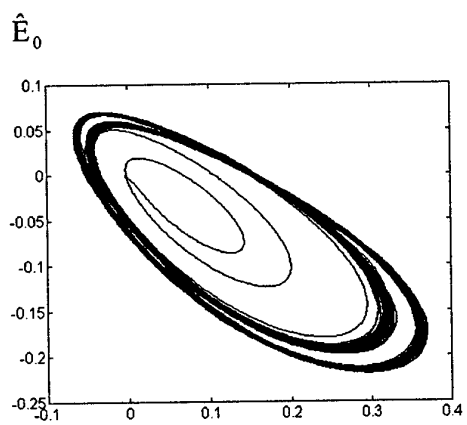
Fig. 43. Phase-space trajectories for $\hat{\alpha} = 1$, $\hat{x}_L = 2.82\pi$, $\hat{C} = 20$;
 (a) $\hat{R} = 10^{-4}$, (b) $\hat{R} = 10^{-3}$, (c) $\hat{R} = 0.01$ and (d) $\hat{R} = 0.1$



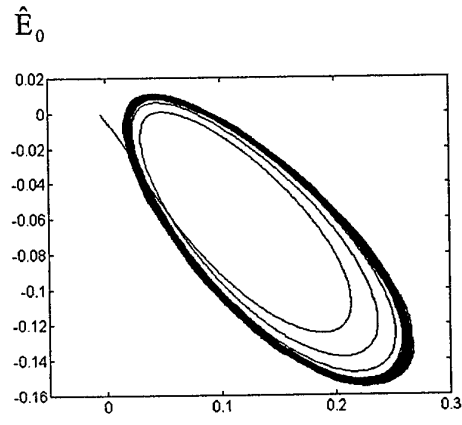
(a)



(b)

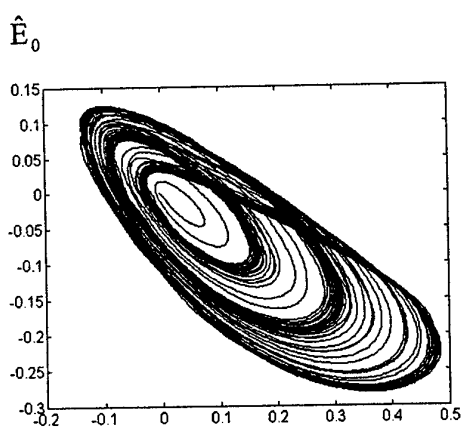


(c)

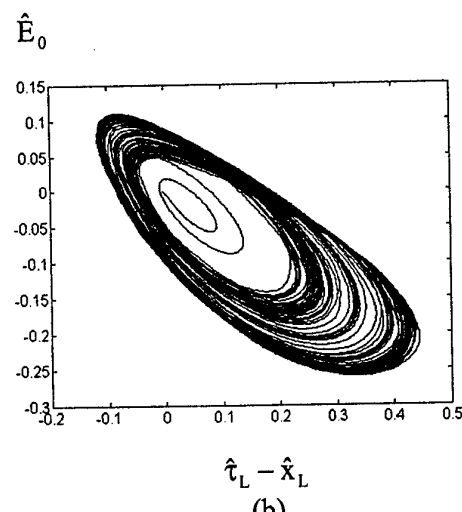


(d)

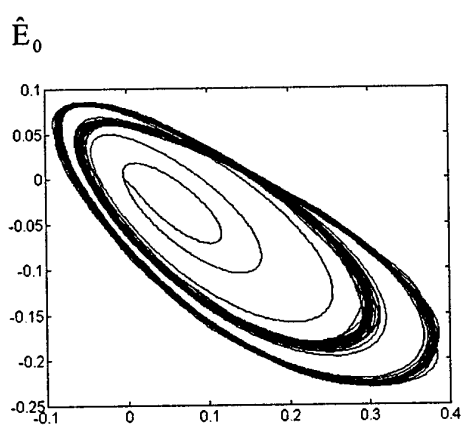
Fig. 44 Phase-space trajectories: $\hat{\alpha} = 1$, $\hat{x}_L = 2.37\pi$ and $\hat{L} = 0.0$:
 (a) $\hat{R} = 0.001$, (b) $\hat{R} = 0.0015$, (c) $\hat{R} = 0.0018$ and (d) $\hat{R} = 0.0025$.



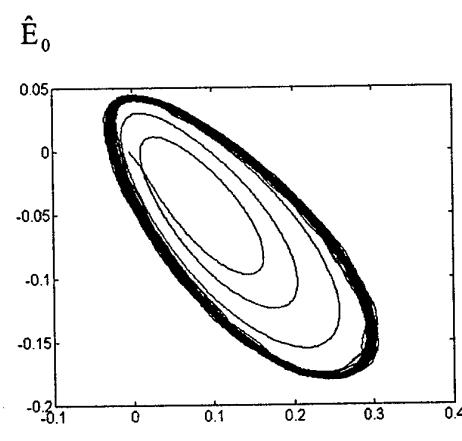
(a)



(b)



(c)



(d)

Fig. 45 Phase-space trajectories: $\hat{\alpha} = 1$, $\hat{L} = 0.0$ and $\hat{x}_L = 2.84\pi$:
 (a) $\hat{R} = 0.001$, (b) $\hat{R} = 0.0011$, (c) $\hat{R} = 0.0015$ and (d) $\hat{R} = 0.002$

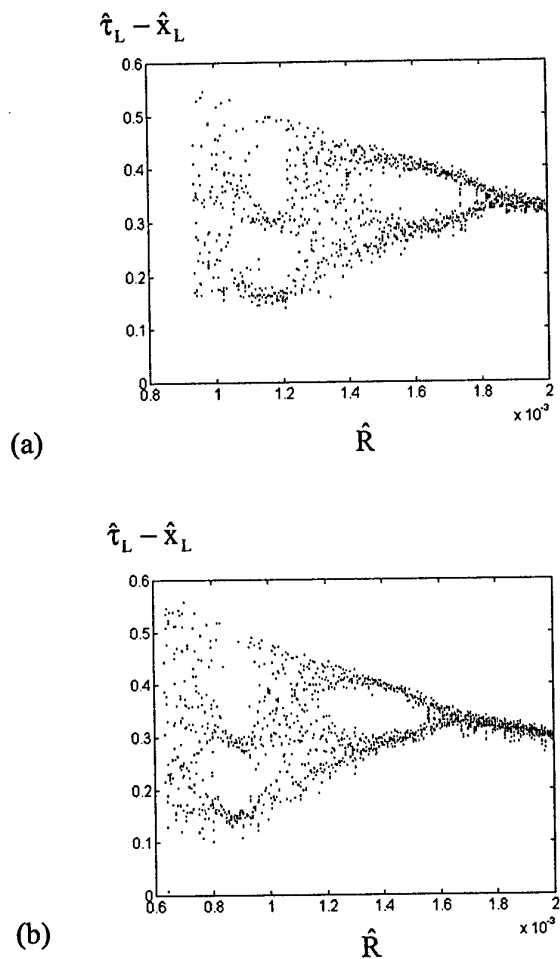
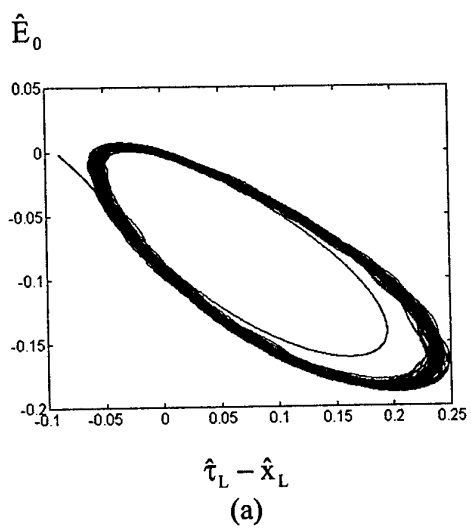
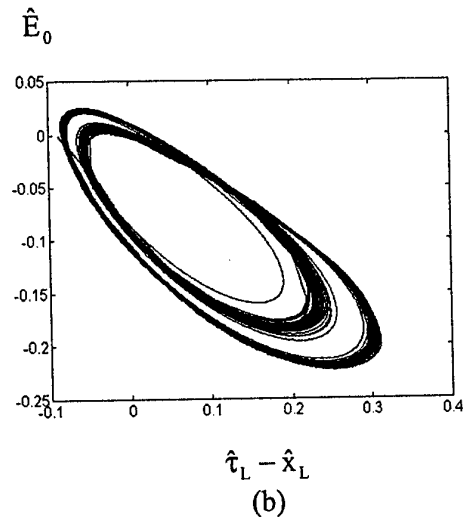


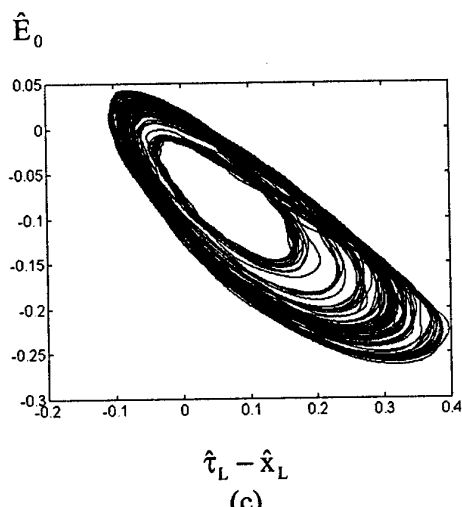
Fig.46 Bifurcation diagrams: $\hat{\alpha} = 1.0$ and $\hat{L} = 0.0$:
 (a) $\hat{x}_L = 2.837\pi$ and (b) $\hat{x}_L = 2.84\pi$



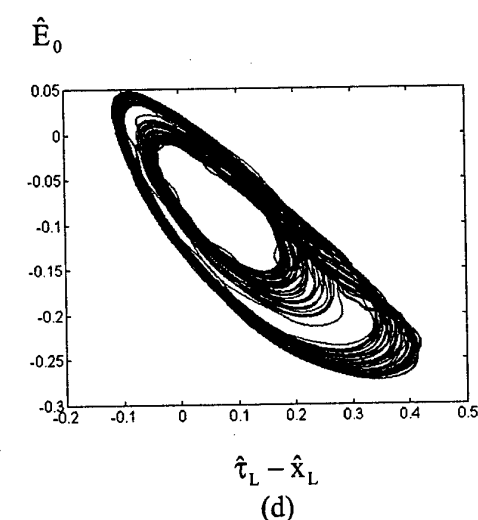
(a)



(b)



(c)



(d)

Fig. 47 Phase-space trajectories: $\hat{\alpha} = 0.99$, $\hat{R} = 0.001$ and $\hat{L} = 0.0$;
 (a) $\hat{x}_L = 2.865\pi$, (b) $\hat{x}_L = 2.861\pi$, (c) $\hat{x}_L = 2.857\pi$ and (d) $\hat{x}_L = 2.856\pi$

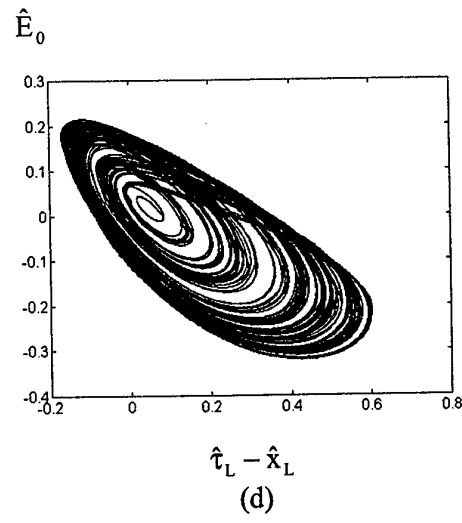
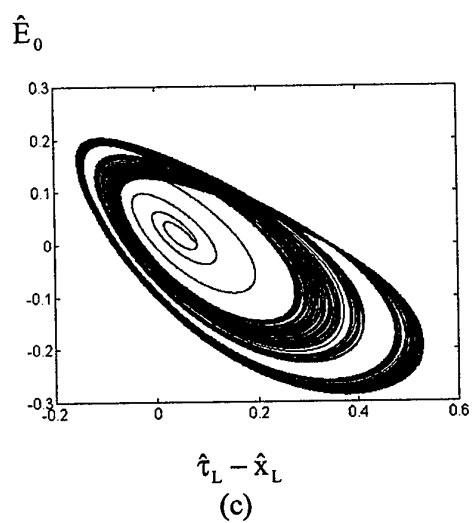
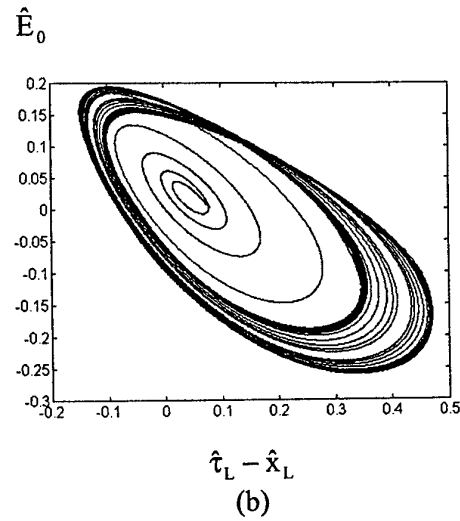
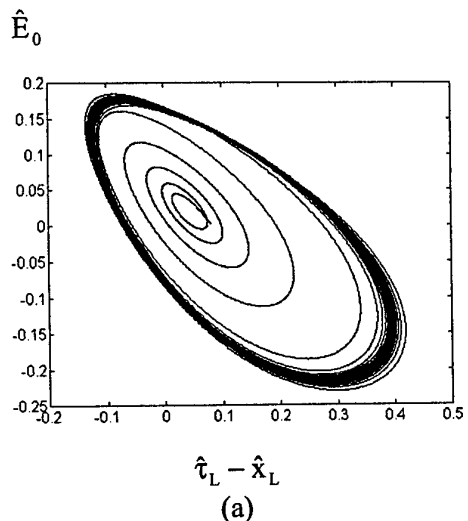


Fig. 48 Phase-space trajectories: $\hat{\alpha} = 1.01$, $\hat{R} = 0.001$ and $\hat{L} = 0.0$;
 (a) $\hat{x}_L = 2.835\pi$, (b) $\hat{x}_L = 2.83\pi$, (c) $\hat{x}_L = 2.825\pi$ and (d) $\hat{x}_L = 2.82\pi$

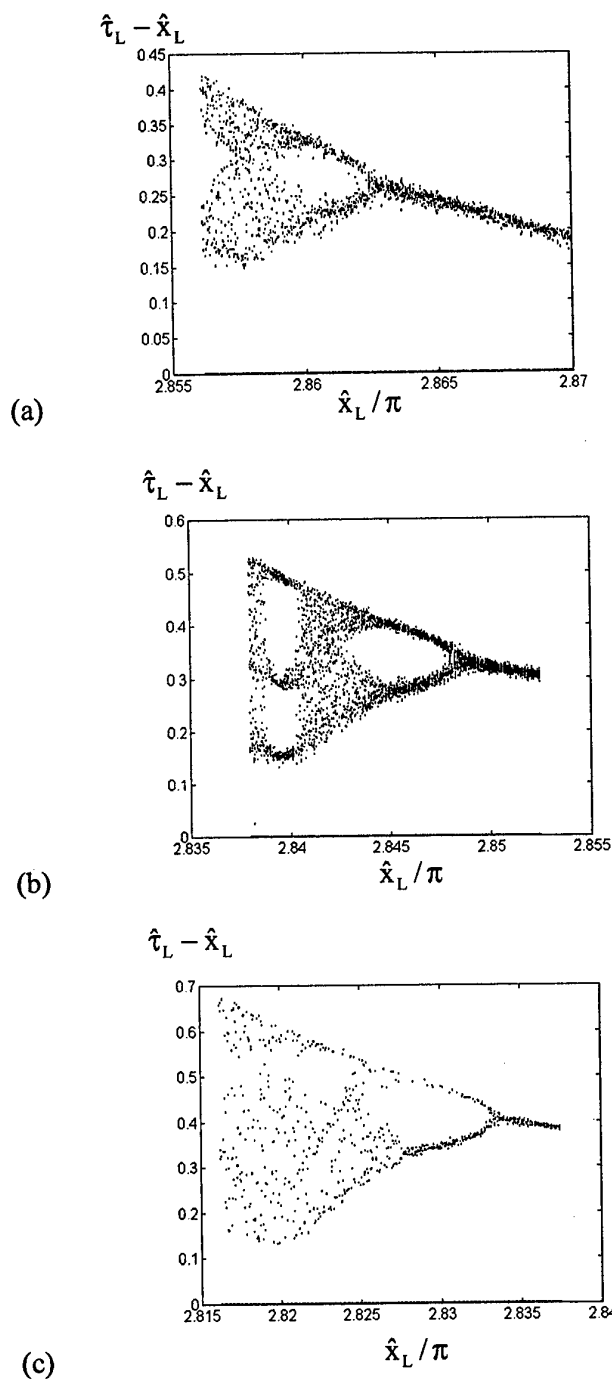


Fig.49 Bifurcation diagrams: $\hat{R} = 0.001$ and $\hat{L} = 0.0$;
 (a) $\hat{\alpha} = 0.99$, (b) $\hat{\alpha} = 1.00$ and (c) $\hat{\alpha} = 1.01$

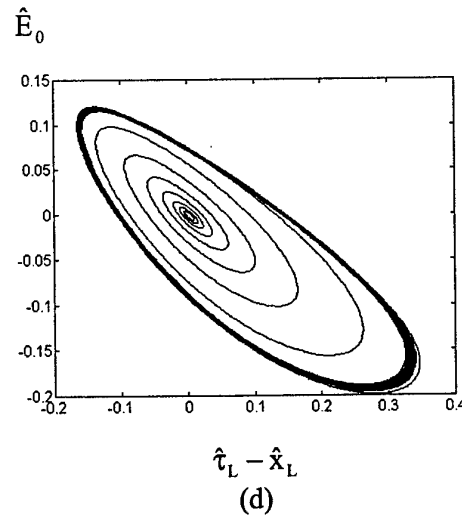
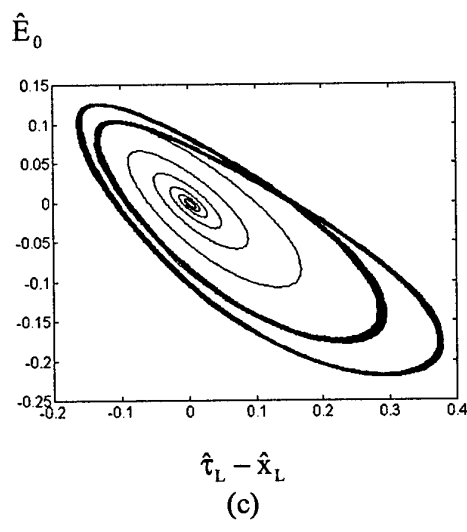
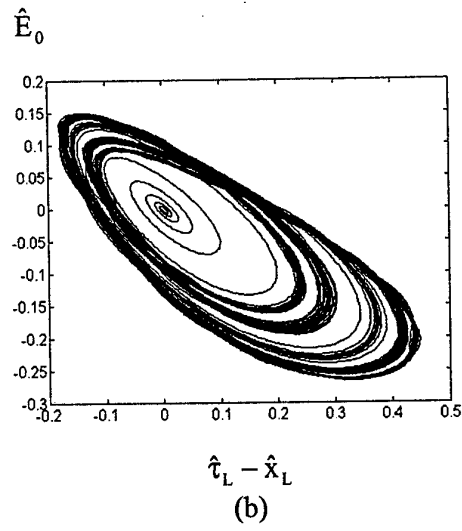
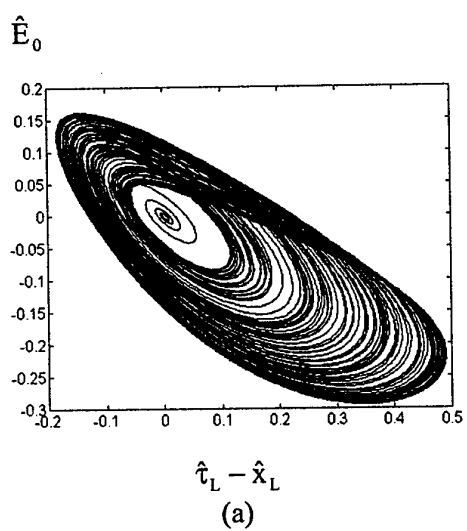
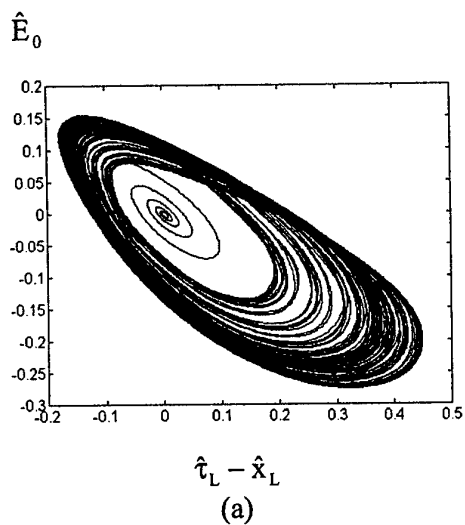
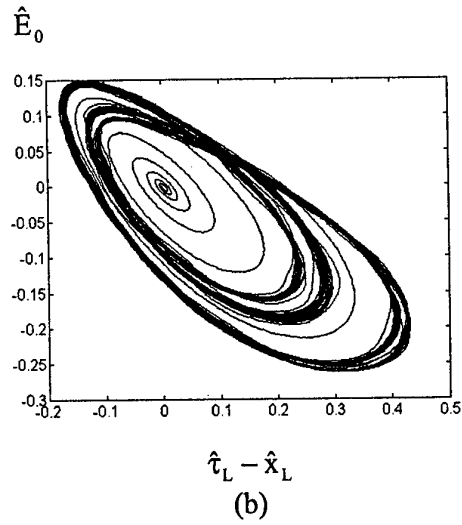


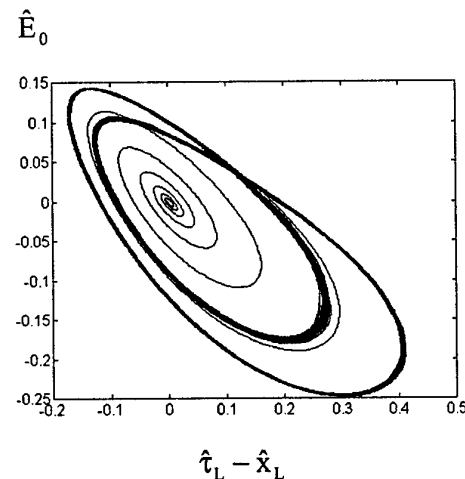
Fig 50 Phase-space trajectories: $\hat{\alpha} = 1$, $\hat{x}_L = 2.85\pi$ and $\hat{R} = 0.0001$:
 (a) $\hat{L} = 0.0$, (b) $\hat{L} = 0.2$, (c) $\hat{L} = 0.5$ and (d) $\hat{L} = 1.0$



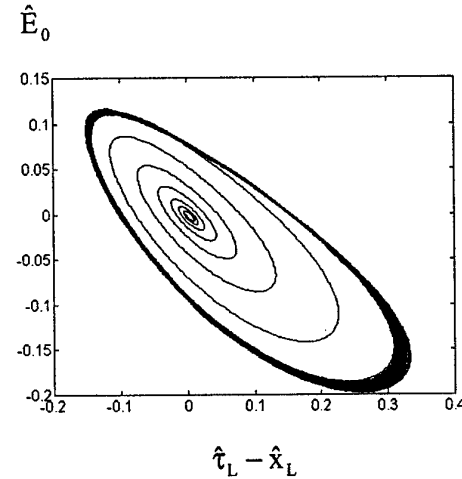
(a)



(b)



(c)



(d)

Fig 51 Phase-space trajectories: $\hat{\alpha} = 1$, $\hat{x}_L = 2.8525\pi$ and $\hat{R} = 0.0001$:

(a) $\hat{L} = 0.0$, (b) $\hat{L} = 0.1$, (c) $\hat{L} = 0.2$ and (d) $\hat{L} = 0.5$

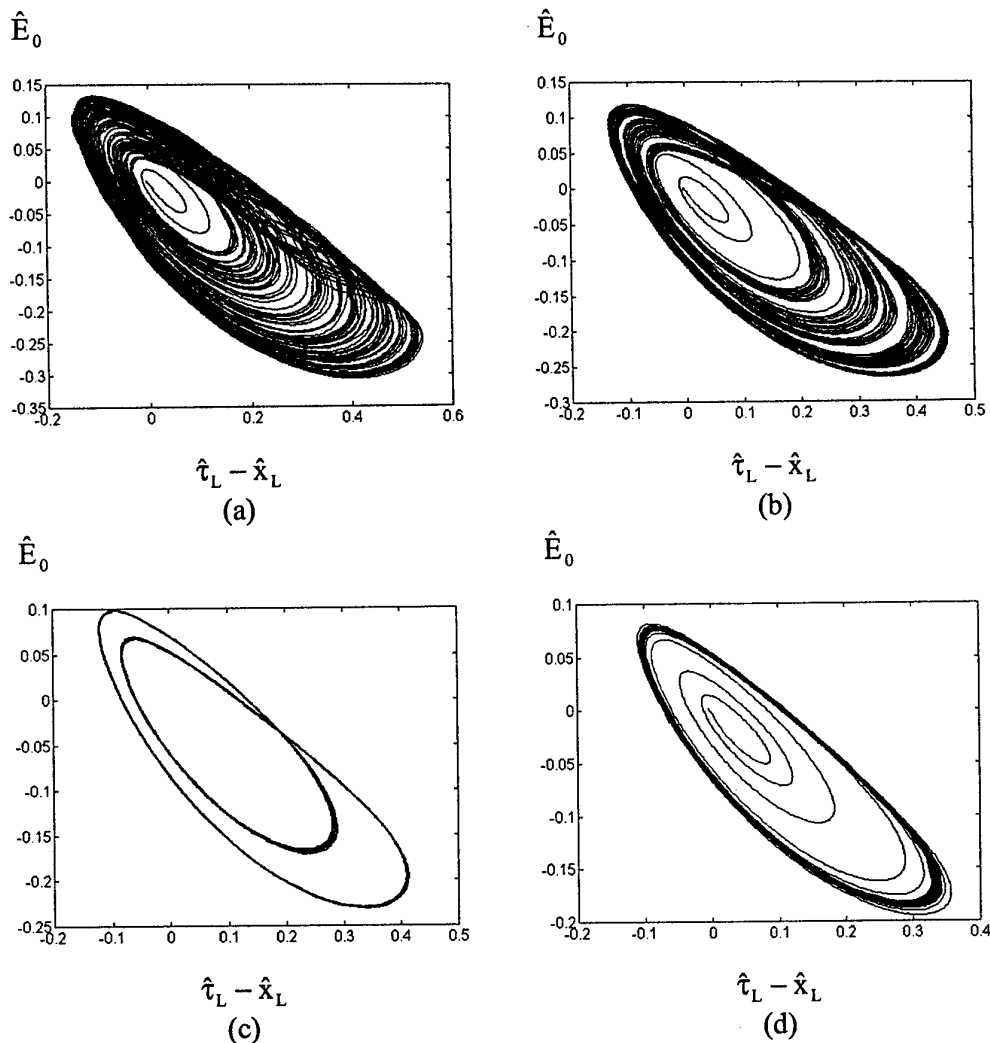


Fig 52 Phase-space trajectories: $\hat{\alpha} = 1$, $\hat{x}_L = 2.837\pi$ and $\hat{R} = 0.001$;
 (a) $\hat{L} = 0.0$, (b) $\hat{L} = 0.1$, (c) $\hat{L} = 0.5$ and (d) $\hat{L} = 1.0$

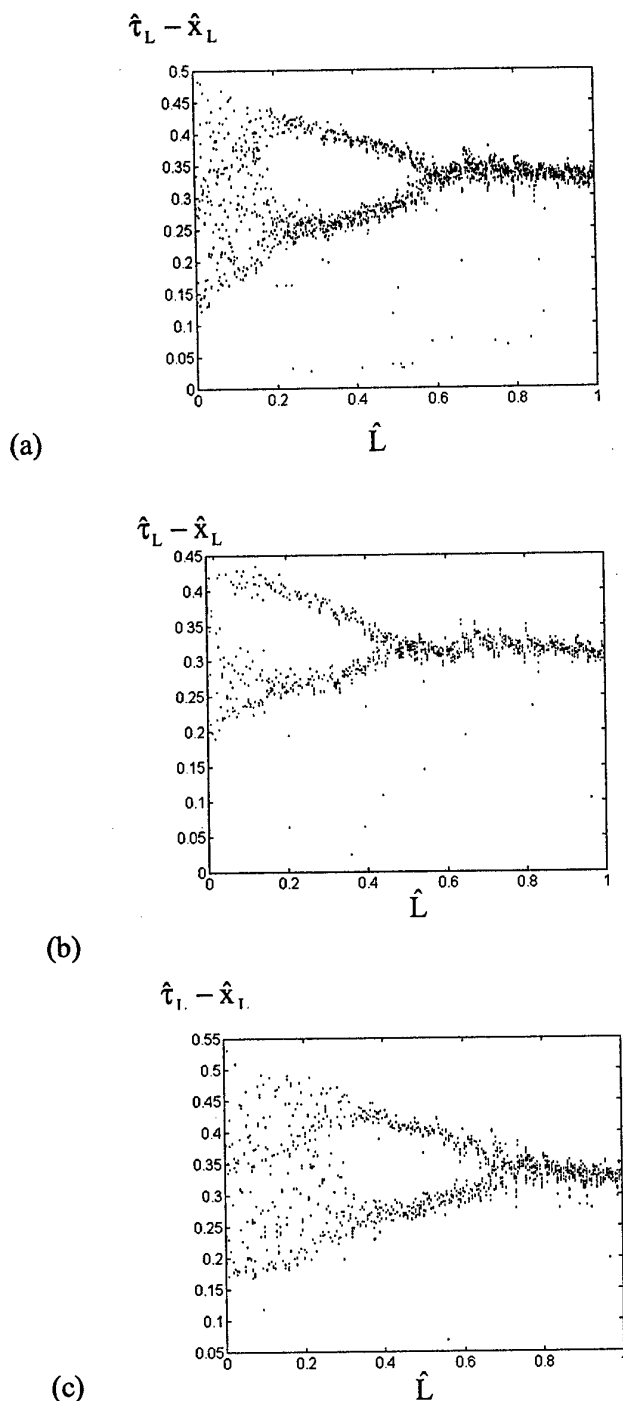


Fig. 53 Bifurcation diagrams: $\hat{\alpha} = 1$:

- (a) $\hat{x}_L = 2.85\pi$ and $\hat{R} = 0.0001$
- (b) $\hat{x}_L = 2.8525\pi$ and $\hat{R} = 0.0001$
- (c) $\hat{x}_L = 2.837\pi$ and $\hat{R} = 0.001$.

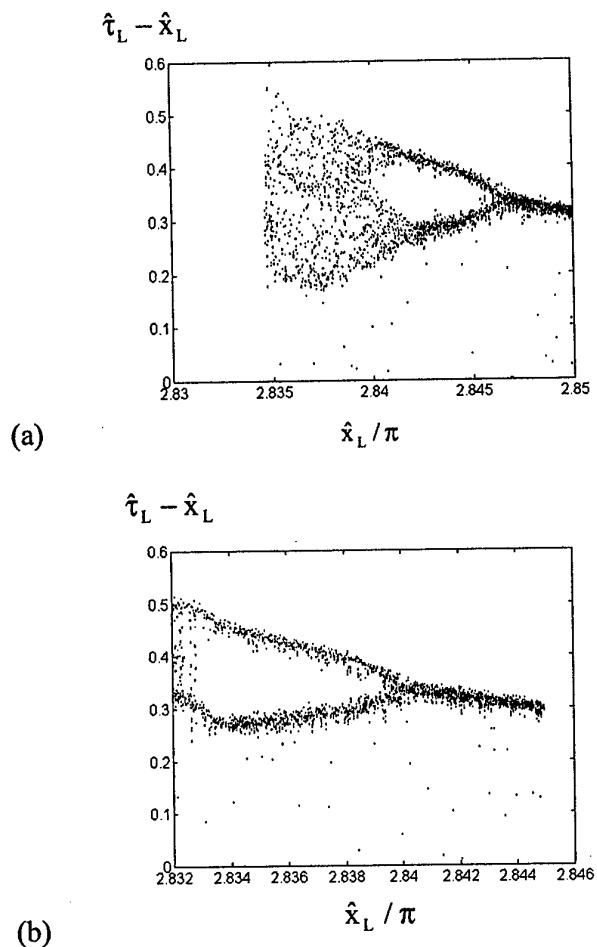


Fig. 54 Bifurcation diagrams: $\hat{\alpha} = 1$ and $\hat{R} = 0.001$
 (a) $\hat{L} = 0.1$ and (b) $\hat{L} = 0.5$

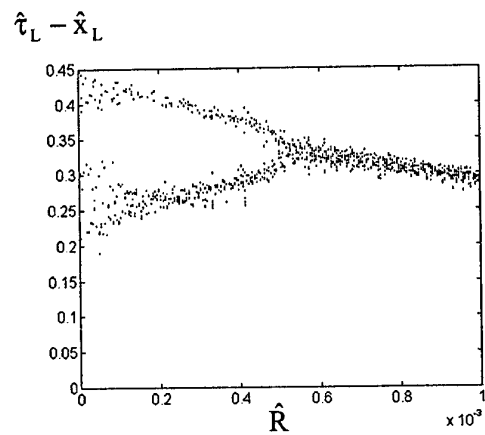


Fig. 55 Bifurcation diagram: $\hat{\alpha} = 1$, $\hat{x}_L = 2.8525\pi$ and $\hat{L} = 0.1$.

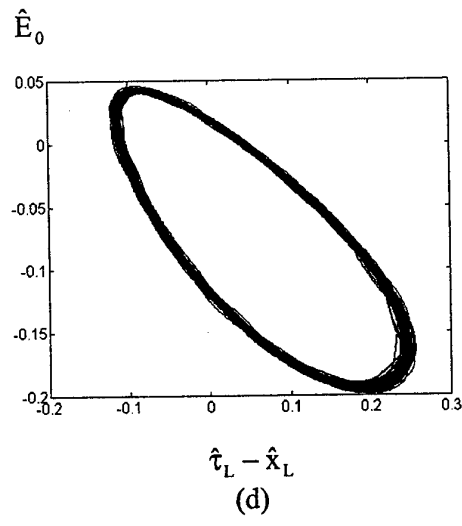
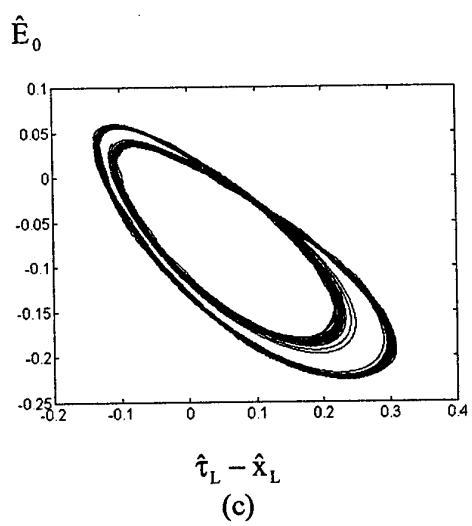
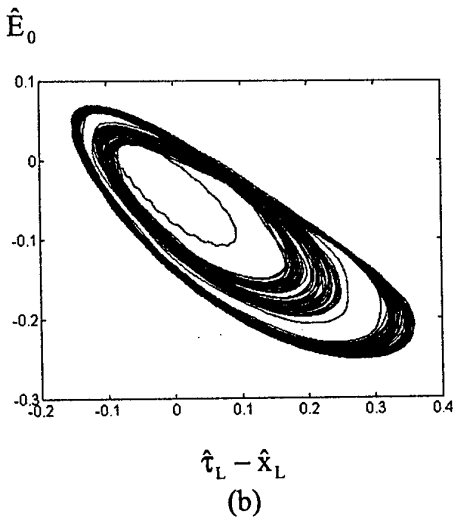
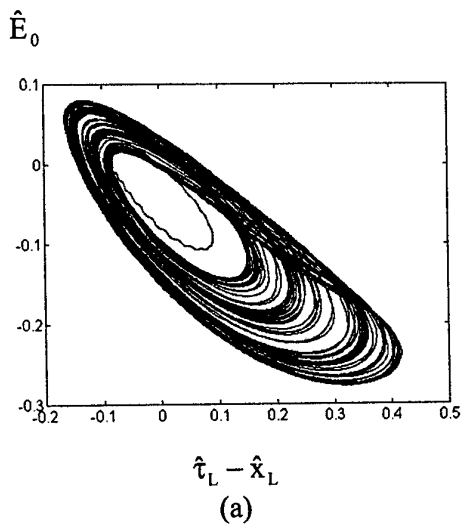
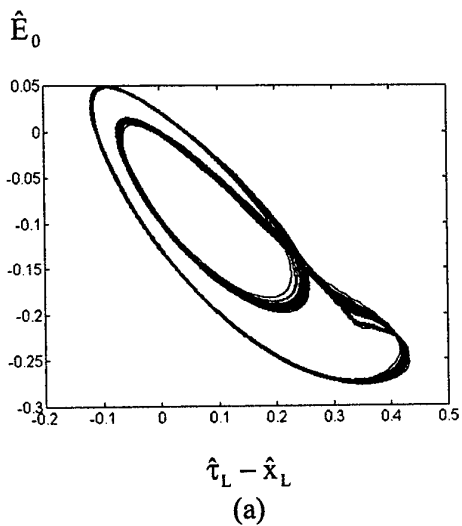
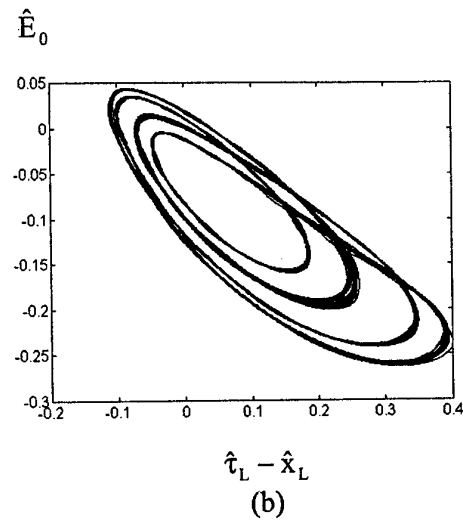


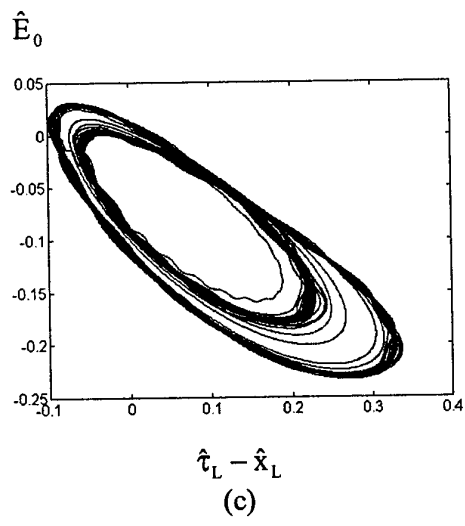
Fig. 56 Phase-space trajectories: $\hat{\alpha} = 0.99$, $\hat{R} = 0.0001$ and $\hat{L} = 0.1$;
 (a) $\hat{x}_L = 2.866\pi$, (b) $\hat{x}_L = 2.869\pi$, (c) $\hat{x}_L = 2.872\pi$ and (d) $\hat{x}_L = 2.875\pi$



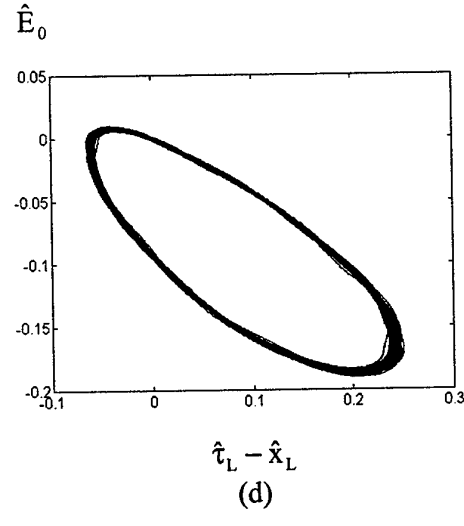
(a)



(b)



(c)



(d)

Fig. 57 Phase-space trajectories: $\hat{\alpha} = 0.99$, $\hat{R} = 0.001$ and $\hat{L} = 0.1$;
 (a) $\hat{x}_L = 2.85468\pi$, (b) $\hat{x}_L = 2.856\pi$, (c) $\hat{x}_L = 2.859\pi$ and (d) $\hat{x}_L = 2.864\pi$

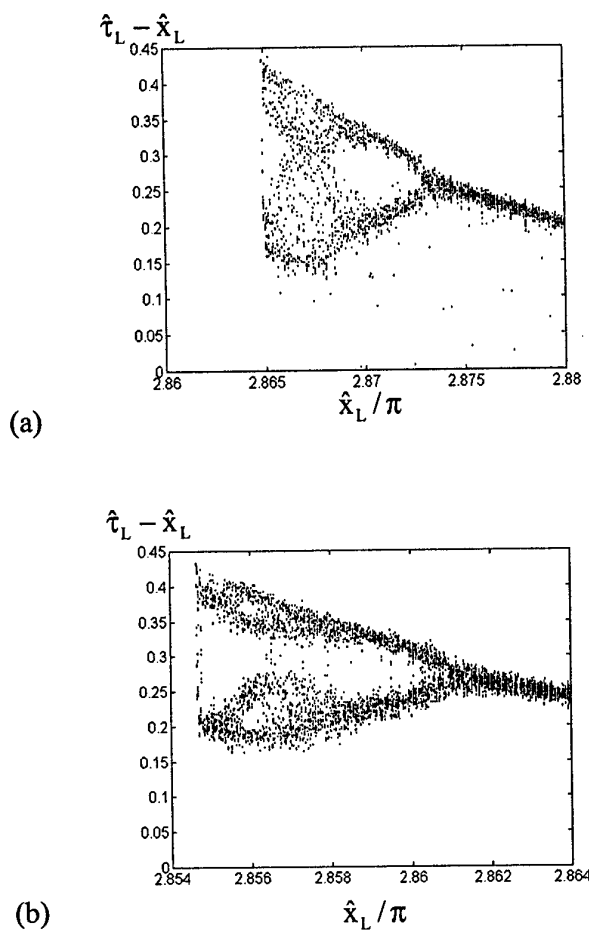


Fig. 58 Bifurcation diagrams: $\hat{\alpha} = 0.99$ and $\hat{L} = 0.1$;
 (a) $\hat{R} = 0.0001$ and (b) $\hat{R} = 0.001$

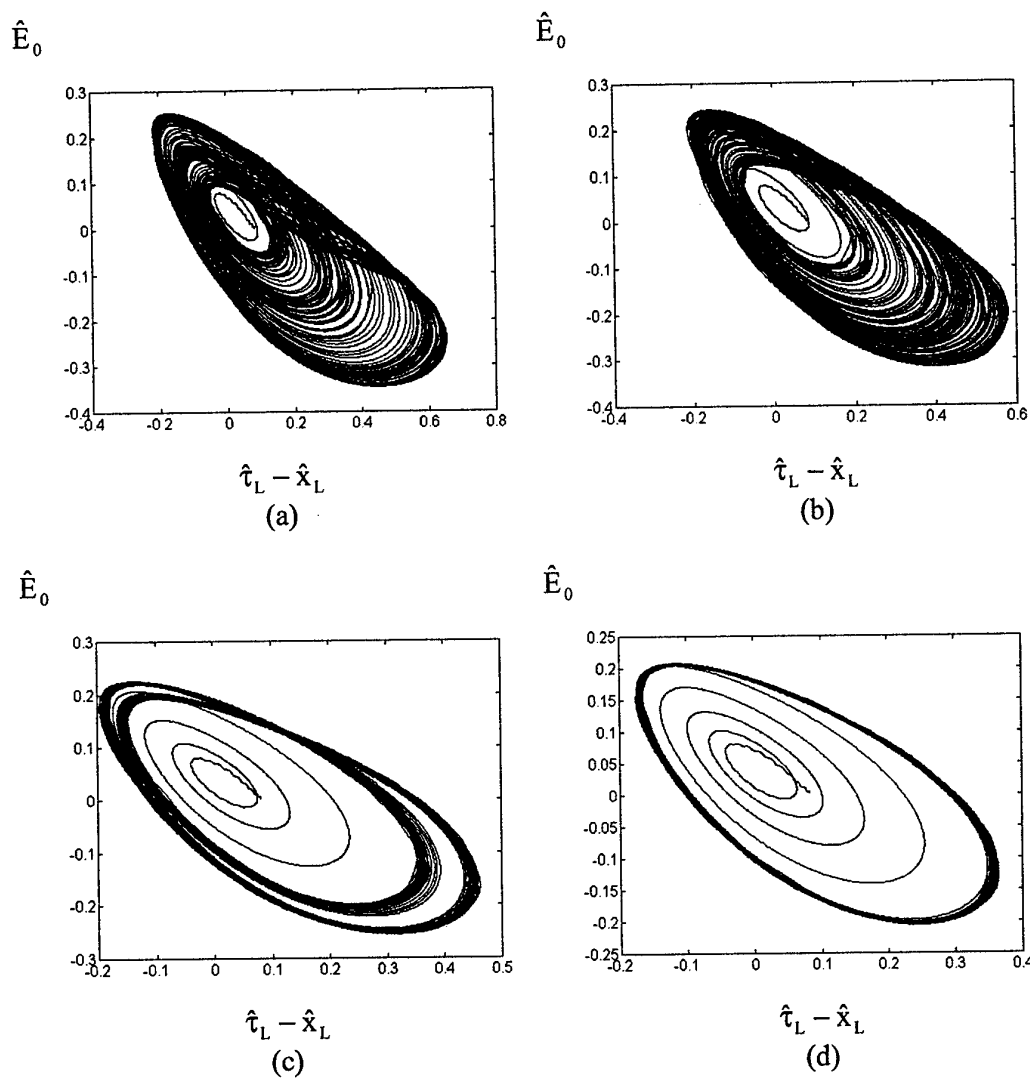


Fig. 59 Phase-space trajectories: $\hat{\alpha} = 1.01$, $\hat{R} = 0.0001$ and $\hat{L} = 0.1$;
 (a) $\hat{x}_L = 2.825\pi$, (b) $\hat{x}_L = 2.83\pi$, (c) $\hat{x}_L = 2.84\pi$ and $\hat{x}_L = 2.85\pi$.

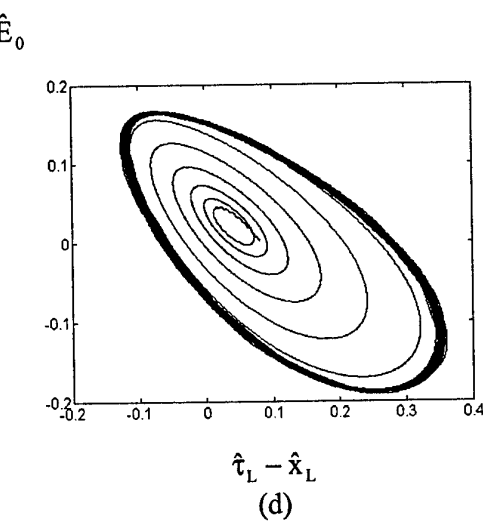
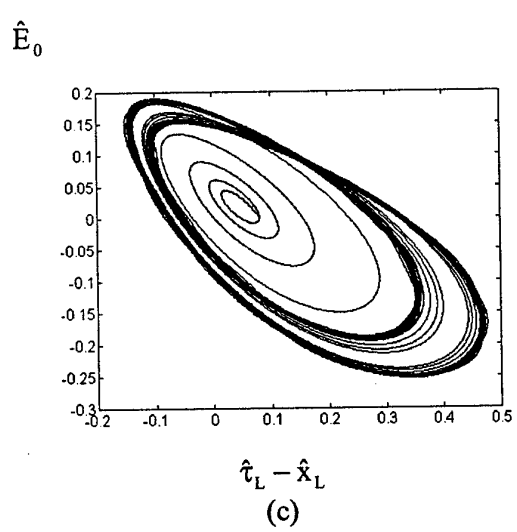
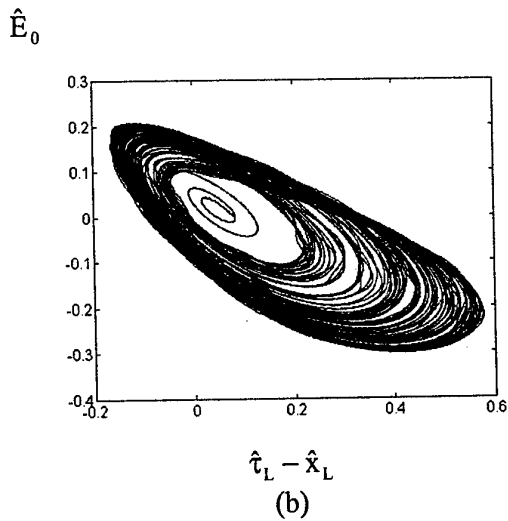
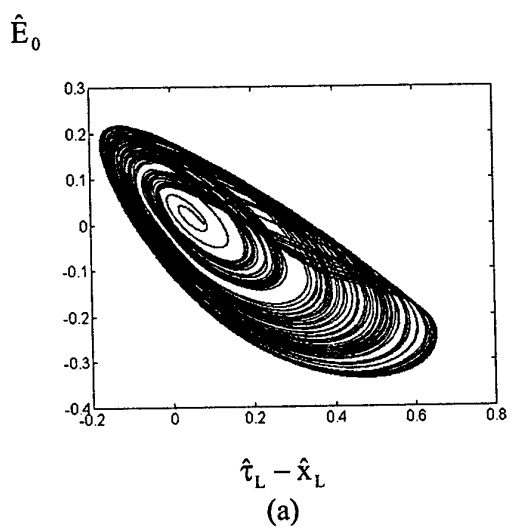


Fig. 60 Phase-space trajectories: $\hat{\alpha} = 1.01$, $\hat{R} = 0.001$ and $\hat{L} = 0.1$;
(a) $\hat{x}_L = 2.815\pi$, (b) $\hat{x}_L = 2.82\pi$, (c) $\hat{x}_L = 2.828\pi$ and (d) $\hat{x}_L = 2.84\pi$.

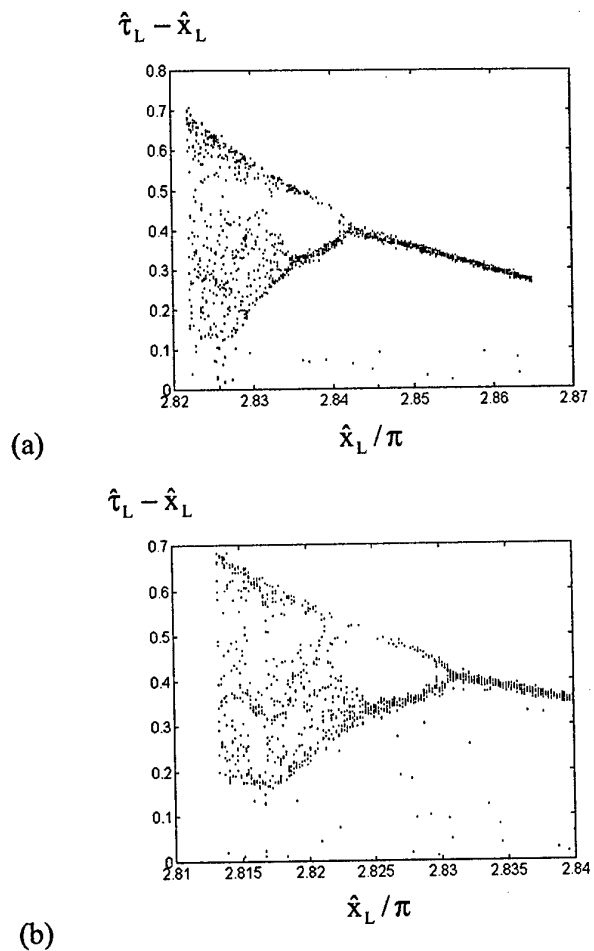


Fig. 61 Bifurcation diagrams: $\hat{\alpha} = 1.01$ and $\hat{L} = 0.1$;
 (a) $\hat{R} = 0.0001$ and (b) $\hat{R} = 0.001$

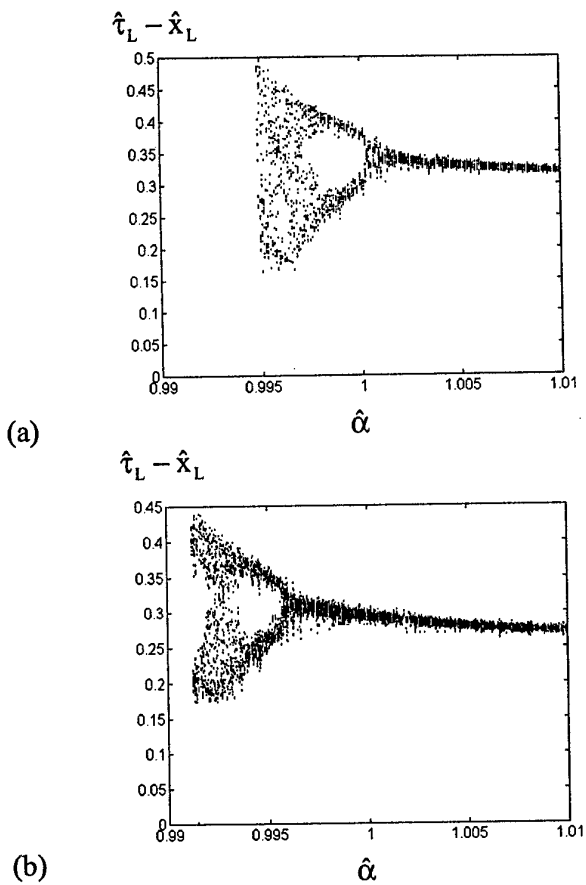


Fig. 62 Bifurcation diagrtams: $\hat{R} = 0.001$ and $\hat{L} = 0.1$;
 (a) $\hat{x}_L = 2.84\pi$ and (b) $\hat{x}_L = 2.852\pi$.

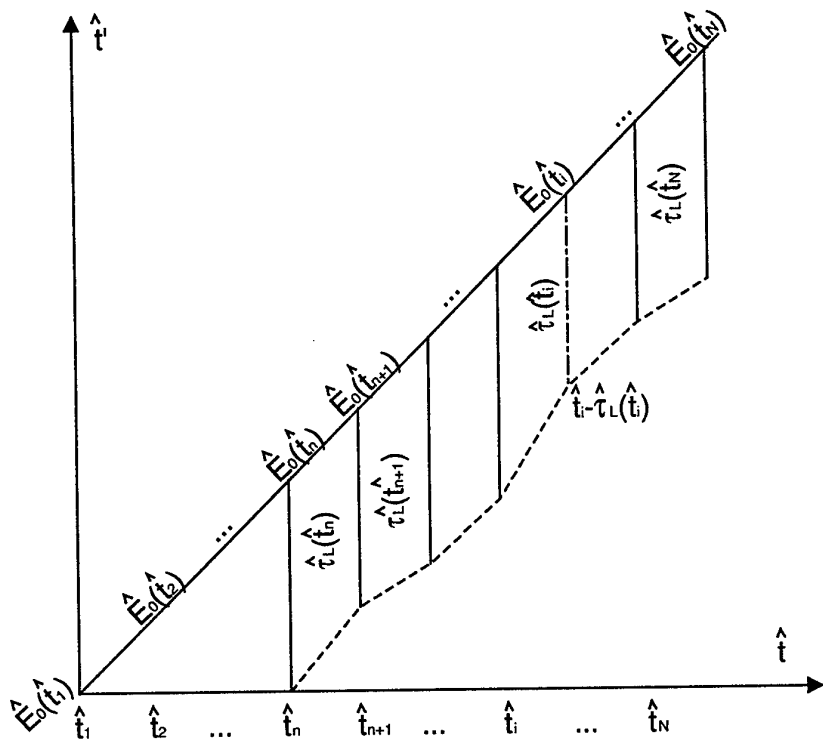
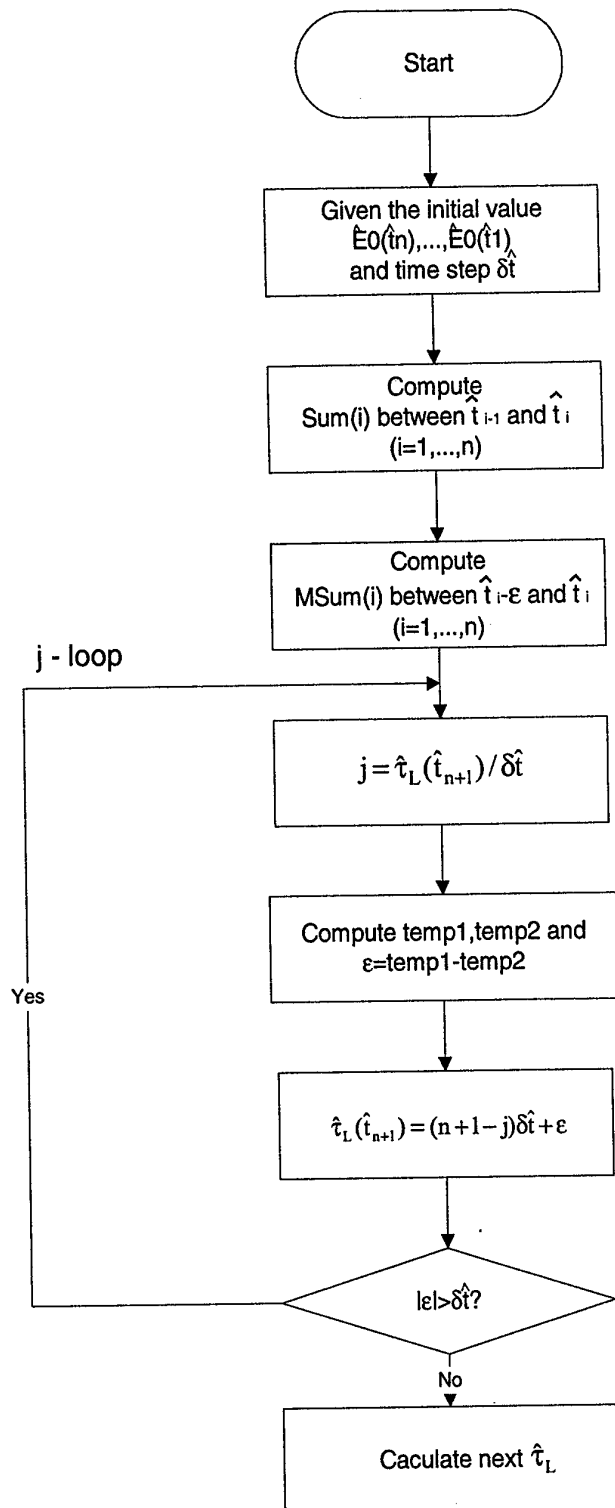


Fig. A2.1 Diagram of the numerical procedure used in solving (3.14), (3.18)



$$\hat{\text{Sum}}(i) = \frac{\delta t}{2} [k(\hat{t}_{i-1}) + k(\hat{t}_i)]$$

$$\hat{M\text{Sum}}(i) \approx \frac{1}{2} \frac{\delta t}{2} \left[\frac{k(\hat{t}_{i-1}) + k(\hat{t}_i)}{2} + k(\hat{t}_i) \right]$$

temp1=RHS of (A2.5)
 where $F_2 = \sum_{i=1}^n \hat{\text{Sum}}(i) + \hat{M\text{Sum}}(j)$
 $\text{temp2} = (n+1 - j)\delta t$ from (A2.12)

Fig. A2.2 Flow diagram for evaluating $\hat{\tau}_L(\hat{t}_{n+1})$
 $(k(\hat{t}_i) - \text{integrand of } F_2 \text{ at } \hat{t}_i)$

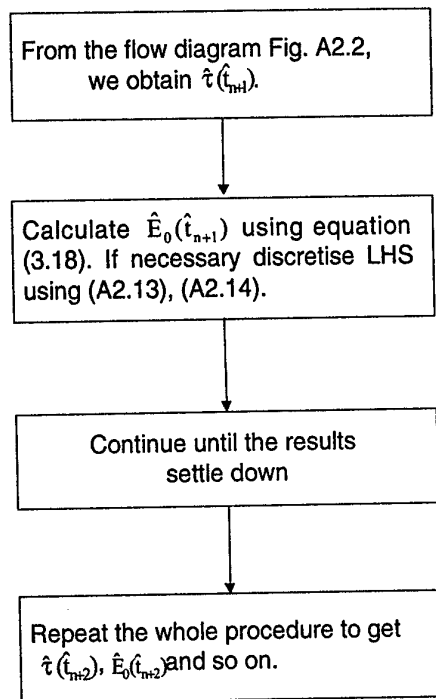


Fig.A2.3 Flow diagram for evaluating $\hat{E}_0(\hat{t}_{n+1})$

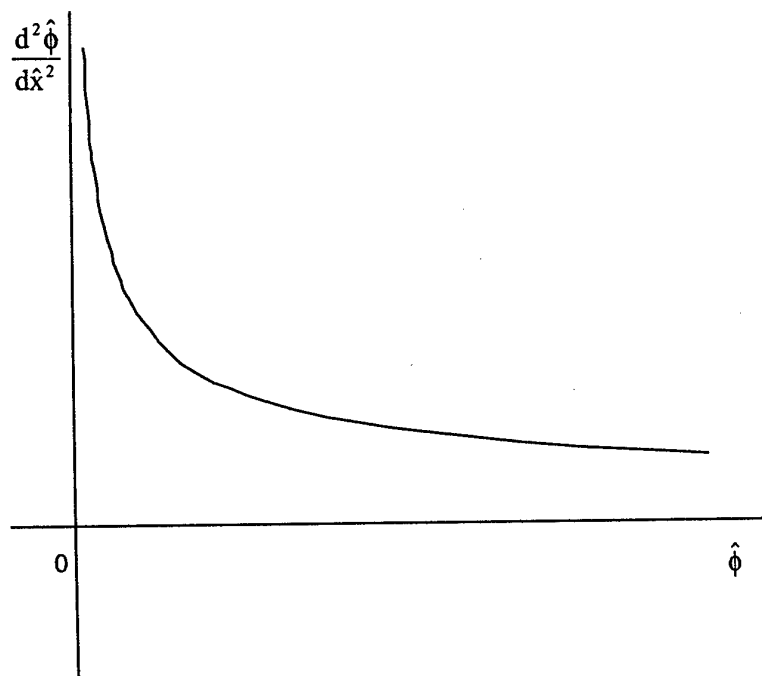


Fig. A3.1 The diagram of Eq. (A3.1a)

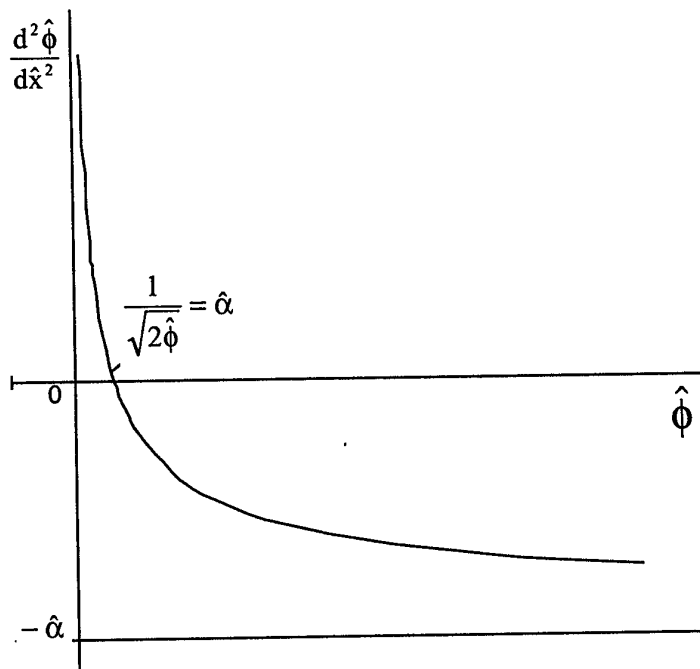


Fig. A3.2 The diagram of Eq. (A3.1b)

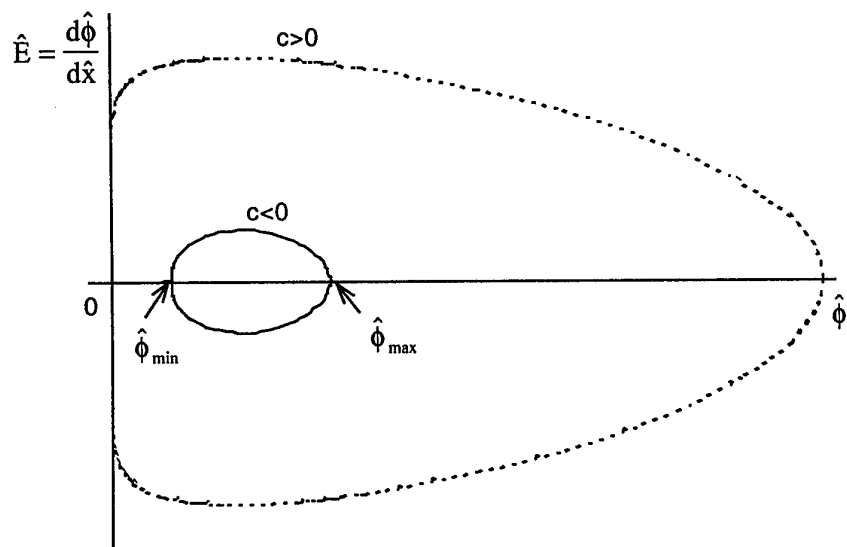


Fig. A3.3 The diagram of Eq.(A3.2b)

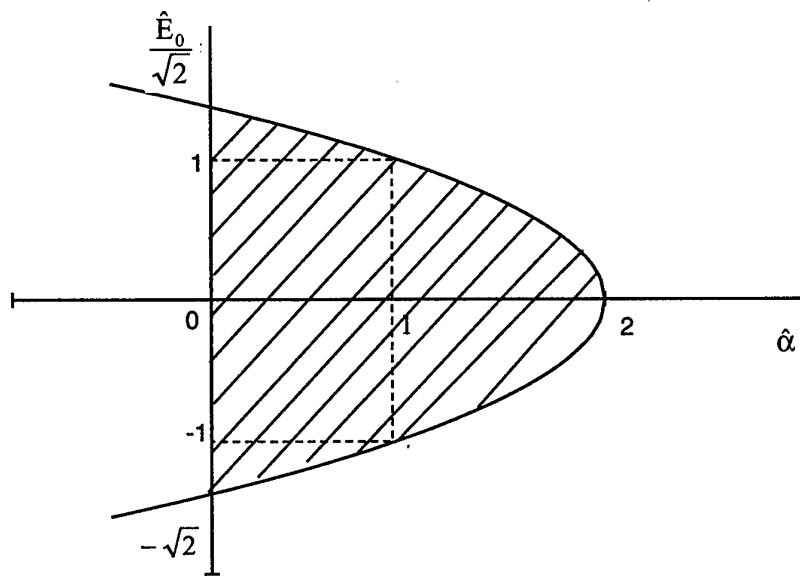


Fig. A3.4 The diagram of Eq. (A3.4)